INVESTIGATION OF NON-INTERCALATION ELECTRODE MATERIALS FOR NEXT-GENERATION BATTERIES

BY

SANGHYEON KIM

DISSERTATION

Submitted in partial fulfillment of the requirements
for the degree of Doctor of Philosophy in Materials Science and Engineering
in the Graduate College of the
University of Illinois at Urbana-Champaign, 2019

Urbana, Illinois

Doctoral Committee:

Professor Paul V. Braun, Chair
Associate Professor Shen J. Dillon
Assistant Professor Christopher Evans
Assistant Professor Joaquín Rodríguez-López

ABSTRACT

As new emerging techniques such as electric vehicles and energy storage at large scale are growing, the demands of secondary rechargeable batteries with high energy density increase dramatically. Conversion and alloying electrodes for secondary rechargeable batteries have been studied intensively as alternatives to intercalation materials as they can provide 2 to 5 times larger gravimetric capacities. However, there are many challenges facing the practical application of conversion electrodes. In this dissertation, the problems of conversion and alloying electrodes are discussed and addressed.

In Chapter 2, the electrochemical properties of FeF_2 conversion cathodes coated on a 3D Ni scaffold with a thin layer of Al_2O_3 are studied. The 3D scaffold improves the reaction kinetics and enables a high specific capacity by providing an efficient electron pathway to the insulating FeF_2 and shortening Li diffusion length. Al_2O_3 coating appears to improve the cycle life significantly as it prevents the side reaction by limiting the direct contact of the electrode with the electrolyte.

In Chapter 3 and 4, this dissertation reports new alloying cathode materials for lithium and sodium ion batteries. The fabrication of a rGO/LiI composite enables the use of LiI as a Li-ion battery cathode. The freestanding rGO/LiI electrodes show stable long-term cycling, reduced shuttling and good rate performance with high specific capacity and small hysteresis. The improved electrochemical performance can be attributed to strong interactions between the active materials and rGO, and the reduced ion and electron transport distances provided by the 3D structured cathode. This dissertation also demonstrates the fabrication of a NaI-loaded CNT mat cathode for Na-ion battery cathode application. The electrodes show a good capacity retention, high specific energy density, and small hysteresis. Adding a CNT mat interlayer between the NaI composite cathode and the separator, and FEC to the electrolyte significantly suppresses shuttling of active materials during cycling. Using ex situ XPS and Raman data, the relevant processes occurring during cycling of the CNT/NaI cathode are examined.

In Chapter 5, a volume expansion issue of conversion electrodes is addressed. A 3D Ni supported Sb_2O_3 electrode is prepared by colloidal templating and pulsed electrodeposition followed by heat treatment. Larger pore interconnects are obtained in the 3D scaffold to increase active materials loading and accommodate a large volume expansion. The electrodes accommodate volume expansion without lowering the overall energy density. The stable cycling

performance can be attributed to the 3D metal scaffold which supports active materials undergoing huge volume changes and post heat treatment effect.

Finally, the reversibility of conversion reaction is discussed in Chapter 6. The electrochemical properties of SnS, chosen as a representative metal sulfide, are studied in a both solid-state and liquid cell. The solid electrolyte prevents the degradation of the SnS active material, enables a reversible conversion reaction, and suppresses electrolyte reduction, the combination of which leads to a stable cycling performance and small first cycle irreversible capacity. Reaction chemistry of SnS in a solid-state cell is discussed more in detail by ex situ XRD and XAS results.

Acknowledgments

I'd like to thank my advisor, Prof. Paul V. Braun for giving me a great opportunity to work for his group and supervising me carefully for the past 5 years. His scientific insight and critical thinking influenced me in a positive way and I was able to become an independent researcher under his guidance. He was always open to my opinion and guided me in the right direction kindly. Again, I'd like to appreciate him for his support for me during my Ph.D. course. Also, I'd like to thank my committee members, Prof. Shen J. Dillon, Prof. Christopher Evans and Prof. Joaquín Rodríguez-López for their reviews and suggestions for my work. I'd like to appreciate their invaluable feedbacks to further improve my work.

I'd like to show my appreciation to Erica Malloch and Susie Lighty for their administrative assistance. I could solely focus on my research thanks to them. I'm grateful to many staff members of the Materials Research Laboratory and machine shop for training and assistance. My work would have not been completed successfully on time without these expert people.

I'd like to give special thanks to Kaitlin Tyler, Matthew Goodman, Junjie Wang and Jin Gu Kang for training me many equipment and techniques, and helping me settle in. I was able to get used to the new environment and start my research quickly with help of them. I was very fortunate that I met awesome labmates in the Braun group for the past 5 years. They are Arghya Patra, Ashish Kulkarni, Michael Caple, Subing Qu, Dr. Runyu Zhang, Zhao Li, Dr. Osman Cifi, Atul Agrawal, Prof. Lilong Xiong, Dr. Zhenxing Yu, Dr. Bhaskar Akkisetty, Christian Ocier, and Yeong-Hui Seo. I will remember every happy moment we shared together and it will be unforgettable. I was not lonely in the US thanks to them. I'd like to thank Julia Kohanek, Shiyan Zhang and Shuqi Lai for consulting and supporting each other. We joined the Braun group at the same time and spent 5 years together. I'd like to wish the best of luck to them in their future career.

It was a great experience for me to get to know and work with highly talented people. They are Prof. Sung-Kon Kim, Prof. Jinyun Liu, Dr. Xiangming Li, Prof. Andrew A. Gewirth, Prof. Ralph G. Nuzzo, Prof. Nuri Oh, Dr. Ke Sun. Qun Li, Minjeong Shin, Dr. Pengcheng Sun Hoonkee Park, Prof. Ho Won Jang, and Prof. David G. Cahill. Particularly, I'd like to give special thanks to Jungwoo Shin, Dr. Jaewon Choi, Dr Seong-Min Bak, and Prof. Lingzi Sang. I'd

like to appreciate them for their contributions to my work, helpful discussion, and scientific inspiration. I'll be looking forward to working with these people in the near future again.

I must thank my parents and all my family members for their support and love. They respected my decision to study abroad and kept me motivated to pursue higher goals. I could overcome all difficulties and finish my Ph.D. program thanks to their encouragement. I hope I can repay their kindness in the future.

Finally, I'd like to thank Kwanjeong Educational Foundation for a scholarship.

TABLE OF CONTENTS

LIST OF ABBREVIATIONS

1D	One-dimensional
3D	Three-dimensional
ALD	Atomic layer deposition
BET	Brunauer, Emmett and Teller
CNF	Carbon nanofiber
CNT	Carbon nanotube
CV	Cyclic voltammetry
DMC	Dimethyl carbonate
EC	Ethylene carbonate
EDS	Energy dispersive spectroscopy
EIS	Electrochemical impedance spectroscopy
EXAFS	Extended x-ray absorption fine structure
FEC	Fluoroethylene carbonate
FT	Fourier transforms
GITT	Galvanostatic intermittent titration technique
HRTEM	High resolution transmission electron microscopy
LIBs	Lithium ion batteries
NMP	N-methyl-2-pyrrolidone
SIBs	Sodium ion batteries
PC	Propylene carbonate
PEEK	Polyether ether ketone
PS	Polystyrene
PVDF	Polyvinylidene fluoride
rGO	Reduced graphene oxide
SAED	Selected area electron diffraction
SEI	Solid electrolyte interface
SEM	Scanning electron microscopy
STEM	Scanning transmission electron microscopy
TEM	Transmission electron microscopy
TGA	Thermogravimetric analysis

XANES	X-ray absorption near edge structure
XAS	X-ray absorption spectroscopy
XPS	X-ray photoelectron spectroscopy
XRD	X-ray diffraction
wt	Weight
ZB	Zinc blende

CHAPTER 1
INTRODUCTION

1.1 Lithium ion and next generation secondary batteries

Since Sony first commercialized LIBs in 1991, it has become a popular power source for electronic devices such as cell phones, laptops etc,[1-3] because of its high energy density which is at least 2-3 times greater than most other rechargeable battery chemistries.[4] LIBs are also key elements for vehicle electrification, a trend that appears to be accelerating recently.[4]

The rechargeable LIBs do not store energy in the form of metallic lithium. The most general types of commercial LIBs consist of a graphite-based negative electrode (anode), organic liquid electrolyte, and a $LiCoO_2$ positive electrode (Figure 1.1). During charging, lithium ions are deintercalated from the layered crystal structure $LiCoO_2$ intercalation host, pass across the electrolyte, and are intercalated between the graphite layers in the anode in zero-valence form. The reverse reaction occurs in the discharge process.

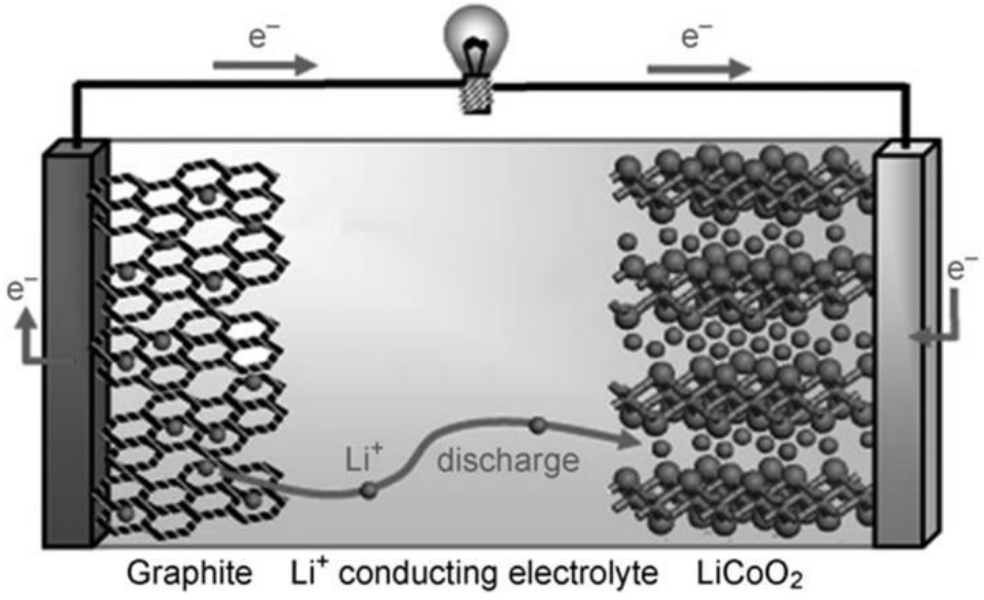

Figure 1.1 Schematic description of a conventional lithium ion battery.[4]

Although the graphite-$LiCoO_2$ cell has been the dominate lithium ion battery system so far, the development of new battery electrodes is urgent as the need for high energy and power

density systems is increasing.[5] Since many key battery features such as energy density, cycle life, and rate performance are mostly determined by intrinsic electrochemical properties of electrode materials, extensive research has been conducted on the development of new electrode materials for LIBs.

Even though LIBs have become the dominant energy storage system for portable devices, people have tried to find better energy storage systems to overcome drawbacks of LIBs. For example, there has been a concern that the cost-effective supply of Li is not sufficient to meet the increasing demands for LIBs. There are concerns that the large-scale application of LIBs will be held back because of the limited abundance and cost of lithium.[6,7]

SIBs have become considered as an alternative to LIBs recently because of the abundance and low costs of sodium (Na).[8] SIBs' working principle is quite similar to LIBs. Na ions shuttle back and forth between the two electrodes during charge and discharge, same as LIBs.

Sodium is positioned below Li in the periodic table, and thus they have similar chemical properties. Table 1.1 shows the comparison of some parameters of Na and Li.[8] Due to the larger ionic size of Na versus lithium and its lower standard electrochemical potential (2.70 V vs. SHE, Standard Hydrogen Electrode) compared to those of Li (3.04 V vs. SHE), the power and energy density of SIBs are inevitably lower than that of LIBs. However, these disadvantages can be compensated by a much lower cost of Na for some particular applications. For example, SIBs may be more cost-effective than LIBs for the grid-scale storage where the operating costs are an important aspect of an entire system.[9]

Characteristics	Na	Li
Cation radius	97 pm	68 pm
Atomic weight	23 g mol^{-1}	6.9 g mol^{-1}
E_o *vs.* SHE	2.7 V	3.04 V
Melting point	97.7 °C	180.5 °C
Abundance	23.6×10^3 mg kg^{-1}	20 mg kg^{-1}
Distribution	Everywhere	70% in South America
Price, carbonates	120 $/ton	4000 $/ton
Theoretical capacity, metal	1165 mAh g^{-1}	3829 mAh g^{-1}

Table 1.1 Comparison of Na and Li.[8]

Another class of new battery systems that have been explored as an alternative to LIBs are all solid-state batteries. In an all solid-state battery the organic liquid electrolytes common in LIBs are replaced by solid electrolytes. One motivation is to eliminate the use of flammable organic electrolytes as they generate a risk of explosion and fire. Even though the theoretical capacity of a metallic Li anode is as high as 3861 mA h g^{-1}, its use with liquid electrolytes can lead to Li dendrite formation, which is a common cause of an explosion.[10,11] Solid electrolytes may enable use of a Li anode because it can physically prevent lithium dendrite growth.[12] Also, solid electrolytes can eliminate an inherent safety problem of liquid electrolyte as they are non-flammable.[11]

Not only from a safety point of view but also from an energy density aspect, all solid-state batteries are more fascinating system than conventional liquid electrolyte-based batteries. The density of solid electrolyte is higher than that of liquid electrolyte, leading to improved total energy density. The total energy density of batteries can be further improved by reducing the net weight and volume of the battery as solid electrolyte enables fewer requirements on the packaging.[11] Many different types of solid electrolyte have been reported so far; perovskite-type (Li(La)TiO_3), NASICON-type (LATP, LAGP, etc.), garnet-type ($Li_7La_3Zr_2O_{12}$), lithium-phosphorous-oxynitride (LiPON), sulfide glass type and etc.[11,14,15] The solid electrolytes for LIBs are summarized in Table 1.2 Solid electrolytes should satisfy several requirements. They should have high Li ionic conductivity and low electronic conductivity. Also, they should be electrochemically stable in the wide range of potential and chemically compatible with the electrodes, especially metallic Li anodes.[11,14]

Type	Materials	Conductivity ($S\,cm^{-1}$)	Advantages	Disadvantages
Oxide	Perovskite $Li_{3.3}La_{0.56}TiO_3$, NASICON $LiTi_2(PO_4)_3$, LISICON $Li_{14}Zn(GeO_4)_4$ and garnet $Li_7La_3Zr_2O_{12}$	10^{-5}–10^{-3}	• High chemical and electrochemical stability • High mechanical strength • High electrochemical oxidation voltage	• Non-flexible • Expensive large-scale production
Sulfide	Li_2S–P_2S_5, Li_2S–P_2S_5–MS_x	10^{-7}–10^{-3}	• High conductivity • Good mechanical strength and mechanical flexibility • Low grain-boundary resistance	• Low oxidation stability • Sensitive to moisture • Poor compatibility with cathode materials
Hydride	$LiBH_4$, $LiBH_4$–LiX (X = Cl, Br or I), $LiBH_4$–$LiNH_2$, $LiNH_2$, Li_3AlH_6 and Li_2NH	10^{-7}–10^{-4}	• Low grain-boundary resistance • Stable with lithium metal • Good mechanical strength and mechanical flexibility	• Sensitive to moisture • Poor compatibility with cathode materials
Halide	LiI, spinel Li_2ZnI_4 and anti-perovskite Li_3OCl	10^{-8}–10^{-5}	• Stable with lithium metal • Good mechanical strength and mechanical flexibility	• Sensitive to moisture • Low oxidation voltage • Low conductivity
Borate or phosphate	$Li_2B_4O_7$, Li_3PO_4 and Li_2O–B_2O_3–P_2O_5	10^{-7}–10^{-6}	• Facile manufacturing process • Good manufacturing reproducibility • Good durability	• Relatively low conductivity
Thin film	LiPON	10^{-6}	• Stable with lithium metal • Stable with cathode materials	• Expensive large-scale production
Polymer	PEO	10^{-4} (65–78 °C)	• Stable with lithium metal • Flexible • Easy to produce a large-area membrane • Low shear modulus	• Limited thermal stability • Low oxidation voltage (<4 V)

Table 1.2 Summary of solid electrolytes for LIBs.[13]

1.2 Conversion and alloying electrodes for high energy density electrodes

As mentioned above, despite that graphite and $LiCoO_2$ have been successful for the commercialization of LIBs, these intercalation materials have intrinsic limitations when it comes to capacity. In intercalation materials, crystal structure of host material is maintained and the capacity of intercalation materials is limited by the number of empty space within the crystal structure where Li ion can be accommodated. To achieve higher energy density of battery beyond the intercalation materials, the development of novel concepts in materials research is necessary. This has led to interest into conversion compound based electrodes.

Conversion and alloying electrodes provide high specific capacity compared to intercalation materials because all possible redox states of active ion can be utilized.[16] Conversion and alloying electrodes undergo crystal structure changes, accompanied by the breaking and reforming chemical bonds.[17]

$$\text{Conversion : } M_aX_b + (b \bullet n)\ Li \leftrightarrow aM + bLi_nX$$

$$\text{Alloying : } Z + aLi \leftrightarrow Li_aZ$$

Conversion electrodes consist of transition metal ions, M, such as Fe^{3+}, Fe^{2+}, Ni^{2+}, Cu^{2+}, Co^{2+}, and X ions which are typically O, S, N, P and F. Transition metal nanoparticles dispersed in the Li_nX matrix is formed when lithium ions react with the conversion compounds.[16,18] Table 1.3 shows the potential value for the plateaus of binary transition metal compounds, M_aX_b . Most of them exhibit low potential value except some fluorides, indicating that majority of them are anode candidates and only a few metal fluorides can be considered as cathodes.

	X=O		X=S		X=N		X=P		X=F	
	Phase	E [V]	Phase	E [V]	Phae	E [V]	Phase	E [V]	Phase	E [V]
M=Ti									TiF_3	0.85
M=V									VF_3	0.4
M=Cr	Cr_2O_3	0.2	CrS	0.85	CrN	0.2			CrF_3	1.8
M=Mn	MnO_2	0.4	MnS	0.7			MnP_4	0.2		
	Mn_2O_3	0.3								
	MnO	0.2								
M=Fe	Fe_2O_3	0.8	FeS_2	1.5			FeP_2	0.3	FeF_3	2
	Fe_3O_4	0.8	FeS	1.3	Fe_3N	0.7	FeP	0.1		
	FeO	0.75								
M=Co	Co_3O_4	1.1	CoS_2	1.65-1.3	CoN	0.8	Co_3P	0.3	CoF_3	2.2
	CoO	0.8	$Co_{0.92}S$	1.4	Co_3N	1				
			Co_9S_8	1.1						
M=Ni	NiO	0.6	NiS_2	1.6			NiP_3	0.7	NiF_2	1.9
			NiS	1.5	Ni_3N	0.6	NiP_2	0.5-0.3		
			Ni_3S_2	1.4			Ni_3P	Slope		
M=Cu	CuO	1.4	CuS	2.0-1.7			CuP_2	0.7	CuF_2	3
	Cu_2O		Cu_2S	1.7			Cu_3P	0.8		
M=Mo	MoO_3	0.45	MoS_2	0.6						
	MoO_2	Slope								
M=W			WS_2	0.8-0.6						
M=Ru	RuO_2	0.9								

Table 1.3 Experimental values of potential for the plateaus associated with conversion reactions in binary transition metal compounds, M_aX_b . "Slope" indicates the absence of distinct voltage plateau in the electrochemical profile.[16]

Alloying electrodes undergo chemical transformation reaction or alloying reaction. They are also called alloying electrodes. The crystal structure changes from one single phase to another single phase through intermediate steps during the charge and discharge. It is reported that Si, Sn, Sb, Al, Bi, P, In, S, Se, Te and I belong to alloying electrodes. Table 1.4 shows the average plateaus potential, lithiated phase and theoretical specific capacity of various alloying materials. Most of them show low potential except selenium and sulfur, indicating that majority of them are anode candidates and only selenium and sulfur can be considered as cathodes.

	Si	Sn	Sb	Al	Bi	Se	S
Potential vs. Li (V)	0.4	0.6	0.9	0.3	0.8	2	2.2
Lithiated phase	$Li_{4.4}Si$	$Li_{4.4}Sn$	Li_3Sb	LiAl	Li_3Bi	Li_2Se	Li_2S
Theoretical specific capacity ($mAh\ g^{-1}$)	4200	994	660	993	385	675	1675

Table 1.4 Comparison of average plateaus potential, lithiated phase and theoretical specific capacity of various alloying materials.[19]

Figure 1.2 shows how different conversion and alloying electrodes are. The crystal structure of the host phase is destroyed in common. However, conversion electrodes produce two new phases after conversion reaction while alloying electrodes form a single new phase through alloying reaction.

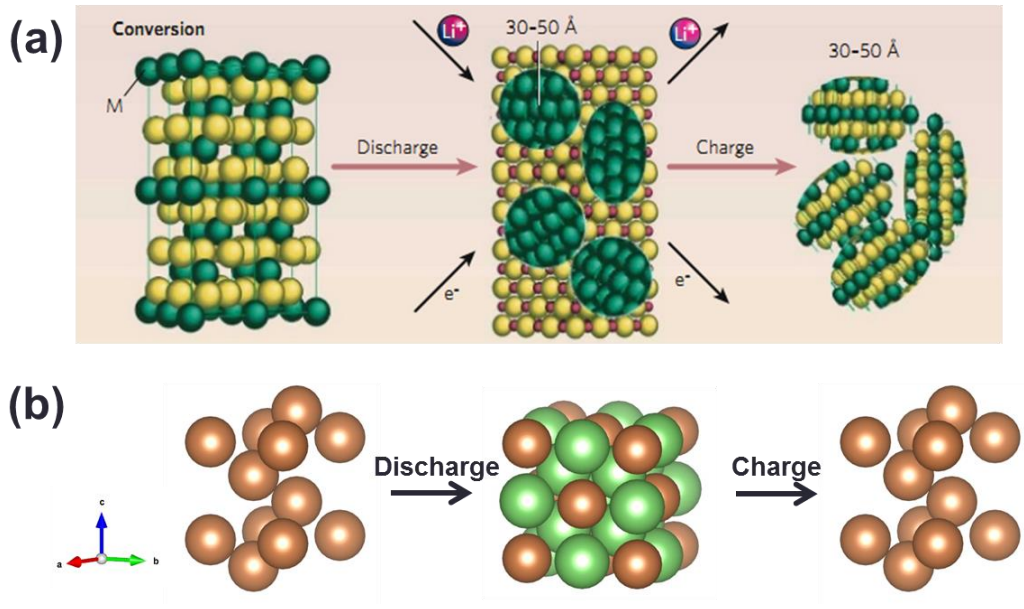

Figure 1.2 Conversion and alloying reactions: (a) conversion with the formation of two new phases; (b) chemical transformation (alloying) with a single new phase formation.[1]

Analogously, most of the conversion electrodes for LIBs can be operational in SIBs. Fe_2O_3, Co_3O_4, and CuO have been reported as conversion electrodes for SIBs so far.[20-23] Sn, Sb, P, S, and Se have been reported to have alloying reaction with Na.[24-28] The working potential of these electrodes is lower in SIBs than in LIBs. This is because sodium reduction potential is originally higher than that of lithium.

1.3 Drawbacks of conversion and alloying electrodes

Although conversion and alloying electrodes can provide much higher energy density than intercalation materials, they have several drawbacks which must be overcome for practical applications. In this chapter, some disadvantages of conversion and alloying electrodes and previous approaches to address these issues will be introduced.

1.3.1 Low electrical conductivity

Most of the conversion electrodes show poor electrical conductivity except some alloying electrodes which are metal and semimetal such as Sn, Sb, and Bi. Electrical

conductivity values of representative conversion electrodes are shown in Table 1.5 Especially, sulfur and metal fluorides, cathode candidates, are known as insulator due to its very low electrical conductivity.

		Electrical conductivity
Fe_2O_3	Conversion	1×10^{-7}, poor
NiO	Conversion	$\sim 1 \times 10^{-5}$, poor
S	Alloying	5×10^{-28}, insulator
Fluoride	Conversion	Insulator
I_2	Alloying	1×10^{-7}, poor

Tabe 1.5 Electrical conductivity of representative conversion and alloying electrodes.[29-32]

A low electrical conductivity of the electrode can lead to poor rate performance, low active material utilization, and large voltage hysteresis. Thus, the electrical conductivity of an electrode needs to be improved either intrinsically or extrinsically. The use of conductive additives such as CNT and rGO have been attempted to improve the electrical conductivity of electrodes.[33-35] These approaches were effective, but use of carbon-based conductive additives can decrease the total energy density of electrodes.

1.3.2 Voltage hysteresis and sluggish reaction kinetics

A voltage hysteresis is a voltage difference between discharge and charge processes. In other words, the voltage hysteresis is a ratio of the energy put in to the energy produced. The voltage hysteresis needs to be reasonably small to avoid poor roundtrip energy inefficiency. The voltage hysteresis of conversion electrodes is generally larger than that of intercalation materials and practical application of conversion electrodes is mainly limited by this large hysteresis. Both kinetic and thermodynamic factors are known to contribute to voltage hysteresis.

Poor electrical conductivity or sluggish lithium diffusion can cause large hysteresis kinetically.[36] However, the previous study suggested that the hysteresis of conversion electrodes mainly stems from thermodynamic factors rather than kinetic factors.[37] Conversion

reaction accompanies chemical bond breaking and reorganization of crystal structure. This process requires the formation of an activation energy leading to large hysteresis. Also, the hysteresis of conversion reaction might originate from inherently different paths of reaction.[37] In this case, the hysteresis is determined by the difference between each thermodynamic potential of discharge and charge process.

In general, conversion electrodes (several hundred mV to ~2 V) show larger voltage hysteresis than alloying electrodes (0.1~0.5 V). Figure 1.3 shows the typical hysteresis of fluoride, oxide, sulfide and phosphide conversion electrodes. It is reported that fluorides exhibit the highest hysteresis while phosphides exhibit lowest hysteresis, indicating the dependence of hysteresis on anion species.[16]

To reduce the hysteresis, people have tried to enhance reaction kinetics by using conductive medium or nanoengineering.[38,39] But, significantly reductions in hysteresis has not been reported yet.

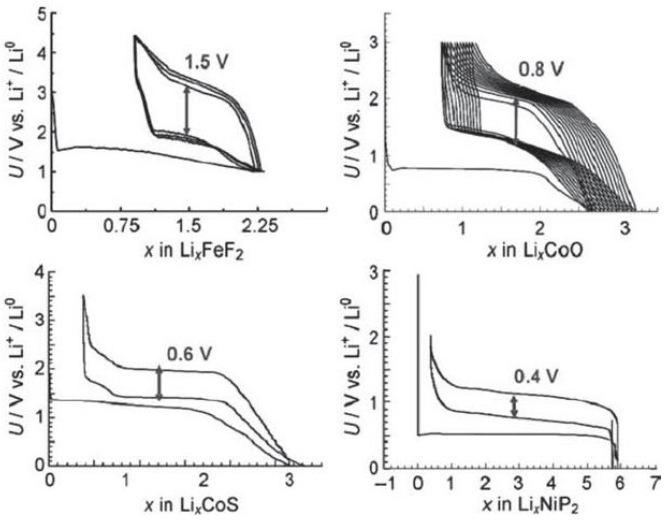

Figure 1.3 Voltage composition profiles for a representative binary fluoride, oxide, sulfide, and phosphide. The values of ΔE_{hys} at the second cycle are indicated.[16]

1.3.3 Undesirable interactions with electrolyte

It is reported that conversion electrodes suffer from undesirable interaction with electrolytes during cycling. For example, metal fluoride is notorious for its metal dissolution

during cycling. CuF_2 is a promising conversion cathode candidate because of its high reaction potential (3 V vs Li^+/Li). However, the conversion reaction is not reversible after first cycle due to the dissolution of Cu produced by reduction of CuF_2.[40] Previous studies reported that the rapid capacity decay of FeF_2 and CoF_2 are due to metal dissolution in conventional carbonate-based electrolyte and, formation and continued growth of a solid electrolyte interphase layer at the interface between electrode and electrolyte.[41-43]

Some alloying electrodes also suffer from unwanted interaction with electrolyte. For example, shuttling is a serious issue in lithium-sulfur batteries. This happens when final or intermediate products are highly soluble in conventional organic electrolytes. Figure 1.4 shows a schematic illustration of shuttling: Li/LiI cell as an example. I_2 and LiI_3 are soluble in aprotic electrolyte and they can freely migrate to the anode side and react with metal Li. This leads to serious self-discharge making charging time of the battery infinite and coulombic efficiency very low.

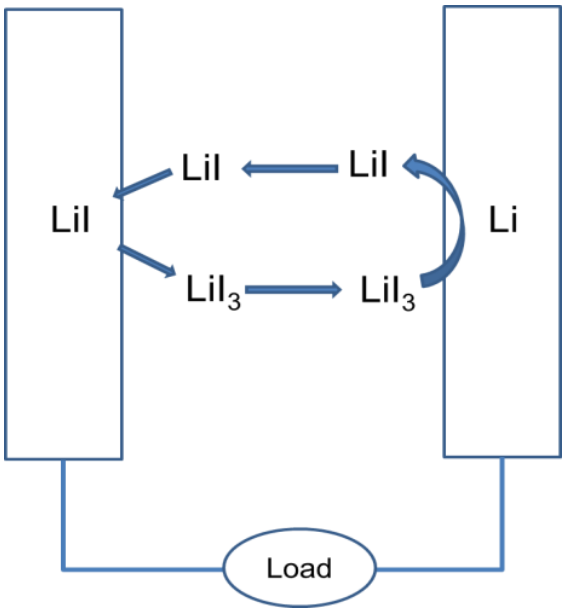

Figure 1.4 Schematic illustration of shuttle effect in a liquid electrolyte Li/LiI cell.

To avoid undesirable side reactions between an electrode and electrolyte, many different types of electrolyte and electrolyte additive have been used to form a protective layer. It is reported that side reactions or metal dissolution can be suppressed by the formation of stable SEI

on the surface of the electrode through electrolyte decomposition.[41,42,44] Use of interlayer can limit shuttling by physically blocking the migration of dissolved species.[45,46] Some electrolyte additives are known to be effective to reduce the shuttling by forming a stable SEI as mentioned above.[47,48] A composite electrode containing functionalized carbon materials with high adsorptivity can improve the adhesion between carbon and active materials and reduce the dissolution of active materials.[48-50]

1.3.4 Huge volume change

Conversion and alloying electrodes undergo huge volume expansion during cycling as they uptake multiple ions as shown in Figure 1.5 Theoretical volume expansion ratio of representative conversion and alloying electrodes for LIBs is presented in Table 1.6 Repeated volume expansion and contraction can cause materials pulverization and loss of electrical contact between active materials and current collectors, leading to large overpotential and capacity decay.[51] Furthermore, undesirable reaction or new SEI formation can occur constantly at the interface between electrolyte and newly exposed electrode surface created by continuous volume changes.[17] To address volume expansion issue, nanostructures such as 1D nanowire, nanotube, 3D inverse opal, and core-shell structures have been attempted to provide an enough empty space within the electrode.[52-58] Composites electrode prepared by incorporating active materials into carbon-based materials such as rGO or carbon nanofiber can buffer the volume expansion and prevent the mechanical loss of active materials.[59-62] Even though previous studies showed high gravimetric capacities, volumetric capacities were mostly overlooked. Active material loading and amount of carbon-based additives need to be optimized to achieve not only high gravimetric capacity but also high volumetric capacity.

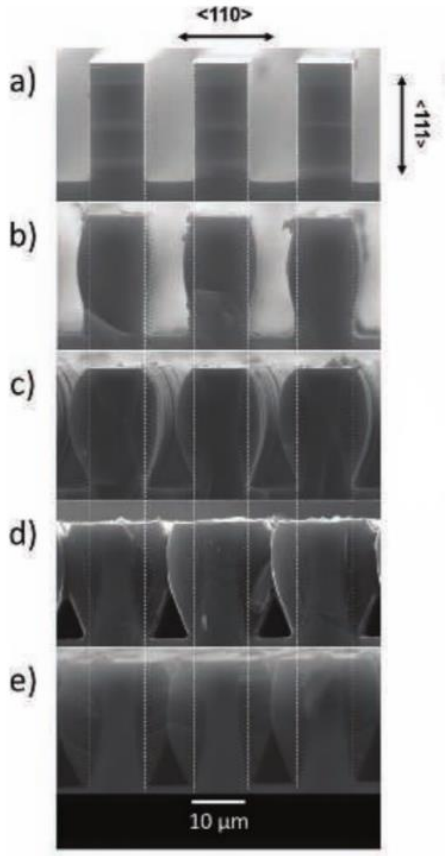

Figure 1.5 Single-crystalline (111) silicon wafer with an array of 10 µm wide bars spaced 10 µm apart galvanostatically charged at current densities of b) 36.8 µA cm^{-2} c) 73.9 µA cm^{-2} d) 147 µA cm^{-2} e) 289 µA cm^{-2} for up to 10 hours.[63]

	Volume Expansion Ratio	Electrochemical reaction
Fe_2O_3	192	$Fe_2O_3+6Li \rightarrow 2Fe+3Li_2O$
NiO	193	$NiO+2Li \rightarrow Ni+Li_2O$
FeF_2	150	$FeF_2+2Li \rightarrow Fe+2LiF$
Sb	300	$Sb+3Li \rightarrow Li_3Sb$
Sn	360	$5Sn+22Li \rightarrow Li_{22}Sn_5$
Si	420	$4Si+15Li \rightarrow Li_{15}Si_4$

Table 1.6 Theoretical volume expansion ratio of various conversion electrodes for LIBs and corresponding electrochemical reaction.

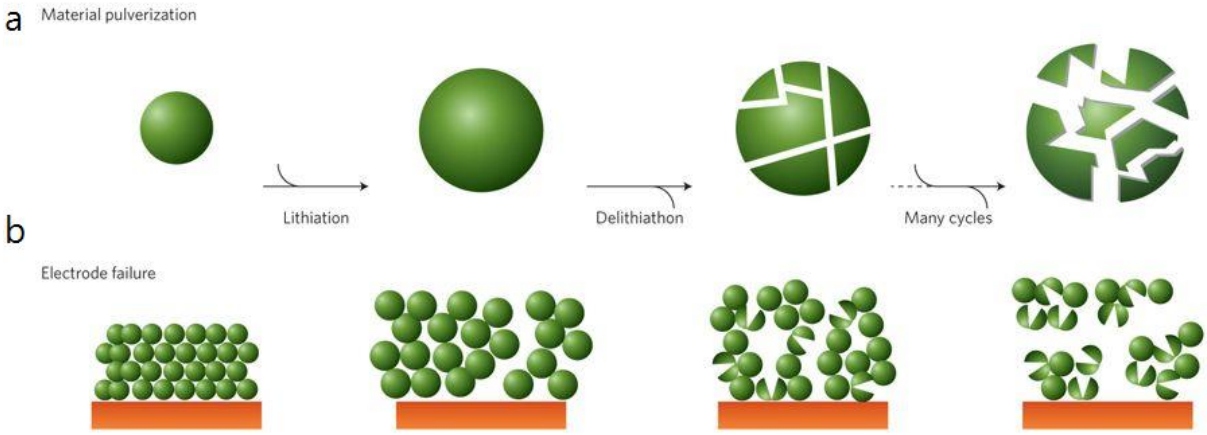

Figure 1.6 Mechanical degradation of high-capacity material at particle level (a) and electrode level (b) during cycling.[47]

In this dissertation, the aforementioned issues of conversion and alloying electrodes are discussed and addressed. FeF_2, one of the conversion cathode candidates, are studied in Chapter 2. 3D metal scaffold and ALD coating are used to improve reaction kinetics and prevent side reaction between electrode and electrolyte. In spite of improved cycling stability and good rate performance, large hysteresis and relatively low working potential are not promising. This leads to interest into new conversion system with high working potential and small hysteresis. New cathode materials for lithium and sodium ion batteries are discussed in Chapter 3 and 4. Most efforts are made to reduce shuttling. 3D metal scaffolds used in Chapter 2 can be also useful for a high capacity electrode for SIBs. Chapter 5 shows the use of a 3D metal scaffold for sodium ion battery application. Many problems of conversion electrode arising from liquid electrolytes such as metal dissolution or shuttling can be fundamentally solved by using solid electrolyte. Chapter 6 discusses the reversible conversion reaction enabled by using solid electrolyte.

1.4 References

[1] M. Armand, J.-M. Tarascon, *nature* **2008**, *451*, 652.

[2] J. B. Goodenough, *Acc. Chem. Res.* **2012**, *46*, 1053.

[3] J.-M. Tarascon, M. Armand, *Nature* **2001**, *414*, 359.

[4] P. G. Bruce, B. Scrosati, J. M. Tarascon, *Angew. Chem., Int. Ed.* **2008**, *47*, 2930.

[5] V. Etacheri, R. Marom, R. Elazari, G. Salitra, D. Aurbach, *Energy Environ. Sci.* **2011**, *4*, 3243.

[6] H. Kim, H. Kim, Z. Ding, M. H. Lee, K. Lim, G. Yoon, K. Kang, *Adv. Energy Mater.* **2016**, *6*, 1600943.

[7] S. W. Kim, D. H. Seo, X. Ma, G. Ceder, K. Kang, *Adv. Energy Mater.* **2012**, *2*, 710.

[8] H. Hou, M. Jing, Y. Yang, Y. Zhang, W. Song, X. Yang, J. Chen, Q. Chen, X. Ji, *J. Power Sources* **2015**, *284*, 227.

[9] J. Whitacre, T. Wiley, S. Shanbhag, Y. Wenzhuo, A. Mohamed, S. Chun, E. Weber, D. Blackwood, E. Lynch-Bell, J. Gulakowski, *J. Power Sources* **2012**, *213*, 255.

[10] J. Bates, N. Dudney, B. Neudecker, A. Ueda, C. Evans, *Solid State Ionics* **2000**, *135*, 33.

[11] C. Sun, J. Liu, Y. Gong, D. P. Wilkinson, J. Zhang, *Nano Energy* **2017**, *33*, 363.

[12] F. Mizuno, A. Hayashi, K. Tadanaga, M. Tatsumisago, *Adv. Mater.* **2005**, *17*, 918.

[13] A. Manthiram, X. Yu, S. Wang, *Nat. Rev. Mater.* **2017**, *2*, 16103.

[14] J. G. Kim, B. Son, S. Mukherjee, N. Schuppert, A. Bates, O. Kwon, M. J. Choi, H. Y. Chung, S. Park, *J. Power Sources* **2015**, *282*, 299.

[15] E. Quartarone, P. Mustarelli, *Chem. Soc. Rev.* **2011**, *40*, 2525.

[16] J. Cabana, L. Monconduit, D. Larcher, M. R. Palacin, *Adv. Mater.* **2010**, *22*, E170.

[17] F. Wu, G. Yushin, *Energy Environ. Sci.* **2017**, *10*, 435.

[18] F. Wang, R. Robert, N. A. Chernova, N. Pereira, F. Omenya, F. Badway, X. Hua, M. Ruotolo, R. Zhang, L. Wu, *J. Am. Chem. Soc.* **2011**, *133*, 18828.

[19] W.-J. Zhang, *J. Power Sources* **2011**, *196*, 13.

[20] X. Liu, T. Chen, H. Chu, L. Niu, Z. Sun, L. Pan, C. Q. Sun, *Electrochim. Acta* **2015**, *166*, 12.

[21] Y. Liu, Z. Cheng, H. Sun, H. Arandiyan, J. Li, M. Ahmad, *J. Power Sources* **2015**, *273*, 878.

[22] J.-W. Wen, D.-W. Zhang, Y. Zang, X. Sun, B. Cheng, C.-X. Ding, Y. Yu, C.-H. Chen, *Electrochim. Acta* **2014**, *132*, 193.

[23] S. Yuan, X. l. Huang, D. l. Ma, H. G. Wang, F. Z. Meng, X. B. Zhang, *Adv. Mater.* **2014**, *26*, 2273.

[24] Y. Xu, Y. Zhu, Y. Liu, C. Wang, *Adv. Energy Mater.* **2013**, *3*, 128.

[25] A. Darwiche, C. Marino, M. T. Sougrati, B. Fraisse, L. Stievano, L. Monconduit, *J. Am. Chem. Soc.* **2012**, *134*, 20805.

[26] J. Qian, X. Wu, Y. Cao, X. Ai, H. Yang, *Angew. Chem.* **2013**, *125*, 4731.

[27] J. Wang, J. Yang, Y. Nuli, R. Holze, *Electrochem. Commun.* 2007, 9, 31.

[28] L. Zeng, W. Zeng, Y. Jiang, X. Wei, W. Li, C. Yang, Y. Zhu, Y. Yu, *Adv. Energy Mater.* **2015**, *5*, 1401377.

[29] S. Ito, Y. Yui, J. Mizuguchi, *Mater. Trans.* **2010**, *51*, 1163.

[30] Z. Li, L. Yuan, Z. Yi, Y. Liu, Y. Huang, *Nano Energy* **2014**, *9*, 229.

[31] I. Popescu, Z. Skoufa, E. Heracleous, A. Lemonidou, I.-C. Marcu, *Phys. Chem. Chem. Phys.* **2015**, *17*, 8138.

[32] S. Banerjee, A. Santhanam, A. Dhathathreyan, P. M. Rao, *Langmuir* **2003**, *19*, 5522.

[33] M. Chen, J. Liu, D. Chao, J. Wang, J. Yin, J. Lin, H. J. Fan, Z. X. Shen, *Nano Energy* **2014**, *9*, 364.

[34] Z. Wang, D. Luan, S. Madhavi, Y. Hu, X. W. D. Lou, *Energy Environ. Sci.* **2012**, *5*, 5252.

[35] X. Zhu, Y. Zhu, S. Murali, M. D. Stoller, R. S. Ruoff, *ACS Nano* **2011**, *5*, 3333.

[36] M. Winter, R. J. Brodd, *Chem. Rev.* **2004,** *104*, 4245.

[37] P. Liu, J. J. Vajo, J. S. Wang, W. Li, J. Liu, *J. Phys. Chem. C.* **2012**, *116*, 6467.

[38] J. Wang, H. Zhou, J. Nanda, P. V. Braun, *Chem. Mater.* **2015**, *27*, 2803.

[39] M. A. Reddy, B. Breitung, V. S. K. Chakravadhanula, C. Wall, M. Engel, C. Kübel, A. K. Powell, H. Hahn, M. Fichtner, *Adv. Energy Mater.* **2013**, *3*, 308.

[40] X. Hua, R. Robert, L.-S. Du, K. M. Wiaderek, M. Leskes, K. W. Chapman, P. J. Chupas, C. P. Grey, *J. Phys. Chem. C.* **2014**, *118*, 15169.

[41] X. Wang, W. Gu, J. T. Lee, N. Nitta, J. Benson, A. Magasinski, M. W. Schauer, G. Yushin, *Small* **2015**, *11*, 5164.

[42] W. Gu, A. Magasinski, B. Zdyrko, G. Yushin, *Adv. Energy Mater.* **2015**, *5*, 1401148.

[43] M. Sina, R. Thorpe, S. Rangan, N. Pereira, R. A. Bartynski, G. G. Amatucci, F. Cosandey, *J. Phys. Chem. C.* **2015**, *119*, 9762.

[44] F. Wu, J. T. Lee, N. Nitta, H. Kim, O. Borodin, G. Yushin, *Adv. Mater.* **2015**, *27*, 101.

[45] Y.-S. Su, A. Manthiram, *Chem. Commun.* **2012**, *48*, 8817.

[46] H. M. Kim, J.-Y. Hwang, A. Manthiram, Y.-K. Sun, *ACS Appl. Mater. Interfaces* **2016**, *8*, 983.

[47] W. Yang, W. Yang, A. Song, L. Gao, G. Sun, G. Shao, *J. Power Sources* **2017**, *348*, 175.

[48] Q. Zhao, Y. Lu, Z. Zhu, Z. Tao, J. Chen, *Nano Lett.* **2015**, *15*, 5982.

[49] F. Wu, J. T. Lee, E. Zhao, B. Zhang, G. Yushin, *ACS Nano* **2015**, *10*, 1333.

[50] C. Wang, X. Wang, Y. Yang, A. Kushima, J. Chen, Y. Huang, J. Li, *Nano Lett.* **2015**, *15*, 1796.

[51] Y. Sun, N. Liu, Y. Cui, *Nature Energy* **2016**, *1*, 16071.

[52] J. Liu, L. Yu, C. Wu, Y. Wen, K. Yin, F.-K. Chiang, R. Hu, J. Liu, L. Sun, L. Gu, *Nano Lett.* **2017**, *17*, 2034.

[53] J. Liu, N. Li, M. D. Goodman, H. G. Zhang, E. S. Epstein, B. Huang, Z. Pan, J. Kim, J. H. Choi, X. Huang, *ACS Nano* **2015**, *9*, 1985

[54] M. S. Park, G. X. Wang, Y. M. Kang, D. Wexler, S. X. Dou, H. K. Liu, *Angew. Chem., Int. Ed.* **2007**, *46*, 750.

[55] T. Song, J. Xia, J.-H. Lee, D. H. Lee, M.-S. Kwon, J.-M. Choi, J. Wu, S. K. Doo, H. Chang, W. I. Park, *Nano Lett.* **2010**, *10*, 1710.

[56] L.-F. Cui, Y. Yang, C.-M. Hsu, Y. Cui, *Nano Lett.* **2009**, *9*, 3370.

[57] Y. Zhu, X. Han, Y. Xu, Y. Liu, S. Zheng, K. Xu, L. Hu, C. Wang, *ACS Nano* **2013**, *7*, 6378.

[58] H. Zhang, P. V. Braun, *Nano Lett.* **2012**, *12*, 2778.

[59] J. Liu, X. Chen, J. Kim, Q. Zheng, H. Ning, P. Sun, X. Huang, J. Liu, J. Niu, P. V. Braun, *Nano Lett.* **2016,** *16*, 4501.

[60] G. Derrien, J. Hassoun, S. Panero, B. Scrosati, *Adv. Mater.* **2007**, *19*, 2336.

[61] Y. Liu, N. Zhang, L. Jiao, J. Chen, *Adv. Mater.* **2015**, *27*, 6702.

[62] M. D. Goodman, S. Kim, N. Tatsuda, K. Yano, P. V. Braun, *Part. Part. Syst. Charact.* **2015**, *32*, 928.

[63] J. L. Goldman, B. R. Long, A. A. Gewirth, R. G. Nuzzo, *Adv. Funct. Mater.* **2011**, *21*, 2412.

CHAPTER 2
IRON(II) FLUORIDE CONVERSION CATHODES THROUGH USE OF A CONDUCTIVE 3D SCAFFOLD AND ALD COATING

The content of this chapter was previously published in: "Improved performance in FeF_2 Conversion Cathodes through use of a Conductive 3D scaffold and Al_2O_3 ALD coating", Sanghyeon Kim, Jinyun Liu, Ke Sun, Shen J. Dillon and Paul V. Braun, Advanced Functional Materials, 27, 1702783, 2017.

2.1 Introduction

Extensive research has been carried out on materials for LIBs given the importance of energy storage for applications ranging from portable electronics to transportation[1-3] and the fact that many key performance attributes, including the energy density of LIBs, are mostly determined by the electrode materials. While high capacity anode materials such as Si, Sn, and Fe_2O_3 have been widely demonstrated, [4-6] development of high capacity cathode materials has not been as successful. The most commonly used cathode materials are lithium transition metal oxides such as $LiCoO_2$.[1] Although they show good cycling stability, their specific capacities are limited by their storing Li^+ via intercalation, generally allowing a maximum of one Li to be accommodated per transition metal cation.[7] This has led to interest into conversion compound based electrodes, which provide high specific capacities by utilizing all possible redox states of metal ions.[7,8]

Among many conversion compounds, FeF_2 is one of the most promising candidates for positive electrode due to its high thermodynamic reduction potential (2.66 V vs. Li/Li^+), its high specific capacity (571 mA h g^{-1}), low cost, and low toxicity.[9-12] During discharge, FeF_2 is reduced with Li forming a bicontinuous Fe network embedded in a LiF matrix. The reverse reaction occurs during charging ($FeF_2 + 2Li \leftrightarrow Fe + 2LiF$).[13,14] However, the poor electrical conductivity of FeF_2, combined with sluggish kinetics and large structural changes during cycling have resulted in an overall poor electrochemical performance, limiting the application of FeF_2.[7,15,16]

Carbon-FeF_2 nanocomposites have been evaluated as a route to address these issue.[11,17-20] Carbon enhances the conductivity of the electrode, and a nanostructured design

can facilitate the conversion reaction kinetics owing to the increased surface area and decreased electron and ion diffusion lengths. However, high capacities could only be achieved at elevated temperature or low current densities, accompanied by rapid capacity decay.

Previous studies have suggested that capacity decay during cycling might be due to the incomplete reconversion of Fe and LiF to FeF_2.[13,21] Further capacity decay may result from metal dissolution into the electrolyte, because newly formed Fe metal and LiF is exposed to the electrolyte each cycle.[19,22] Direct contact of cathodes with electrolyte, absent a stable solid electrolyte interphase, is generally unfavorable as it can cause many side reactions.[23] Therefore, an approach which protects the electrode surface from electrolyte during cycling needs to be considered.

This chapter describes the fabrication of a three dimensional conductive scaffold supported Al_2O_3 coated FeF_2 electrode and demonstrates how the 3D metal scaffold and Al_2O_3 coating improve the electrochemical performance of FeF_2. The electrodes were prepared by electrodeposition and fluorination, and coated with thin layer of Al_2O_3 by ALD. To the best of my knowledge, this is a first report describing the synthesis of 3D scaffolded metal fluorides. The porous electrode structure accommodates the large volume changes of the conversion compound during cycling. Relative to previous work, the reaction kinetics of FeF_2 with Li^+ were improved, likely because the active materials are in close contact with both a current collector and electrolyte. The enhanced capacity retention resulting from the Al_2O_3 ALD coating without suppression of electrode reaction kinetics was observed.

2.2 Results and discussion

Figure 2.1 shows a schematic of the 3D Ni@FeF_2 electrode fabrication. The Ni inverse opal serving as a 3D conductive scaffold was made via Ni electrodeposition through a PS colloidal template. Fe metal nanoparticles were first deposited onto the Ni scaffold using pulsed electrodeposition. Pulse electrodeposition was then employed to deposit a conformal coating of Fe nanoparticles throughout Ni scaffold. The amount of Fe deposited was controlled by the number of pulses. The Fe nanoparticles were then selectively fluorinated into FeF_2 using a AgF_2 decomposition method. When AgF_2 is heated, it generates fluorine gas; [24] the F_2 gas then reacts with Fe forming FeF_2. Relative to other fluorination methods using fluorine gas or

hydrofluoric acid which are dangerous and require complicated experimental set ups,[25-27] this method is facile and safe. Here, the method is optimized for the synthesis of FeF_2, however, the synthesis of other metal fluorides should also be possible by this route. Finally, ALD was used to coat the structure with 1~2 nm of Al_2O_3. The surface roughness before and after ALD appears similar in SEM (Figure 2.2) because the ALD coating layer is ultrathin (~1.5 nm), and thus largely electron transparent. Since ALD was performed at low temperature (80 ℃), there was no sintering of the underlying morphology.

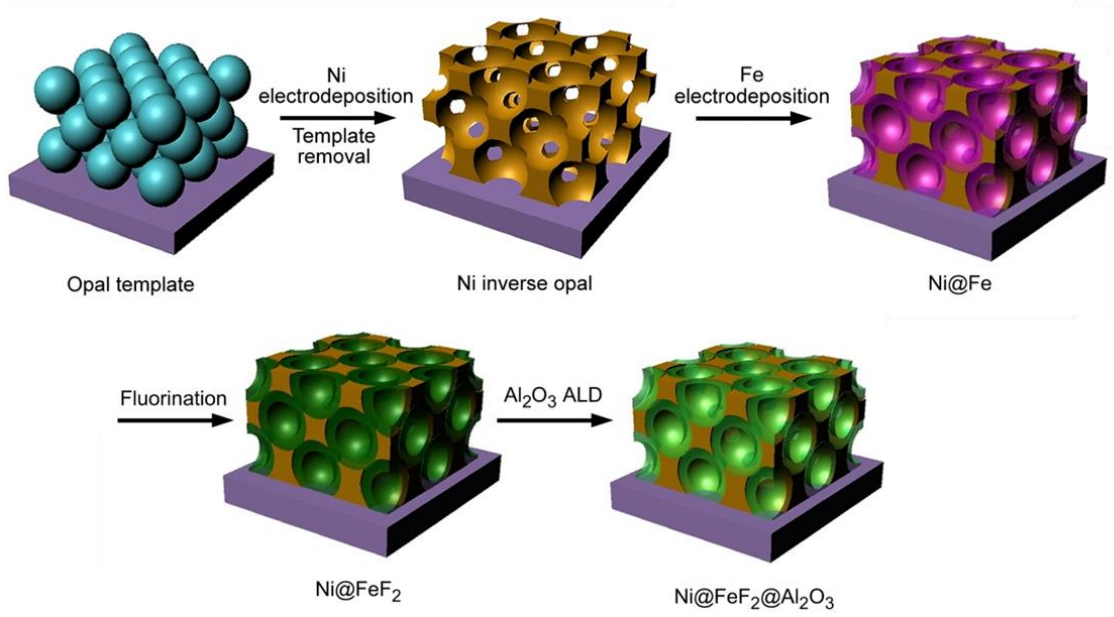

Figure 2.1 Schematic illustration of the 3D $Ni@FeF_2@Al_2O_3$ electrode fabrication process.

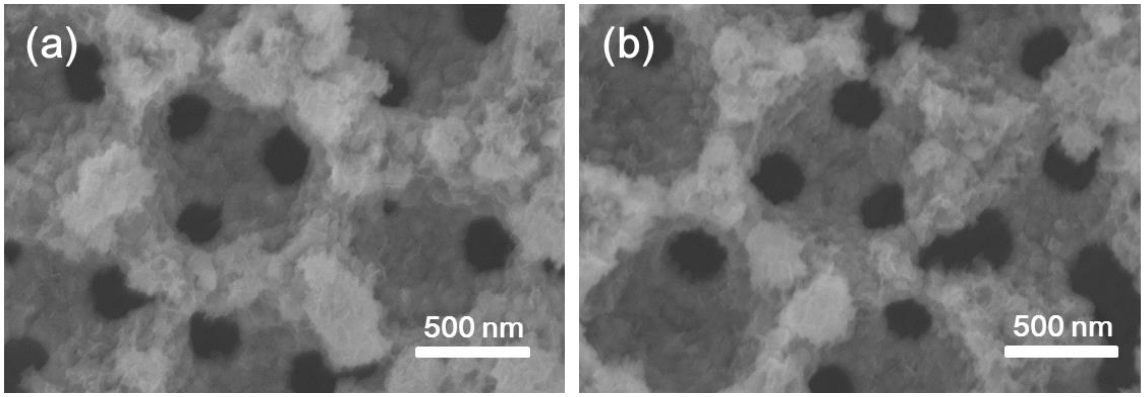

Figure 2.2 Top view SEM images of $Ni@FeF_2$ electrodes (a) before and (b) after 1.5 nm Al_2O_3 ALD coating.

Figure 2.3 shows that Fe metal particles were uniformly coated on the Ni inverse opal. A SEM image of the fluorinated Ni@Fe is presented in Figure 2.3c. A slight volume expansion of the active material was observed, probably due to the conversion of Fe to FeF_2. At room temperature (the Fe electroplating temperature), Fe does not react with Ni, however, I was concerned Fe and Ni might react during the fluorination process. To determine if this could occur, I refer to a previous study which suggested the interatomic diffusivity in Fe/Ni multilayers is about 2.1 x 10^{-19} cm^2 s^{-1} at 300 ℃.[28] Based on a simple diffusion calculation, interatomic diffusion at 300 ℃ for 1 h might yield a reacted layer about 0.5 nm thick. Since fluorination process was done at even lower temperature (250 ℃) where the thickness of the reacted layer would be even less, I assume interatomic diffusion can be neglected. Also, a Ni signal is not been detected in the XPS measurement indicating Ni has not diffused through the Fe layer (the probe depth of XPS is at most 10 nm).

The 3D FeF_2@Ni retains its open porous structure with a pore size between voids of ca. 200 nm after fluorination. One attribute of the inverse opal structure is its ability to accommodate the volume expansion of the active materials (about 50 % for FeF_2)[25] during cycling and facilitate electrolyte infiltration into the electrode. The HRTEM image in Figure 2.3d displays lattice fringes of 0.33nm, corresponding to the (1 1 0) d-spacing of tetragonal FeF_2. SAED (Figure 2.4c) shows the polycrystalline nature of FeF_2.

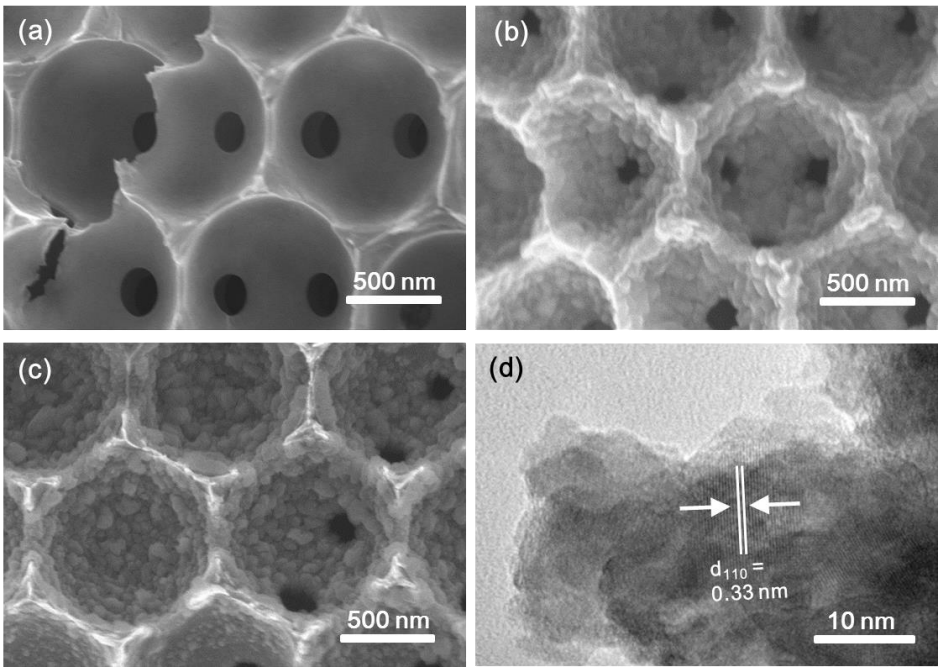

Figure 2.3 Cross-sectional SEM images of (a) 3D Ni, (b) 3D Ni@Fe and (c) Ni@FeF_2 inverse opals. (d) HRTEM image of a small piece of the 3D Ni@FeF_2 electrode.

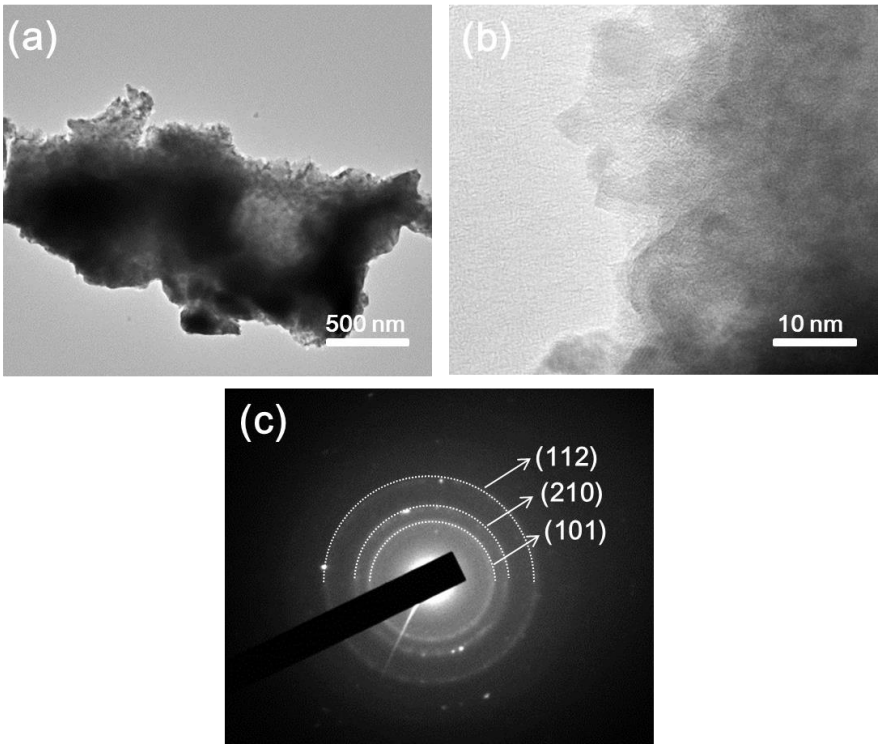

Figure 2.4. (a) TEM and (b) HRTEM images of 3D Ni@FeF_2 electrodes, and corresponding SAED pattern, taken from (b) region.

XRD was performed on Ni@Fe and Ni@Fe_2 samples. Metallic Fe was confirmed by XRD (Figure 2.5). Figure 2.5b shows that all peaks in XRD pattern other than that of Ni and W match FeF_2. No metallic Fe was observed after fluorination, indicating that Fe was fully converted into FeF_2. The average FeF_2 grain size, calculated by the Scherrer equation,[26] is about 12 nm. XPS analysis (Figure 2.5c) also agrees with conversion of Fe into FeF_2. The Fe 2p XPS spectra measured from Fe and FeF_2 are shown in Figure 2.5c. The shift of the binding energy scale was corrected with respect to the C 1s peak (285 eV). The Fe 2p XPS of Fe is mainly composed of characteristic Fe^{3+} signal with two main peaks and satellite peaks. This is presumably because a few nanometers of outer surface of Fe is oxidized to Fe_2O_3. Fe 2p3/2 peak for metallic Fe is shown at around 707 eV.[14] After the fluorination, all satellite peaks of Fe^{3+} disappeared and Fe^{2+} peaks were formed.[14,29] The Fe 2p line shape well matches characteristic of FeF_2,[14] indicating that FeF_2 was converted from Fe. Also, no oxide formation was observed during the fluorination. Since Ni is covered by Fe, the possible oxide which can be formed primarily during fluorination would be iron oxide. No iron oxide phases were found in the TEM analysis (Figure 2.3d and Figure 2.4). Moreover, In XPS, all satellite peaks of Fe^{3+} disappeared after the fluorination, indicating that any existing Fe_2O_3 was converted into FeF_2 (Figure 2.5c).

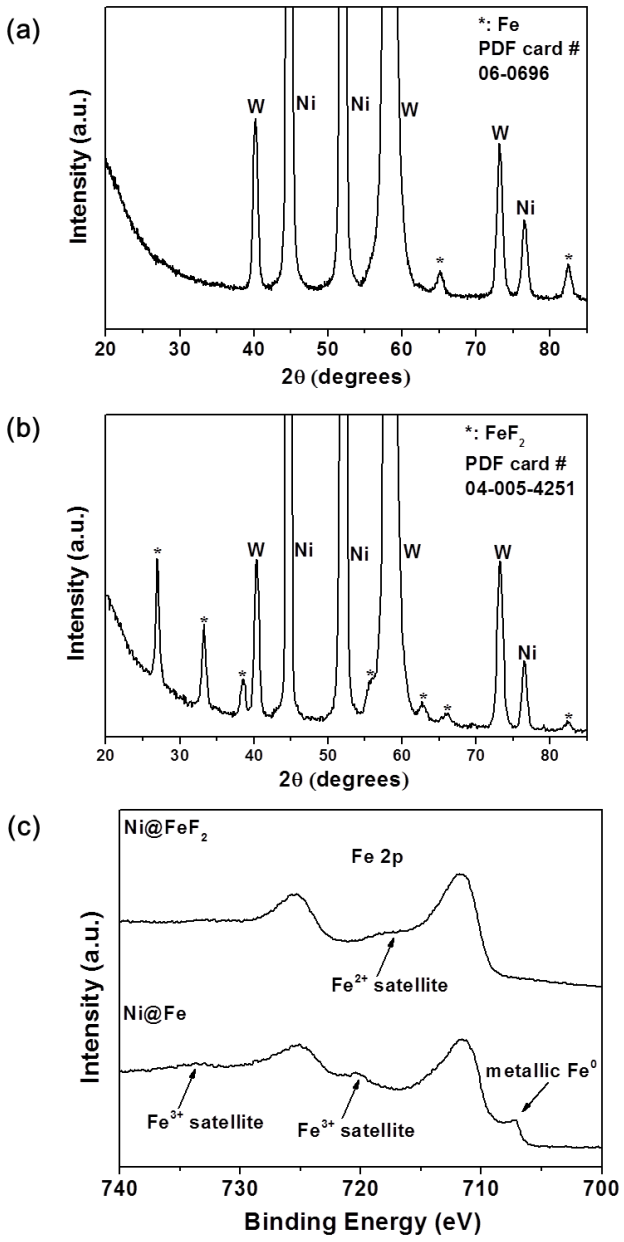

Figure 2.5 XRD and XPS before and after fluorination. XRD of (a) a 3D Ni@Fe and (b) 3D Ni@Fe@FeF_2. (c) XPS spectra of Fe 2p region obtained from 3D Ni@Fe and Ni@FeF_2 samples.

The AgF_2 decomposition method is highly oxidizing but what I suspect is occurring is that the F_2 gas reacts preferentially with Fe over oxygen because of its high reactivity and because 250 ℃ is too low of a temperature for significant oxide formation especially considering the low gas pressure inside the reactor (~10^{-5} mbar, ~10^{-6} Torr). Finally, to determine if nickel

fluoride could be formed, a bare nickel inverse opal was treated using the same fluorination process. XRD (Figure 2.6a) and EDS (Figure 2.6b), indicate nickel fluoride was not formed.

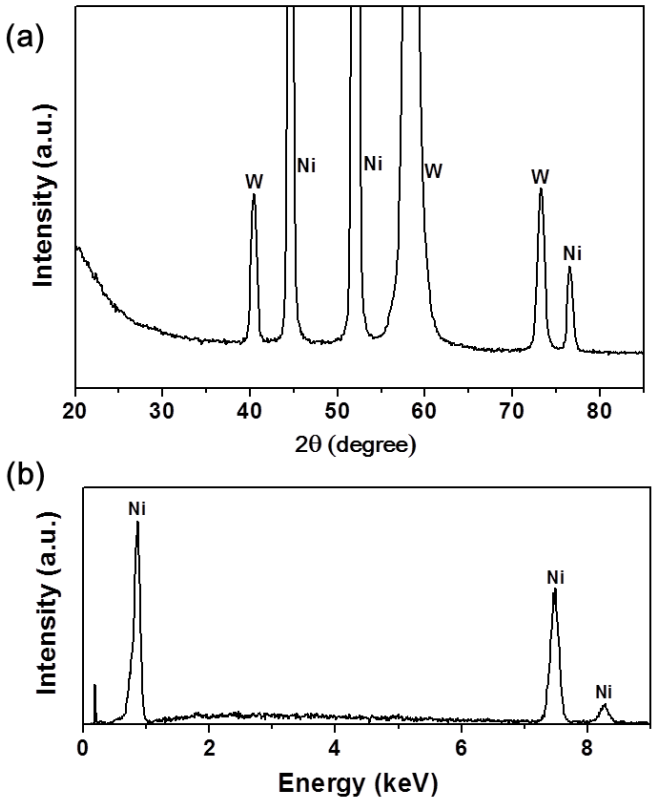

Figure 2.6 (a) XRD and (b) EDS spectrum of a Ni inverse opal sample after it the fluorination process. Nickel fluoride was not observed.

The active material loading and ALD coating thickness which provided the best electrochemical performance was determined. First, the effect of FeF_2 loading on the electrochemical performance of the 3D Ni@FeF_2 electrode was examined. All variables, except FeF_2 loading, including electrode area and thickness were identical across all samples. The specific capacities of three electrodes with different loadings at varying current densities are represented in Figure 2.7a. The electrodes were cycled 5 times at each current density. As the FeF_2 loading increases, the specific capacity decreases. Higher FeF_2 loadings lead to longer electron and ion diffusion lengths, resulting in slow reaction kinetics. A higher active material loading also leads to narrower pores which may reduce Li ion transport ability due to limited

electrolyte accessibility.[32,33] A significant capacity drop was observed in the electrode with a loading of 0.94 g cm^{-3}, so the electrode with a loading of 0.75 g cm^{-3} was chosen for most studies.

To avoid electrode degradation during cycling, an ultrathin (<2 nm) layer of Al_2O_3 was coated on Ni@FeF_2 by ALD; a common method for depositing ultrathin conformal coatings. Figure 2.7b shows how cycling stability changes with Al_2O_3 coating thickness. All electrodes were cycled at 200 mA g^{-1} and had the same FeF_2 loading (around 0.75 g cm^{-3}). As the Al_2O_3 thickness increases, cycling stability is improved. However, a large drop in initial capacity was observed for 2 nm thick Al_2O_3 coatings even though this thickness provided the most stable cycling behavior. This is perhaps because the thicker coating begins to significantly restrict Li diffusion.[34] On the basis of these results, 1.5 nm was determined to be a good Al_2O_3 coating thickness for our electrodes.

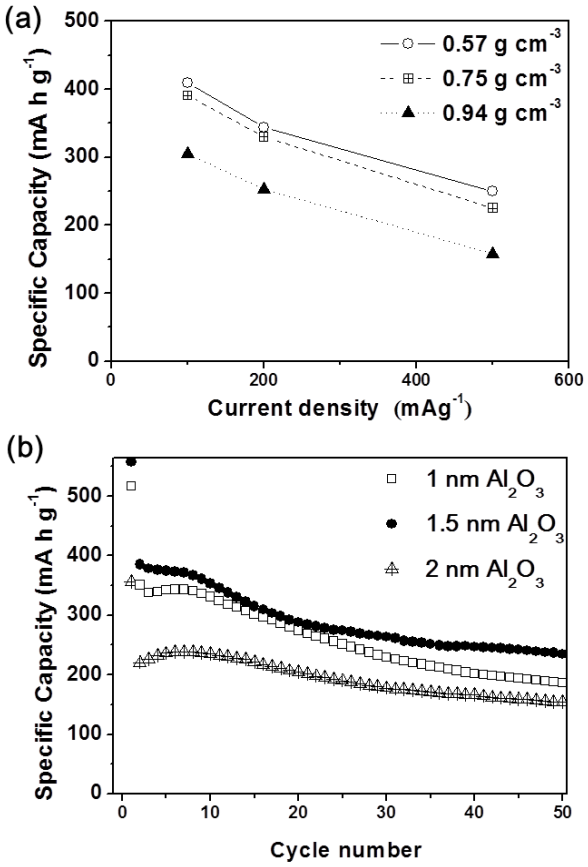

Figure 2.7 (a) Specific capacity of Ni@FeF_2 electrodes with different active material loadings at various current densities. (b) Specific capacities versus cycle number for 1, 1.5, and 2 nm-thick Al_2O_3 coated Ni@FeF_2 electrodes. All electrodes have the same active material loading (around 0.75 g cm^{-3}), and were cycled at 200 mA g^{-1}.

The electrochemical properties of FeF_2 electrodes were evaluated by galvanostatic discharge/charge tests at room temperature. Figure 2.8a shows the cycling performance of 3D Ni@FeF_2 electrodes with and without 1.5 nm Al_2O_3 coating at a current density of 200 mA g^{-1} over 100 cycles. 3D Ni@FeF_2 and Ni@FeF_2@Al_2O_3 electrodes exhibit 557 and 473 mA h g^{-1} for the first discharge capacity, respectively. These correspond to 97.5 % and 87.8 % of the respective electrode theoretical value, indicating high active material utilization. After a few cycles, the uncoated electrode shows a similar capacity as the Al_2O_3 coated electrode. The capacity of the uncoated electrode then continues to decay more rapidly compared to the Al_2O_3 coated electrode. The Coulombic efficiency of the coated electrode exceeds that of the bare

electrode after 22 cycles, gradually increases to 99 % after 60 cycles and remains above 99 % through 100 cycles. After 100 cycles, the capacity of the Al_2O_3 coated electrode is about 200 mA h g^{-1}. Considering the testing condition (200 mA g^{-1}, room temperature), this result is comparable or even better than the previous reported values for FeF_2 which were generally cycled at lower current densities (20-50 mA g^{-1}) and higher temperatures,[11,17,21,35] perhaps due to the combination of the highly conductive 3D metal scaffold and the ALD coating. Good electrical conductivity is important since FeF_2 is an electrical insulator. The porous nature of the electrode provides a path for Li ion transport and provides a large surface area.[36] Furthermore, this electrode structure accommodates the large volume changes of FeF_2. While this is not easy to observe in SEM images, in Figure 2.9, the lithiated electrode appears denser, and the windows between the voids left by the colloids appear smaller. The structure can accommodate a 50% volume expansion while any degradation of the structure due to the swelling during cycling was not observed. Previous research has shown that fast conversion reactions can be achieved when active material nanoparticles are in direct contact with a current collector,[30] as is the case in this work.

The Al_2O_3 coated FeF_2 second cycle discharge capacity is about 280 mA h cm^{-3}, higher than the previously reports for composite cathodes.[37,38] It is expected that even higher volumetric capacity 3D FeF_2 electrodes could be formed by optimizing the Ni inverse opal structure, something that is possible both through varying the diameter of the colloids forming the PS template and by Ni electropolishing.[36]

Figure 2.8b shows the initial two discharge-charge curves of the Ni@FeF_2@Al_2O_3 electrode, which are typical of FeF_2.[17-18] In the first discharge, a long plateau at around 1.6 V is observed which can be attributed to the reduction of FeF_2 to α-Fe and LiF.[13,18,39] After the first discharge, two stages are observed in the second discharge curve. The lithium uptake by FeF_2 at high potentials without conversion resulted in the steep slope to around 2.15 V; this effect is commonly observed in conversion compounds.[17,39] This lithium uptake may be due to interfacial lithium storage made possible by phase segregation through conversion and deconversion reactions,[7] and the formation of mixed or nonstoichiometric fluoride phases which could have some capacity at higher voltages. The second slope represents the conversion reaction. The voltage plateau in the second discharge curve exhibits a higher reaction potential than that in first discharge curve perhaps due to the reduction of particle size after conversion

reaction.[13] Improved reaction kinetics due to smaller nanoparticles after the first cycle reduces the overpotential, resulting in a higher reaction potential. dQ/dV curves were obtained by differentiating the charge/discharge voltage curves (Fig 2.8c). The dQ/dV curves show the reaction peaks more clearly. Interestingly, two peaks were observed in the charge reaction curves, indicating that deconversion reaction consists of two steps, probably conversion and intercalation. The voltage hysteresis of $Ni@FeF_2@Al_2O_3$ in this work, defined as the voltage difference where half of charge capacity and discharge capacity were delivered, is about 1.2 V in contrast to the typical ~1.7 V hysteresis for conventional slurry-cast FeF_2-based electrodes.[11,30]

The rate performance of the 3D $Ni@FeF_2@Al_2O_3$ electrode was evaluated by cycling the electrode at different current densities. When the current density increased from 50 to 100 and 200 mA g^{-1}, the electrode delivered 88 and 70 % of its 50 mA g^{-1} capacity, respectively (Figure 2.8d). Even at 1000 mA g^{-1}, the electrode still delivered 32 % capacity retention indicating that the slow reaction kinetics of conversion compounds can be enhanced by a 3D conductive scaffold. Moreover, when the rate returns from 1000 to 50 mA g^{-1}, about 83 % of the 50 mA g^{-1} capacity was recovered.

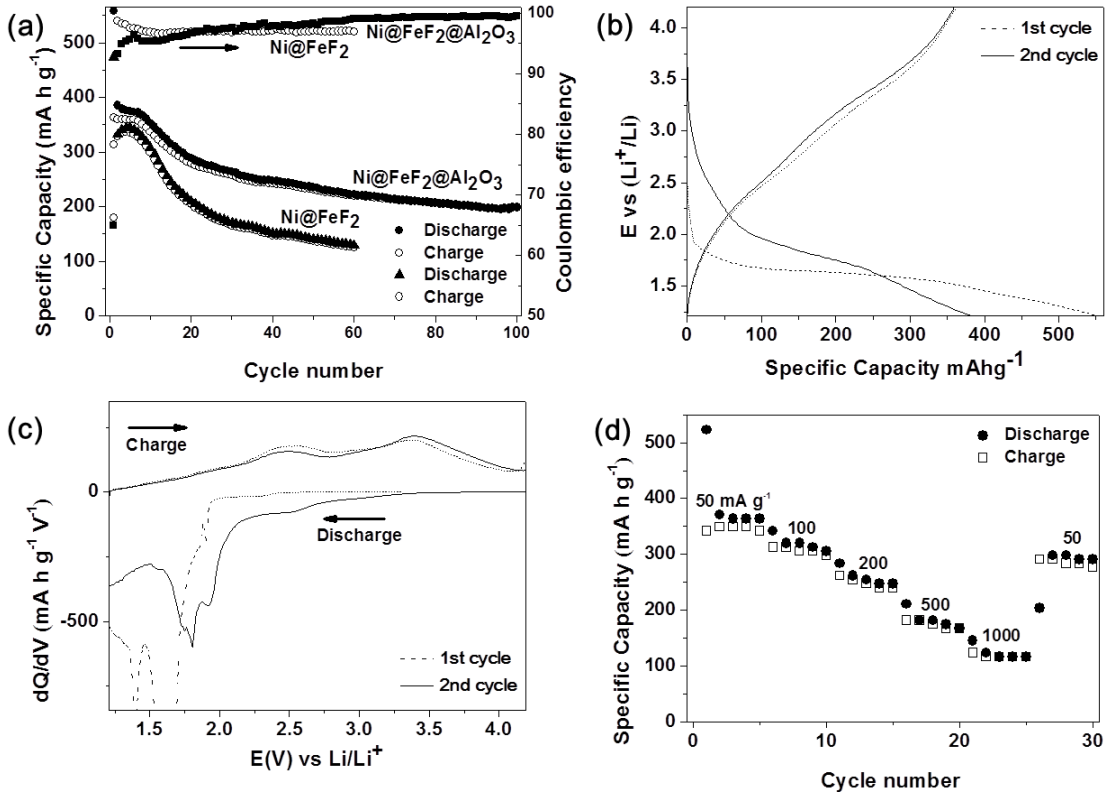

Figure 2.8 (a) Cycling performance of 3D Ni@FeF_2@Al_2O_3 and Ni@FeF_2 at 200 mA g^{-1}. (b) 1st and 2nd cycle discharge-charge curves of 3D Ni@FeF_2@Al_2O_3 at 200 mA g^{-1}. (c) Differential capacity plot for cycles presented in Fig 2.8b. (d) Rate performance of 3D Ni@FeF_2@Al_2O_3 electrodes. All electrodes have the same active material loading (around 0.75 g cm^{-3}).

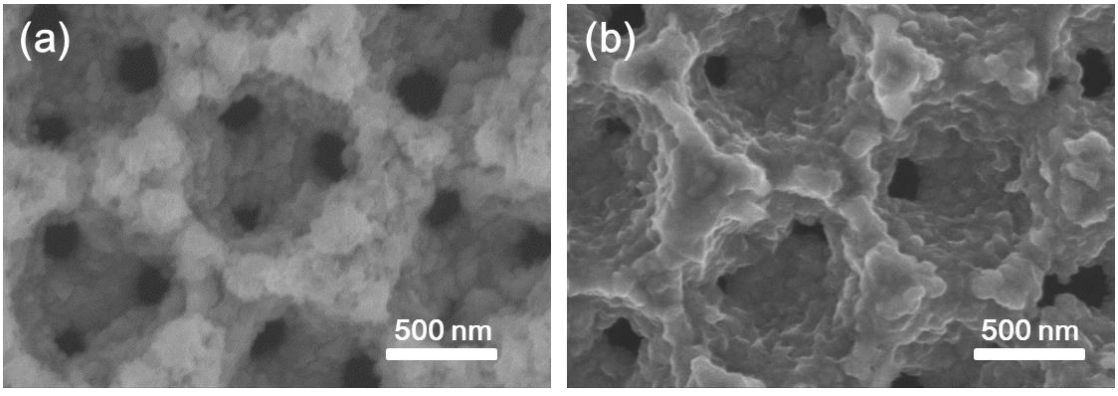

Figure 2.9 Top view SEM images of Ni@FeF_2 electrodes (a) before cycling and (b) after first discharge.

To investigate the reason behind the different behavior of the bare and Al_2O_3 coated electrodes, XPS was performed on uncycled and cycled 10 times bare electrodes, and 10 times cycled Al_2O_3 coated electrodes (Figure 2.10). Duplicate experiments were performed for all samples and the same XPS results were obtained for all duplicate experiments. XPS spectra in Figure 2.10 were normalized for comparison. Carbon was detected on uncycled bare electrodes due to natural carbon contamination.[40] While the C 1s signal obtained from 10 times cycled Al_2O_3 coated electrode is almost same as that obtained from the uncycled bare electrode, new two prominent peaks were observed in the 10 times cycled bare electrode. After 10 cycles, for the bare electrode, C 1s signals at 290.3 eV and 287 eV due to C-F and C-O bonds, respectively,[41] were observed. Since no binder, carbon black or $LiPF_6$ salt were used, FeF_2 and electrolyte should be the only sources for F and C. The C-F bond formation is thus evidence for a side reaction between FeF_2 and electrolyte. The C-O bond formation also indicates the electrolyte decomposition on the surface of electrode. A similar trend was observed in the F 1s spectra (Figure 2.10b). The F 1s spectra obtained from uncycled bare electrodes and 10 times cycled Al_2O_3 coated electrodes contains just one peak at 685.2 eV which is a characteristics of F^- in FeF_2.[40] However, C-F peaks were observed in the F 1s spectrum at 688.3 eV for the 10 times cycled bare electrode.[42]

Unlike in the C 1s and F 1s spectra, peak position shifts or new peaks were not observed in Fe 2p spectra after cycling for all samples (Figure 2.10c) but, the Fe 2p intensity was much smaller for the bare vs. the Al_2O_3 coated electrodes after 10 cycles. Since XPS only detects at most the top 10 nm of a material, the reduced Fe 2p intensity from the bare electrode might be due to formation of an over layer or Fe loss by dissolution. Both this possibilities have been supported by previous studies which suggest that electrolyte decomposes on the surface of FeF_2, and metal ions in metals fluorides can become soluble in electrolyte during cycling.[19,21] In summary, based on the XPS data, I suspect that FeF_2 undergoes chemical degradation when cycled directly in contact with a carbonate based electrolyte and the ALD coating prevents this side reaction by limiting contact of the electrode with the electrolyte.

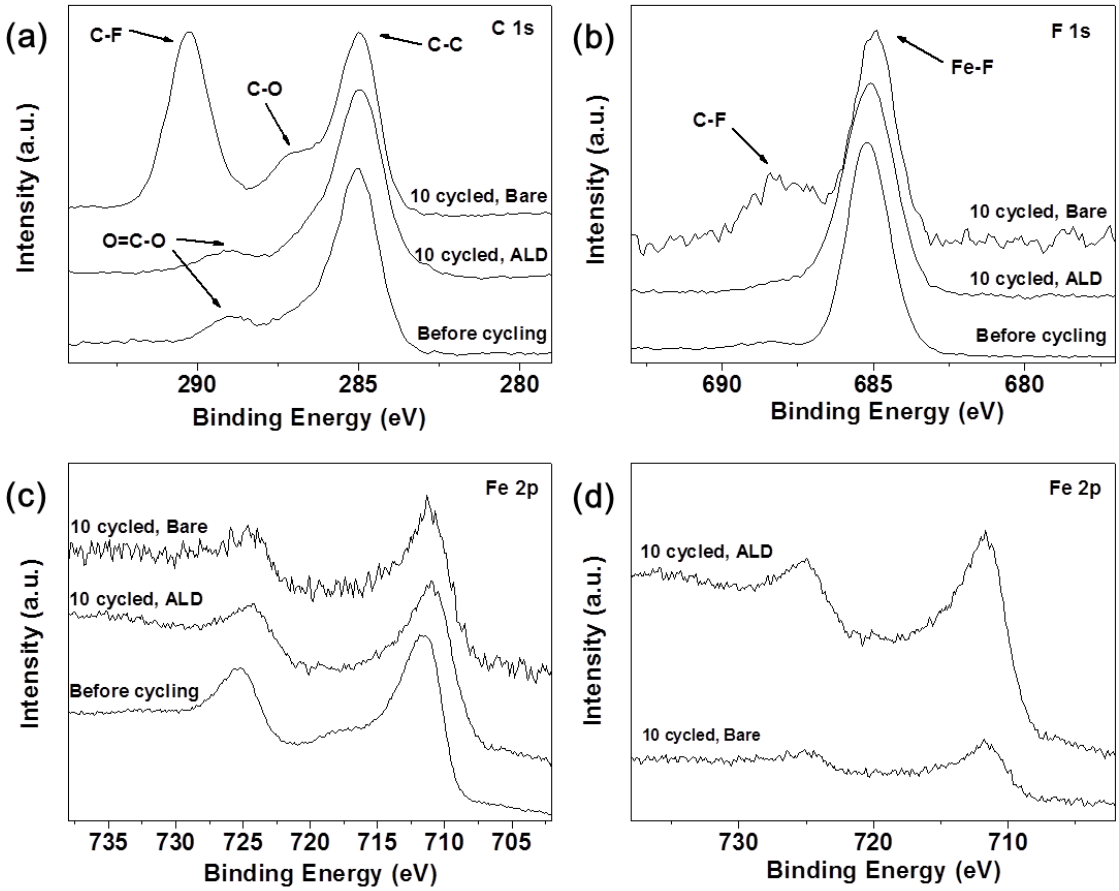

Figure 2.10 Normalized XPS spectra of (a) C 1s, (b) F 1s and (c) Fe 2p region obtained from uncycled and 10 times cycled Ni@FeF_2 electrodes and a Ni@FeF_2@Al_2O_3 electrode cycled 10 times. (d) Original XPS spectra of Fe 2p region obtained from 3D Ni@FeF_2@Al_2O_3 and Ni@FeF_2 electrodes cycled 10 times.

To additionally evaluate the effect of the Al_2O_3 coating, differential capacity data for bare and Al_2O_3 coated electrodes for the 2^{nd}, 5^{th} and 10^{th} cycles (Figure 2.11) was examined to determine how surface reactions affect reaction kinetic. All oxidation and reduction peaks from the Al_2O_3 coated electrode overlap well from the 2^{nd} to 10^{th} cycle, indicating stable and reversible electrochemical reactions. However, the peak positions in the bare sample changes with cycling. In cathodic reaction, the conversion reaction peak moves toward lower voltage as cycling proceeds. This is due to increasing overpotential perhaps related to growth of an electrochemically inactive layer. This suggests side reactions between the electrode and

electrolyte affect the reaction kinetics. As described in the above, the deconversion reaction of FeF_2 consists of two steps, probably conversion and intercalation. Two oxidation peaks are clearly shown in the ALD coated sample which change little with cycling. In the bare sample, the first oxidation peak is disappearing with cycling, indicating the deconversion is incomplete. Therefore, the rapid capacity decay in bare sample can probably be attributed to incomplete deconversion lowering the utilization of active materials.[19,21,22] The ALD coating appears helpful to maintain the reversible electrochemical reaction.

The overall capacity behavior of $Ni@FeF_2@Al_2O_3$ electrode can be explained as follows (Figure 2.8a). I suspect that some SEI forms on the surface of the Al_2O_3 ALD coating during the first few cycles, and perhaps there are also defects in the Al_2O_3 coating which become passivated with additional cycling. Initial contact between the electrolyte and any exposed FeF_2, leads to capacity decay but capacity decay stabilizes with growth of the SEI layer.

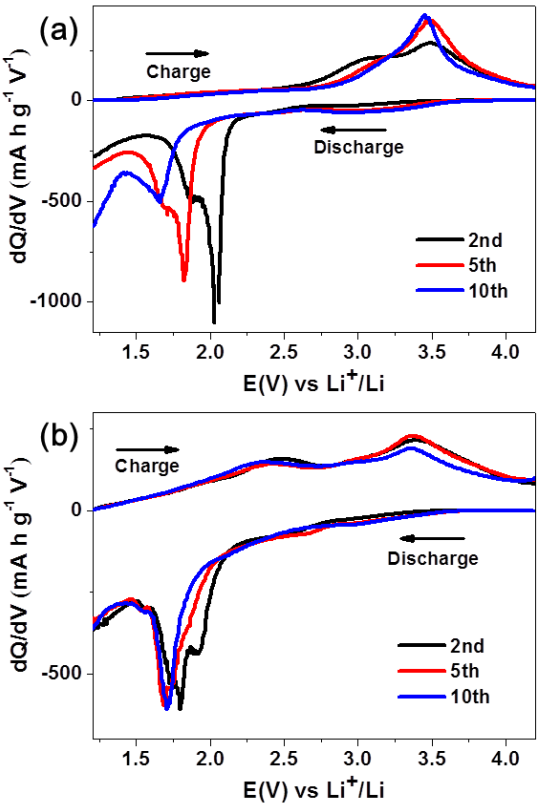

Figure 2.11 Differential capacity plot of (a) $Ni@FeF_2$ and (b) $Ni@FeF_2@Al_2O_3$ cycled at 200 mA g^{-1} for the 2^{nd}, 5^{th} and 10^{th} cycles.

2.3 Conclusions

Ni supported 3D FeF_2 electrodes were fabricated by Fe metal electrodeposition combined with a facile fluorination method and Al_2O_3 ALD. The 3D scaffold enables a high specific capacity by providing an efficient electron pathway to the insulating FeF_2, and while there is still capacity fade in the coated electrode, the Al_2O_3 coating does improve both the Coulombic efficiency and capacity retention. The thin Al_2O_3 layer appears to reduce the degree of reaction between the active material and the electrolyte, improving the cycle life relative to that commonly observed in fluoride based conversion compounds. This work demonstrates that a 3D conductive scaffold, coupled with a thin surface coating on the active material, reduces several of the drawbacks of a FeF_2-based electrode, specifically the typical sluggish reaction kinetics and rapid capacity fade. It is worth noting that the fabrication method presented here can be applied for synthesis of other metal fluoride materials on different types of 3D conductive scaffolds.

2.4 Experimental section

Sample preparation: A tungsten substrate (Sigma-Aldrich) was sonicated in concentrated ethanolic KOH for 30 min, rinsed with millipore water, and dried. A PS suspension (0.2 wt %) was prepared by dispersing 1 μm PS spheres (Molecular Probes) in millipore water. The tungsten substrate was vertically placed into vials filled with the PS suspension at 55 ℃ overnight. The substrate was taken out from the vials before the solution completely evaporated and subsequently annealed at 96 ℃ for 3 h to strengthen the adhesion between PS spheres and to increase the interconnect size between the PS spheres. Electrodeposition of Ni was performed by applying -1.5 mA cm^{-2} in a commercial Ni plating solution with the sample as the working electrode and a nickel plate as a counter electrode. After the deposition, the sample was immersed into toluene to dissolve the PS template and Ni inverse opal was obtained. The final electrode thickness was typically about 6 μm.

Fe metal nanoparticles were electrodeposited on the Ni inverse opal by pulsed-voltage electrodeposition in a 0.375 M $FeSO_4$ solution. Platinum foil and a Ag/AgCl electrode saturated by 3M NaCl (BASi Inc.) were used as the counter electrode and reference electrode, respectively. The cathodic pulses consisting of -0.8 V vs Ag/AgCl for 0.3 s and -1.6 V vs Ag/AgCl for 10s were applied repeatedly. The amount of Fe metal deposited is proportional to the number of

pulses applied. The sample was washed with Millipore water and ethanol and dried in vacuum oven. The sample was placed in a quartz reactor with Silver (II) fluoride (AgF_2, Sigma Aldrich) to convert Fe metal into FeF_2. The sample and AgF_2 were spatially separated in the reactor and AgF_2 is not in direct contact with the electrode in the reactor (Figure 2.12). Silver (II) fluoride was used as a fluorine precursor. The reactor was evacuated to 10^{-5} mbar and then heated to 250 ℃ for 1h. The thin layer of Al_2O_3 was deposited on the sample in a Cambridge Nanotech ALD system at 80 ℃. The growth rate was 0.9 nm per cycle.

Figure 2.12 Illustration of the fluorination process. The reactor is sealed and under vacuum.

Characterization: Sample morphologies were confirmed using a Hitachi S-4800 SEM. EDS was done using a Hitachi S-4700 SEM equipped with an Oxford INCA energy-dispersive X-ray analyzer. The crystal structures were investigated by a Philips X'pert MRD XRD using Cu Kα radiation (λ = 0.15418 nm). The crystal structures were also confirmed by electron diffraction in a JEOL 2100 Cryo TEM. XPS spectra were obtained with a Kratos Axis Ultra XPS system with a monochromatic Al Kα (1486.6 eV) source. The amount of active materials was determined by inductively coupled plasma (ICP-MS) analysis. For postmortem SEM and XPS analysis after cycling, electrodes were washed with DMC multiple times and dried in the glove box prior to analysis.

Electrochemical Measurements: 1.0 M $LiClO_4$ in EC/DMC (1:1 by vol) was used as electrolyte and lithium foil was used as counter electrode for two-electrode cell. All cells were assembled in the glove box under Argon atmosphere. Galvanostatic discharge/charge tests were conducted on potentiostat (VMP3, Bio-Logic) in a jar cell over the range of 1.2 to 4.2 V.

2.5 References

[1] M. Armand, J.-M. Tarascon, *Nature* **2008**, *451*, 652.

[2] J. B. Goodenough, *Acc. Chem. Res*. **2012**, *46*, 1053.

[3] J.-M. Tarascon, M. Armand, *Nature* **2001**, *414*, 359.

[4] H. Wu, G. Zheng, N. Liu, T. J. Carney, Y. Yang, Y. Cui, *Nano Lett.* **2012**, *12*, 904.

[5] G. Derrien, J. Hassoun, S. Panero, B. Scrosati, *Adv. Mater.* **2007**, *19*, 2336.

[6] X. Zhu, Y. Zhu, S. Murali, M. D. Stoller, R. S. Ruoff, *Acs Nano* **2011**, *5*, 3333.

[7] J. Cabana, L. Monconduit, D. Larcher, M. R. Palacin, *Adv. Mater.* **2010**, *22*. E170.

[8] P. Poizot, S. Laruelle, S. Grugeon, L. Dupont, J. Tarascon, *Nature* **2000**, *407*, 496.

[9] F. Badway, F. Cosandey, N. Pereira, G. Amatucci, *J. Electrochem. Soc.* **2003**, *150*, A1318.

[10] I. Plitz, F. Badway, J. Al-Sharab, A. DuPasquier, F. Cosandey, G. Amatucci, *J. Electrochem. Soc.* **2005**, *152*, A307.

[11] S. K. Martha, J. Nanda, H. Zhou, J. C. Idrobo, N. J. Dudney, S. Pannala, S. Dai, J. Wang, P. V. Braun, *RSC Adv.* **2014**, *4*, 6730.

[12] H. Li, P. Balaya, J. Maier, *J. Electrochem. Soc.* **2004**, *151*, A1878.

[13] F. Wang, R. Robert, N. A. Chernova, N. Pereira, F. Omenya, F. Badway, X. Hua, M. Ruotolo, R. Zhang, L. Wu, *J. Am. Chem. Soc.* **2011**, *133*, 18828.

[14] S. Rangan, R. Thorpe, R. A. Bartynski, M. Sina, F. Cosandey, O. Celik, D. D. Mastrogiovanni, *J. Phys. Chem. C* **2012**, *116*, 10498.

[15] L. Li, F. Meng, S. Jin, *Nano Lett.* **2012**, *12*, 6030.

[16] P. Liu, J. J. Vajo, J. S. Wang, W. Li, J. Liu, *J. Phys. Chem. C* **2012**, *116*, 6467.

[17] M. A. Reddy, B. Breitung, V. S. K. Chakravadhanula, C. Wall, M. Engel, C. Kübel, A. K. Powell, H. Hahn, M. Fichtner, *Adv. Energy Mater*. **2013**, *3*, 308.

[18] J. Zhou, D. Zhang, X. Zhang, H. Song, X. Chen, *ACS Appl. Mater. Interfaces* **2014**, *6*, 21223.

[19] W. Gu, A. Magasinski, B. Zdyrko, G. Yushin, *Adv. Energy Mater*. **2015**, *5*. 1401148.

[20] Y. Zhang, L. Wang, J. Li, L. Wen, X. He, *J. Alloys Compd.* **2014**, *606*, 226.

[21] M. Sina, R. Thorpe, S. Rangan, N. Pereira, R. A. Bartynski, G. G. Amatucci, F. Cosandey, *J. Phys. Chem. C* **2015**, *119*, 9762.

[22] X. Wang, W. Gu, J. T. Lee, N. Nitta, J. Benson, A. Magasinski, M. W. Schauer, G. Yushin, *Small* **2015**, *11*, 5164.

[23] X. Meng, X. Q. Yang, X. Sun, *Adv. Mater.* **2012**, *24*, 3589.

[24] W. Grochala, *J. Fluorine Chem.* **2008**, *129*, 82.

[25] Q. Chu, Z. Xing, J. Tian, X. Ren, A. M. Asiri, A. O. Al-Youbi, K. A. Alamry, X. Sun, *J. Power Sources* **2013**, *236*, 188.

[26] R. Ma, Z. Lu, C. Wang, H.-E. Wang, S. Yang, L. Xi, J. C. Chung, *Nanoscale* **2013**, *5*, 6338.

[27] H. Zhou, R. E. Ruther, J. Adcock, W. Zhou, S. Dai, J. Nanda, *ACS nano* **2015**, *9*, 2530.

[28] J. Liu, K. Barmak, *J. Vac. Sci. Technol. A* **2015**, *33*, 021510.

[29] Y. Ma, G. Ji, J. Y. Lee, *J. Mater. Chem.* **2011**, *21*, 13009.

[30] F. Wang, H.-C. Yu, M.-H. Chen, L. Wu, N. Pereira, K. Thornton, A. Van der Ven, Y. Zhu, G. G. Amatucci, J. Graetz, *Nat. Commun.* **2012**, *3*, 1201.

[31] T. C. Vaimakis, C. S. Skordilis, P. J. Pomonis, *J. Colloid Interface Sci.* **1995**, *172*, 311.

[32] H. Zhang, P. V. Braun, *Nano Lett.* **2012**, *12*, 2778.

[33] J. Wang, H. Zhou, J. Nanda, P. V. Braun, *Chem. Mater.* **2015**, *27*, 2803.

[34] Y. S. Jung, A. S. Cavanagh, A. C. Dillon, M. D. Groner, S. M. George, S.-H. Lee, *J. Electrochem. Soc.* **2010**, *157*, A75.

[35] N. Pereira, F. Badway, M. Wartelsky, S. Gunn, G. Amatucci, *J. Electrochem. Soc.* **2009**, *156*, A407.

[36] H. Zhang, X. Yu, P. V. Braun, *Nat. Nanotechnol.* **2011**, *6*, 277.

[37] C. Ban, Z. Wu, M. J. Kirkham, L. Chen, Y. S. Jung, E. A. Payzant, Y. Yan, M. S. Whittingham, A. C. Dillon, *Adv. Energy Mater.* **2011**, *1*, 58.

[38] M. Hara, H. Nakano, K. Dokko, S. Okuda, A. Kaeriyama, K. Kanamura, *J. Power Sources* **2009**, *189*, 485.

[39] N. Yamakawa, M. Jiang, B. Key, C. P. Grey, *J. Am. Chem. Soc.* **2009**, *131*, 10525.

[40] R. Thorpe, S. Rangan, R. Whitcomb, A. C. Basaran, T. Saerbeck, I. K. Schuller, R. A. Bartynski, *Phys. Chem. Chem. Phys.* **2015**, *17*, 15218.

[41] K. Bomben, J. Moulder, P. E. Sobol, W. Stickle, *Handbook of X-ray Photoelectron Spectroscopy. A Reference Book of Standard Spectra for Identification and Interpretation of XPS data, Physical Electronics, Eden Prairie, Minnesota, **1995**.*

[42] R. Dedryvere, S. Leroy, H. Martinez, F. Blanchard, D. Lemordant, D. Gonbeau, *J. Phys. Chem. B.* **2006**, *110*, 12986.

CHAPTER 3
REDUCED GRAPHENE OXIDE/LITHIUM IODIDE COMPOSITE CATHODES

The content of this chapter was previously published in: "Reduced graphene oxide/LiI composite lithium ion battery cathodes", Sanghyeon Kim, Sung-Kon Kim, Pengcheng Sun, Nuri Oh and Paul V. Braun, Nano Letters, 17, 6893-6899, 2017.

3.1 Introduction

Demand for high energy and power density secondary batteries for a range of technologies, including next-generation hybrid and all-electric vehicles,[1-3] has led to considerable research in batteries which provide both high power and charge acceptance, without a significant reduction in energy. The Li-iodine system ($I_2 + 2Li \leftrightarrow 2LiI$) has been considered promising because of fast electrochemical conversion of the iodine/triiodide redox pair and high reaction potential with lithium.[4-6] However, to date, there have been only a few reports on rechargeable Li-iodine cells,[7-11] because of several issues including the following: iodine is highly soluble in aprotic electrolytes, leading to self-discharge due to shuttling;[7] Li-iodine cells generally use Li metal as an anode, however, Li metal can form dendrites during cycling which lead to shorting;[12] iodine is volatile even at room temperature, leading to cell fabrication challenges;[8] iodine based electrodes suffer from poor electrical conductivity.

This chapter presents the fabrication of a reduced graphene oxide (rGO)/LiI composite cathode with a gravimetric specific capacity of 200 mA h g^{-1} after 100 cycles at 0.5 C, and stable cycling performance at both low (0.5 C) and high (10 C) current densities. Promisingly, the rGO/LiI electrodes show good rate performance and a small hysteresis even at high C-rates (0.257 V at 10 C), which addresses some of the problems with the Li-iodine system, providing hope that the Li-iodine chemistry may be viable for energy storage. While LiI has been studied as an electrolyte additive or as components of a solid electrolyte,[13-16] to the best of my knowledge, this is the first report of LiI being used as an secondary lithium ion battery electrode material. The rGO was chosen as the host for LiI because of its high electrical conductivity, porous nature and good adsorptivity for both LiI and I_2.[12,17,18] Specifically, the oxygen-containing functional groups in rGO such as carbonyl and alkoxy groups, are thought to provide strong anchoring points to other elements, resulting in for example good lithium affinity.[19-21]

For example, rGO was found to serve as a shuttle inhibitor in lithium-sulfur batteries.[19] Additionally, rGO can suppress the dissolution of active materials species during cycling, and has also been found to facilitate rapid electron transfer.[12,17,18] Importantly, the use of LiI as the active cathode material rather than elemental iodine enables use of lithium-free anodes such as graphite, silicon, and tin. The high melting (469 ℃) and boiling points (1171 ℃) of LiI provide better thermostability compared to iodine (melting point : 113.7 ℃, boiling point 184 ℃), enabling heating during cell fabrication as necessary.

3.2 Results and discussion

The LiI active materials were loaded into a compressed rGO aerogel from an ethanolic LiI solution. As ethanol evaporates, LiI precipitates in the rGO. The resulting rGO/LiI composite was directly used as a free standing electrode without a current collector or additional binder. Cross-sectional SEM images of bare rGO and rGO/LiI composites are shown in Figure 3.1a and 3.1b. Cross-sectional SEM images were taken at the center of rGO film to ensure that LiI is uniformly distributed throughout rGO film. Figure 3.1a shows rGO is made up of stacks of wrinkled graphene sheets and the sheets are porous which is beneficial for both solution infiltration and ion transport. Figure 3.1b shows an SEM image of the rGO/LiI electrode. No large LiI particles were observed, perhaps because the LiI coats the rGO rather uniformally. To further confirm uniform coating of rGO with LiI, EDS mapping using high-angle annular dark-field scanning transmission electron microscopy (HAADF-STEM) was conducted (Figure 3.1c). The EDS mapping indicates that C, O and I are uniformly distributed in the rGO/LiI composite. The relatively low intensity of I might be due to the loss of I during STEM sample preparation.

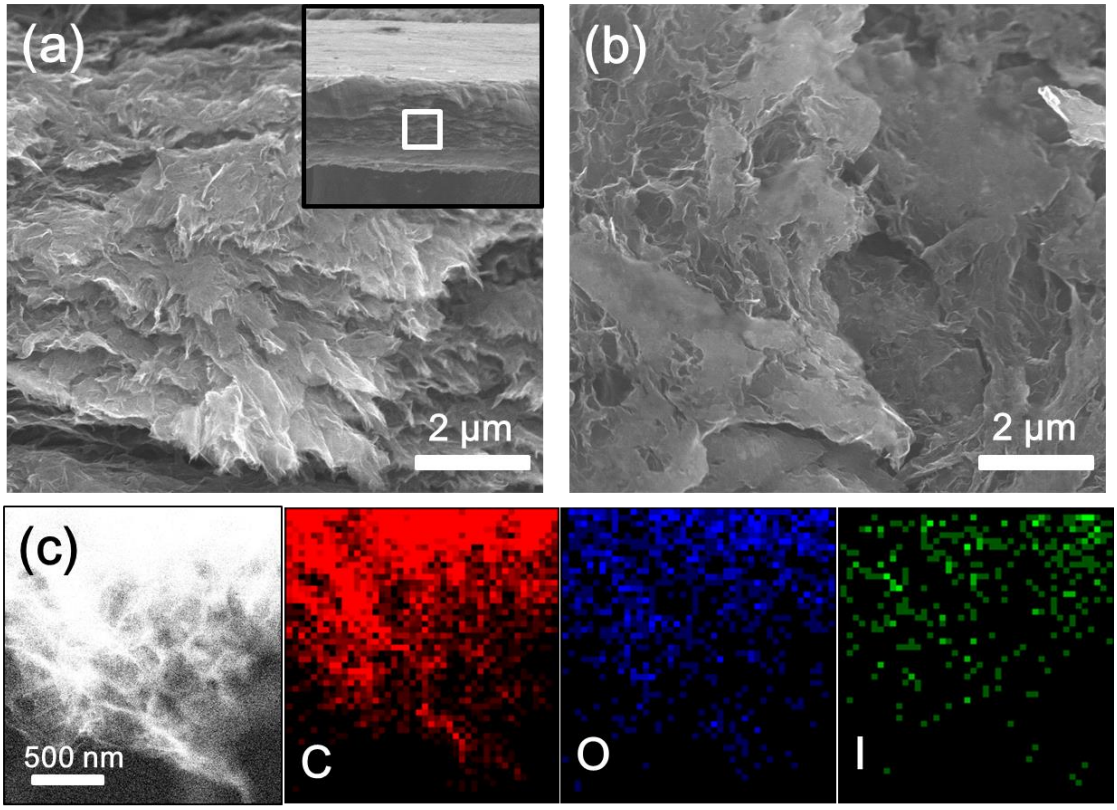

Figure 3.1 Cross-sectional SEM images of (a) Bare rGO and (b) a rGO/LiI electrode. The inset in Fig 1b is a low magnification cross-sectional SEM image of the bare rGO indicating where the high magnification image was taken (white box). (c) HAADF-STEM image of the rGO/LiI electrode and corresponding EDS mapping for C, O, and I.

XRD spectra of the rGO and rGO/LiI electrodes are shown in Figure 3.2a. The rGO exhibited a broad 002 peak at $2\theta = 23.5°$, coming from the graphene layers.[22] The rGO/LiI composite showed no diffraction peak other than two broad peaks coming from the Kapton tape (necessary to protects the LiI from oxidation), indicating the precipitated LiI is either nanocrystalline or amorphous. If a broad rGO peak is present, it may be hidden by the Kapton peaks. XPS was carried out to confirm the presence of LiI on rGO (Figure 3.2b and 3.2c) and investigate the interaction between LiI and rGO (Figure 3.3). The Li 1s peak at about 55.9 eV corresponds to Li^+.[23] The two peaks observed at 619.1 and 630.5 eV in the I 3d spectra matches the characteristic peaks of I^-.[24] No new peaks or significant peak shift were observed in the C 1s XPS spectra of rGO/LiI relative to the starting rGO, an indication that the

interaction between LiI and C is mostly physical. Interestingly, the O 1s XPS peak shifted about 1 eV toward higher energy (to about 533 eV) after LiI infilling (Figure 3.4). This is perhaps because electrons in oxygen are attracted to Li^+, leading to a higher binding energy.[25] Li_2O's O 1s peak is at 528.6 eV,[23,26] so while Li_2O can form in the process of XPS measurement, no Li_2O formation is observed in this study. The interaction between residual oxygen in the rGO and Li in the LiI perhaps improves adsorption of LiI on rGO during cycling. The oxygen content in rGO is found to be about 10 % by EDS.

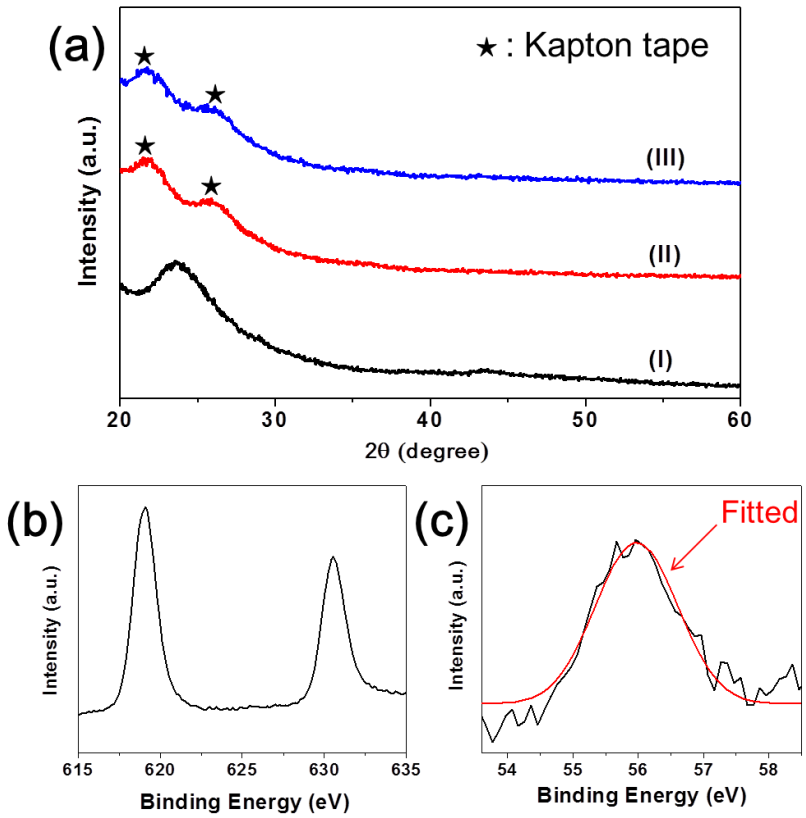

Figure 3.2 (a) XRD of (I) rGO without kapton tape, (II) rGO and (III) rGO/LiI with kapton tape. XPS spectra of (b) I 3d and (c) Li 1s from rGO/LiI.

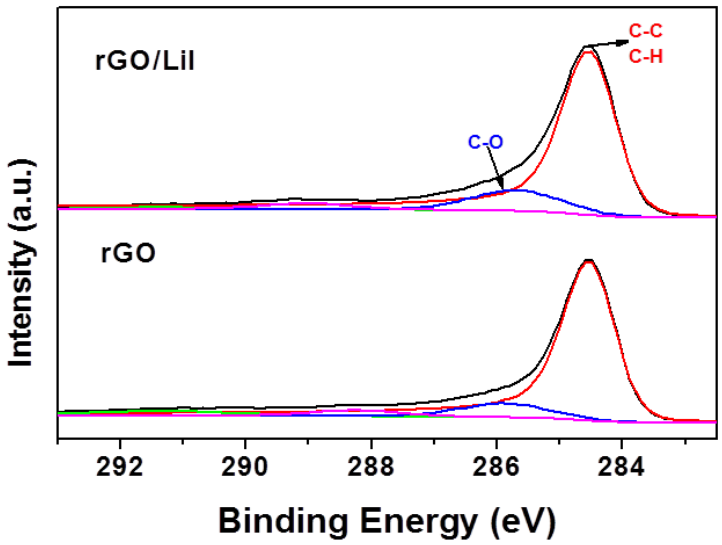

Figure 3.3 XPS spectra of C 1s region obtained from rGO and rGO/LiI sample.

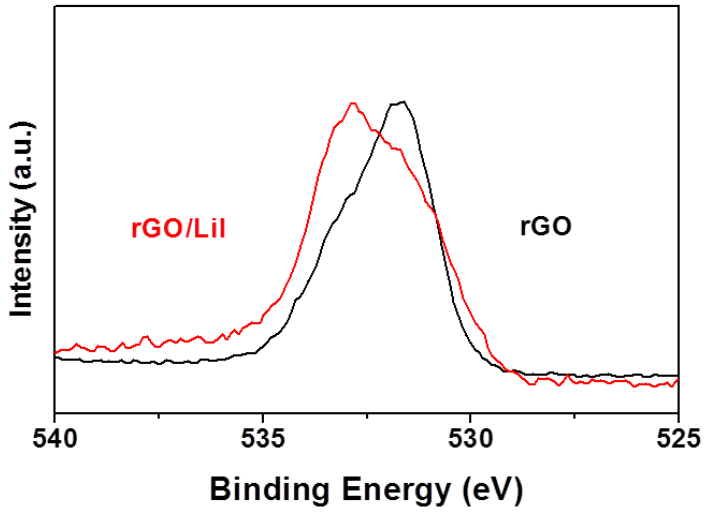

Figure 3.4 XPS spectra of O 1s from rGO and rGO/LiI.

CV was performed on the rGO/LiI composite to investigate its electrochemical properties (Figure 3.5a). In the anodic scan, LiI is oxidized to LiI_3 at 2.88 V and LiI_3 is further oxidized to I_2 at 3.5 V.[7-11] The reason why the current at the second anodic peak at 3.5 V looks saturated is because of shuttling. The reverse reaction occurs in the cathodic scan. I_2 is

reduced to LiI_3 at 3.4 V and LiI_3 is further reduced to LiI at 3.07 V. All oxidation and reduction peaks overlap well after first cycle, indicating stable and reversible electrochemical reactions. The battery reactions can be described as follows.

$$1)\ 2\mathrm{LiI} \leftrightarrow \frac{2}{3}LiI_3 + \frac{4}{3}Li^+ + \frac{4}{3}e^-$$

$$2)\ \frac{2}{3}\mathrm{Li}I_3 \leftrightarrow I_2 + \frac{2}{3}Li^+ + \frac{2}{3}e^-$$

$$\text{Overal reaction}:\ 2\mathrm{LiI} \leftrightarrow I_2 + 2Li^+ + 2e^-$$

To study the kinetics of the LiI electrodes, CV was performed at scan speeds from 0.5 to 2 mV s^{-1} (Figure 3.5b). The second anodic peaks are missing in Figure 3.5b at high scan rates. This is because the peak potential moves toward higher potentials at high scan rates unless the reaction is Nernstian in which charge transfer resistance is 0.[27] It is known that peak current has the following relationship with scan rate: $I_p = a * v^b$ where a is a constant and ν is the scan rate. b ranges from 1/2 to 1, depending on whether the reaction is diffusion controlled or a capacitive process.[28,29] Figure 3.5c shows a logarithmic relationship between peak currents and scan rate. b was determined to be 0.6 and 0.54 for the anodic and cathodic reactions, respectively, indicating the LiI_3/LiI redox pair is close to diffusion-controlled.

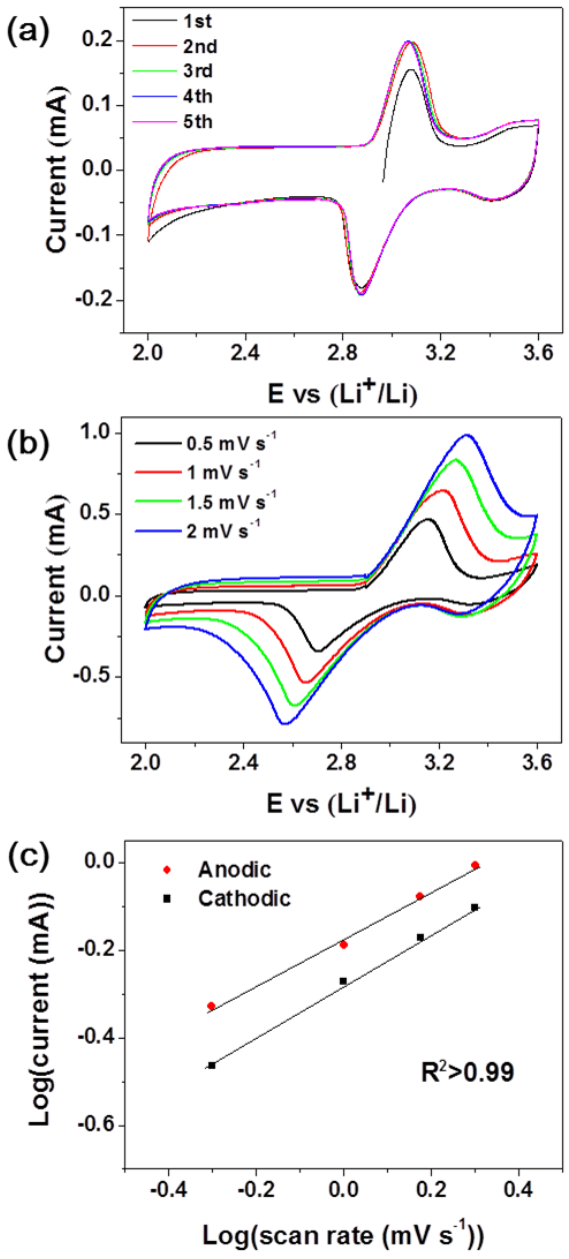

Figure 3.5 (a) Cyclic voltammetry curves of the rGO/LiI electrode at a scan rate of 0.5 mV s^{-1} and (b) scan rates of 0.5, 1, 1.5, and 2 mV s^{-1}. (c) plot of log(peak current) vs. log(scan rate) obtained from Fig 3.5b.

The formation of I_2, final product was confirmed by an ex-situ XPS measurement on a charged LiI/rGO electrode (Figure 3.6). An I $3d_{5/2}$ peak was observed at 619.9 eV which matches the characteristic peak of elemental of iodine.[30,31] The I $3d_{5/2}$ XPS peak shifted

about 0.8 eV toward higher energy after charge process (Figure 3.2b and Figure 3.6), supporting the hypothesis that LiI was converted to I_2 upon charging.

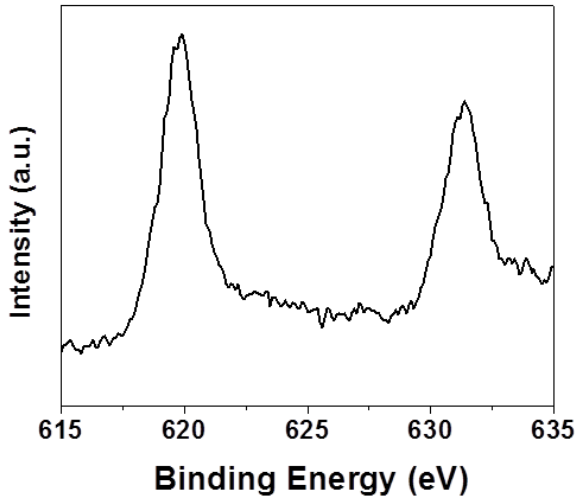

Figure 3.6 XPS spectra of I 3d from rGO/LiI electrode after first charge process.

The electrochemical properties of the rGO/LiI electrodes were evaluated by galvanostatic discharge/charge tests at room temperature. Figure 3.7a shows the performance of the rGO/LiI electrodes at 0.5 C over 100 cycles. Prior to extended cycling, the electrodes were pre-cycled 3 times at 1 C to enhance the electrode stability. The initial specific capacity of the rGO/LiI electrodes is 270 mA h g^{-1}, which is higher than theoretical capacity of LiI (200 mA h g^{-1}). This extra capacity comes from the rGO. The bare rGO capacity is about 30 mA h g^{-1} over the voltage range of 2-3.6 V (Figure 3.8), and the weight fraction of LiI in the composite is 30~40 %. Since specific capacity is calculated based on the weight of LiI only, an increase in specific capacity of 70 mA h g^{-1} from the rGO is reasonable. Charge capacity is always higher than discharge capacity because of shuttling. Figure 3.7b shows two pairs of plateaus, which are consistent with the CV profiles. The shuttling was also observed in discharge/charge curves through longer plateaus during the charge process. To reveal which redox reaction contributes more to shuttling, cycling tests were conducted at cutoff voltages of 2.0-3.3 V and 2.0-3.6 V (Figure 3.9). When the electrode was cycled in the voltage range of 2.0-3.3 V, little shuttling was observed, indicating shuttling during the LiI_3/I_2 reaction is more prominent than for LiI/LiI_3. This perhaps because I_2

is more soluble than LiI_3 in the DOL/DME electrolyte and as they will have reduced coulombic attraction with O in the rGO.

While there is shuttling at high voltages, other than this issue, the electrodes showed rather good cycling stability. The average capacity decay rate per cycle over 100 cycles is 0.28 %, and as low as 0.13 % over cycles 50 to 100. I attribute the high capacity and good cycling stability to the rGO, which both provides strong absorption of the active materials and a conductive pathway for electrons. To confirm the effect of rGO, a control experiment was performed using a CNF film rather than rGO. CNF/LiI electrodes were made using the same fabrication process and cycling was performed at 0.5 C in the voltage range of 2.0-3.6 V (Figure 3.10). The CNF/LiI electrodes exhibited low specific capacity (~40 mA h g^{-1}). Furthermore, the color of the electrolyte turned yellow after cycling, in contrast to the electrolyte for rGO/LiI, which remained clear after cycling. The electrolyte color change is due to LiI_3 and I_2 species which dissolve during cycling.[8] This result agrees with previous research which has shown that heteroatoms incorporated in graphene can offer strong binding sites for polar ionic compounds, resulting in significantly improved electrochemical performance similar to what I observe.[12,17,25,32] This also could be due to the fact that rGO has a higher surface area (active sites) than CNF. BET analysis would be required to measure the surface area.

The rate performance of the rGO/LiI electrodes was evaluated by cycling at different C-rates. The 2 C capacity was 88 % the 1 C capacity, the 5 C capacity was 77 % of the 1 C capacity, and even at 10 C, the electrode delivered 69 % of its 1 C capacity (Figure 3.7d). Moreover, when the rate returns back to 1 C, most of capacity was recovered. The reason for high-rate performance will be discussed later.

Figure 3.7e shows the cycling performance of rGO/LiI electrode at 5 C after pre-cycling at 1 C for three cycles. After 200 cycles, the discharge capacity was 168 mA h g^{-1}. Interestingly, an electrode cycled at 10 C showed even better cycling stability and at this C-rate, no significant shuttling was observed. The shuttling during the LiI_3/I_2 redox reaction was restricted at this C-rate probably because there was not sufficient time for significant amounts of active material to dissolve, travel to, and react with lithium. The difference in the specific capacities (36 mA h g^{-1}) between the samples presented in Figure 3.7c and Figure 3.7e is probably due to variations in the rGO/LiI weight ratio (60:40 for Figure 3.7c, 67:33 for Figure

3.7e) and the fact the rGO has a non-negligible capacity, and the capacity loss of the sample presented in Figure 3.7c due to it being cycled 22 times at lower C-rates before testing at 10 C, while the sample presented in Figure 3.7e had only been cycled 3 times at lower C-rates before testing at 10 C.

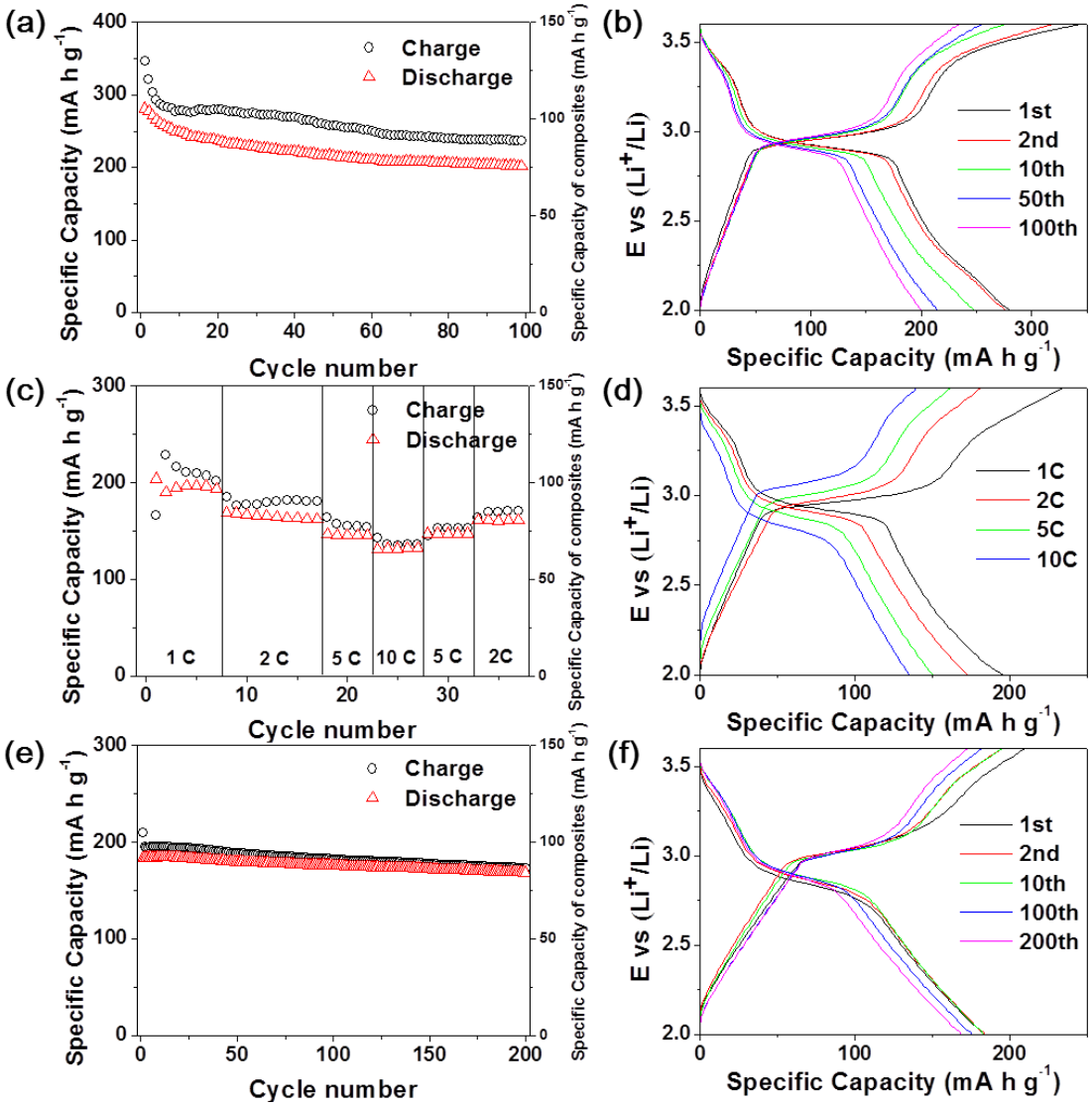

Figure 3.7 (a) Cycling performance of rGO/LiI cathode at 0.5 C. (b) 1st, 2nd, 10th, 50th and 100th cycle discharge-charge curves of rGO/LiI at 0.5 C. (c) Rate performance of LiI at 1 to 10 C. (d) Second cycle rGO/LiI discharge/charge curves at different C-rates. (e) Cycling performance of rGO/LiI at 10 C. (f) 1st, 2nd, 10th, 100th and 200th cycle rGO/LiI discharge/charge curves at 0.5 C.

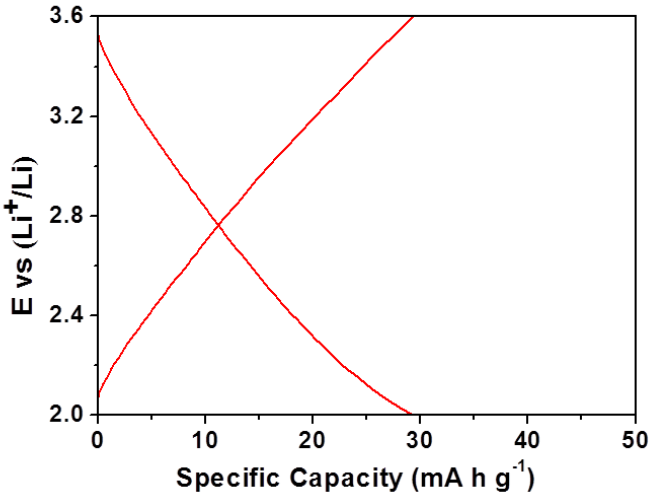

Figure 3.8 Typical discharge and charge curves of bare rGO. As a result of the rGO capacity, there was a maximum of a 15 % LiI-based specific capacity error due to the somewhat indeterminate capacity of rGO in the rGO/LiI electrodes.

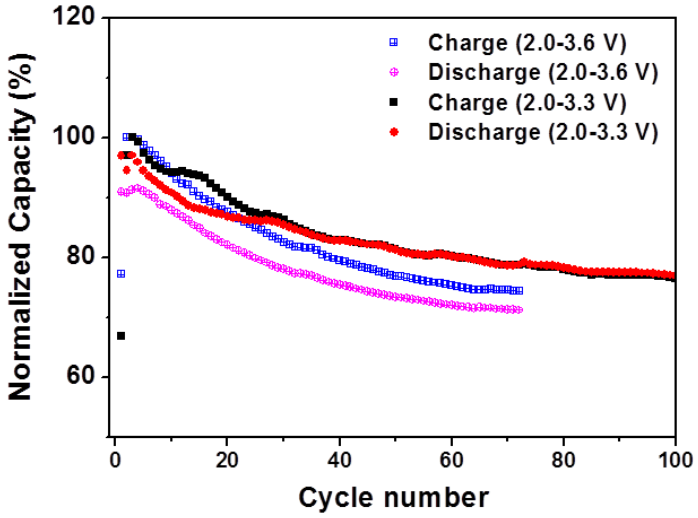

Figure 3.9 Normalized Capacity behavior of LiI/rGO electrodes cycled at 1 C over the voltage ranges of 2.0-3.6 V and 2.0-3.3 V.

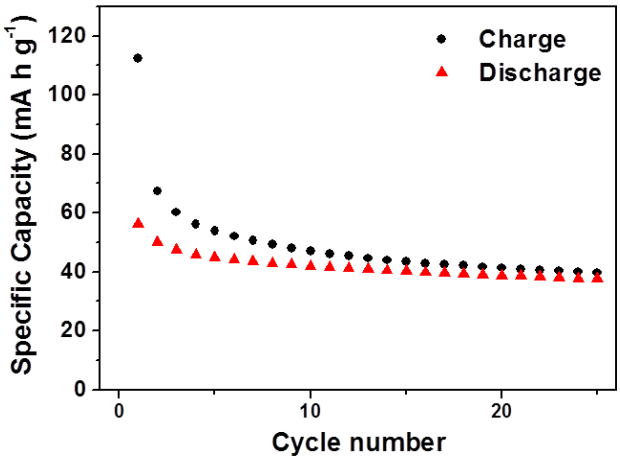

Figure 3.10 Cycling performance of CNF/LiI composite at 0.5 C.

Importantly, there are few changes in the voltage plateaus (Figure 3.7b) with increasing C-rate. The voltage hysteresis at 1, 2, 5 and 10 C was determined from dQ/dV curves (Figure 3.11a) obtained by differentiating the charge/discharge voltage curves of the second cycle at each C-rate. Two pairs of redox peaks observed in cyclic voltammetry were also seen in the dQ/dV curves. The hysteresis was taken as the difference between the LiI_3/LiI redox peaks. Figure 3.11b presents the calculated hysteresis, 0.056, 0.081, 0.158, 0.257 V, at 1, 2, 5 and 10 C, respectively. These values are the smallest I am aware of for alloying or conversion reactions (a similar trend is observed for the I_2/LiI_3 redox couple, where the hysteresis is 0.047, 0.117, 0.108, and 0.277 V at 1,2,5 and 10 C, respectively). Hysteresis is as sum of polarization in charge and discharge process. The primary contributions to polarization are (1) activation polarization related to charge transfer reactions, (2) ohmic polarization coming from internal resistances of cell components and the contact resistance between cell components, and (3) concentration polarization coming from limitations in diffusion.[33] Figure 3.5c shows the reaction kinetics of the LiI_3/LiI redox pair is mostly limited by diffusion rather than charge transfer indicating concentration polarization is more important than activation polarization. The ohmic polarization has a linear relationship with current ($\eta = IR$), while concentration polarization is logarithmic in terms of current ($\eta = c * \log\left(\frac{I_l}{I_l - I}\right)$, c is constant). Since hysteresis was linear with current (C-rate), it appears the (small) hysteresis is mostly

dominated by ohmic polarization. When concentration polarization is dominant, hysteresis will not be linear with current, and the point where the hysteresis becomes non-linear with current is dependent on the limiting current (I_l), the current where the Li concentration gradient becomes steep within the active materials. As shown in the above equation, the higher the limiting current, the smaller the concentration polarization. The limiting current is defined as follows. $I_l = \frac{nFAD_0C_0^*}{\delta}$ (D_0: diffusion coefficient, C_0^*: concentration of Li at the electrode surface, δ: diffusion length). The limiting current of the rGO/LiI electrode is expected to be high because of short solid-state diffusion lengths (LiI particle thickness) and high Li diffusion coefficient in LiI.[34,35] The fact that the activation polarization and concentration polarization is not changing significantly with current density is a sign that charge transfer and mass transfer effects are not limiting the rate performance, resulting in the high-rate performance.

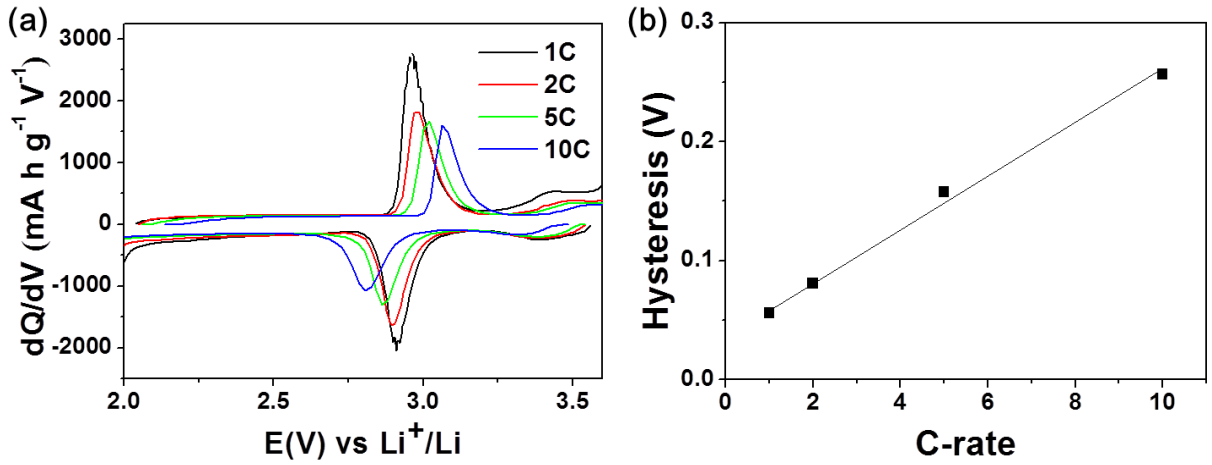

Figure 3.11 (a) Differential capacity plot of the second cycle at 1, 2, 5, and 10 C. (b) Plot of C-rate vs. hysteresis (V) based on Fig 3.11a.

To examine the cause of capacity fade of the rGO/LiI electrodes, impedance measurements were conducted after 10, 20 and 30 cycles (Figure 3.12). The resulting three Nyquist plots consist of two depressed semicircles in the high and medium frequency regions and an inclined line indicating solid-state Li diffusion in the low frequency regions. The charge transfer resistance is shown by the diameters of the two semicircles. The presence of two

semicircles in the Nyquist plot is presumably due to dissolved redox species.[36] Marcus theory suggests charge transfer reaction rates are affected by environment.[27] Charge transfer reactions of dissolved redox species should be fast because structural reorganization in the electrolyte is easier.[27,36] Therefore, the high frequency semicircle may represent electrochemical redox reactions of dissolved species and the medium frequency semicircle related to redox reactions on the solid electrode. One concern is that $LiNO_3$ has been reported to react with lithium to form a protective surface film.[37] To ensure this film has no impact on the impedance measurements, they were repeated immediately after replacing the Li metal anode with a new one. The same two semicircles were still observed. Considering the $LiNO_3$-derived film is not formed before cycling,[38] this result validates the two semicircles are not related to the Li anode.

All Nyquist plots showed significantly overlapped shapes and similar charge transfer resistances (Figure 3.12 and Table 3.1), indicating the electrode reaction kinetics remained largely unchanged during cycling.

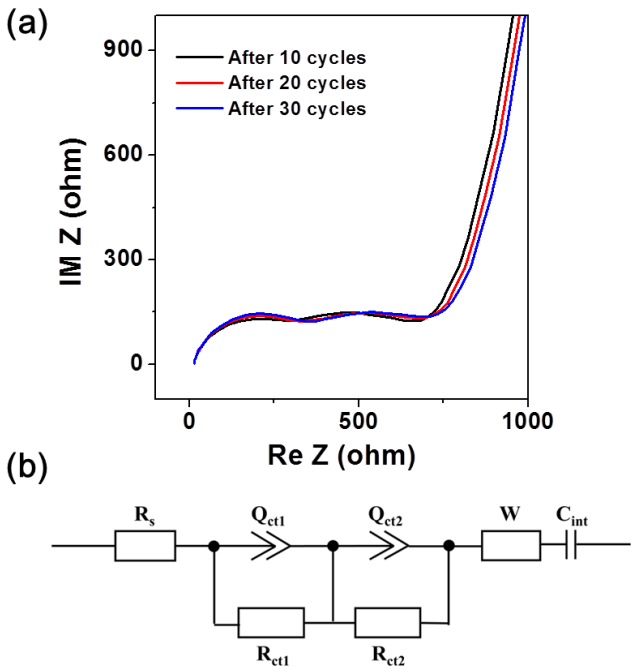

Figure 3.12 (a) Electrochemical impedance spectroscopy of rGO/LiI electrodes after 10, 20 and 30 cycles (b) Equivalent circuit model used for impedance data fitting. (R_s: solution resistance; R_{ct1} and R_{ct2}: charge transfer resistance; Q_{ct1} Q_{ct2} : constant phase element; W: Warburg impedance; C_{int}: intercalation capacitance).

	R_s (Ω)	R_{ct1} (Ω)	R_{ct2} (Ω)
after 10 cycles	12.74	382.9	242
after 20 cycles	12.76	376.3	278.9
after 30 cycles	12.27	376.1	301.5

Table 3.1 Fitting data from Figure 3.12a.

For further insight into the capacity fade, SEM analysis was conducted on the Li metal anode after cycling. After cycling 30 times, the Li metal anode was removed from the electrolyte and dried in a glove box without washing. Figure 3.13a shows the SEM image of

the anode after cycling. Small particles were observed on the anode. In lithium-sulfur batteries, the dissolved polysulfides can migrate throughout the separator by shuttling to form insoluble sulfides (Li_2S_2, Li_2S) onto Li surface. The gradual growth of this inactive layer contributes to the capacity decay by consuming active materials.[39-41] A similar phenomenon was observed here. EDS (Figure 3.13b) indicates these particles contain O, S and I, indicating iodine species were consumed by shuttling and forming compounds on the Li surface, providing the possibility the capacity decay with cycling is due to loss of active materials. As a control experiment, an uncycled Li metal anode was treated similarly, and no particles were observed on the anode, indicating the particles form during cycling. The LiI morphology after cycling (10 cycles, 0.5 C) is not clear, similar to the previously reported unclear morphology of a rGO/Li_2S electrode after cycling. The EDS spectrum and iodine mapping indicate LiI is present on the rGO. Electrolyte (F, O, and S peaks) were also observed in the EDS spectrum as the electrode was not washed before EDS analysis, because of high solubility of LiI in organic electrolyte.

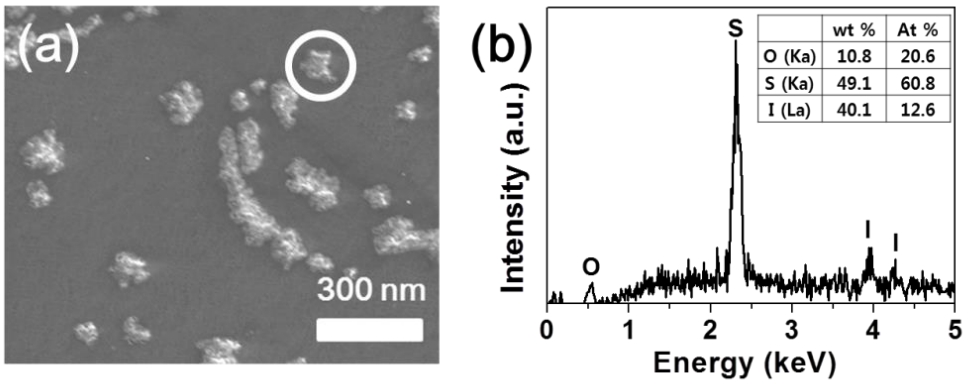

Figure 3.13 (a) SEM image of a Li electrode after cycling and (b) EDS spectrum taken from marked region in Figure 3.13a.

3.3 Conclusions

In conclusion, rGO/LiI electrodes prepared by a simple solution infiltration, evaporation and precipitation method were demonstrated as a lithium ion battery cathode for the first time. The rGO/LiI cathode shows a reasonable specific capacity and stable cycling behavior at both

low and high current densities probably because rGO provides an efficient electron pathway and suppresses the dissolution of active materials during cycling. The rGO/LiI electrode exhibits good rate performance and small hysteresis at high C-rate, which can be attributed to its fast reaction kinetics resulting from the short electron and ion diffusion lengths in this system. While I have yet to do the experiments, I suspect the performance of rGO/LiI electrodes can be increased further by engineering the rGO oxygen content or by doping other element into the rGO and by electrolyte optimization. This work demonstrates the possibility of using LiI as a battery cathode and may inspire further investigations on LiI-based cathodes.

	$LiCoO_2$	$LiMn_2O_4$	$LiFePO_4$	LiI
Density (g cm^{-3})	5.1	4.3	3.6	4.1
Potential (V)	3.9	4.05	3.4	2.95
Specific capacity (mA h g^{-1})	140	120	160	200
Specific energy vs. Li (Wh kg^{-1})	546	486	544	590
Volumetric capacity (mA h cm^{-3})	714	516	576	820
Energy density (Wh L^{-1})	2785	2090	1958	2419

Table 3.2 Electrochemical characteristics of some commercial Li-ion battery cathode materials and LiI.[1-3]

3.4 Experimental section

Synthesis of rGO aerogel: GO was synthesized by a modified Hummer's method using expanded graphite.[42] The rGO aerogel was synthesized as reported.[43] GO (4 mg/mL) was dispersed into an aqueous solution which has the weight ratio of GO:Hypophosphorous acid (H_3PO_2):I_2 of 1:100:10. The final volume was 40 mL. The solution was sonicated for 5 min and then put into a water-bath maintained at 90℃. A black gel-like cylinder was removed after 12h

and washed with alcohol and water in a soxhlet extractor for 12h. The wet gels were freeze-dried for two days to obtain the aerogel.

Synthesis of rGO/Li composite: A 0.1 M LiI solution was prepared by dissolving lithium iodide (LiI, Sigma Aldrich) in anhydrous ethanol with stirring overnight in an argon-filled glove box. The rGO aerogels were pressed and cut into about 40 µm-thick pieces and dried at 100 ℃ under vacuum. The resulting rGO electrodes were then transferred into the glove box. Since LiI is air and moisture sensitive, the remaining steps were all done in a glove box. LiI solution was dropped onto the rGO electrodes using a pipette and the ethanol fully evaporated. The rGO electrodes were then turned over and the LiI-infilling step repeated. The whole process was repeated two additional times. The rGO/LiI composite materials were then heated at 150 ℃ for 1h. The areal capacity was around 0.4 mA h cm^{-2}. The areal capacity can be further increased by pressing multiple electrodes together (Figure 3.14).

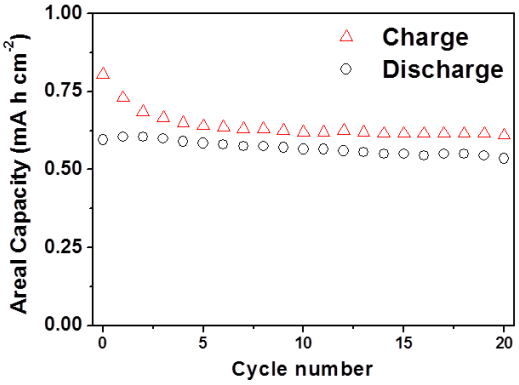

Figure 3.14 0.5 C areal capacity of electrode formed by pressing two rGO/LiI electrodes together.

Characterization: Electrode morphologies were confirmed using a Hitachi S-4700 SEM. EDS was conducted using a Hitachi S-4700 SEM equipped with an Oxford INCA energy-dispersive X-ray analyzer. XPS analysis were done with a Kratos Axis Ultra XPS system with a monochromatic Al Kα (1486.6 eV) source. Binding energies were calibrated with respect to the C 1s peak (284.4 eV). To minimize air exposure time, samples for SEM and XPS measurement were prepared in the glove box. The sample was attached on the sample holder which was put in a bottle filled with Ar gas and tightly sealed. The sample holder was taken out of the bottle just before transferring to the vacuum chamber. The vacuum chamber was immediately pumped

down. The air exposure time was less than 1 second. The crystal structures were checked by a Philips X'pert MRD XRD (Materials Research Diffractometer) using Cu Kα radiation (λ = 0.15418 nm). The rGO/LiI sample was sealed in the glove box using Kapton tape to prevent oxidation of LiI. STEM-EDS was performed using JEOL 2200FS with a HAADF detector for elemental mapping.

Electrochemical Measurements: 1.0 M Lithium bis(trifluoromethane sulfonyl) imide (LiTFSI) in 1,3-dioxolane (DOL) /1,2-dimethoxyethane (DME) (1:1 by vol) containing 1 wt % $LiNO_3$ was used as electrolyte and lithium foil was used as the counter electrode for two-electrode cells. All cells were assembled in the glove box. Galvanostatic discharge/charge tests and cyclic voltammetry were conducted using a VMP3, Bio-Logic potentiostat and swagelok-type cells over a voltage range of 2.0 to 3.6 V or 2.0 to 3.3 V vs. Li/Li^+. Current densities and specific capacities were calculated based on LiI. An AC amplitude of 6 mV was applied over the frequency range of 100 kHz to 10 mHz for impedance measurements.

3.5 References

[1] M. Armand, J.-M. Tarascon, *Nature* **2008**, *451*, 652.

[2] S. W. Lee, N. Yabuuchi, B. M. Gallant, S. Chen, B.-S. Kim, P. T. Hammond, Y. Shao-Horn, *Nature Nanotechnol.* **2010,** *5*, 531.

[3] V. Etacheri, R. Marom, R. Elazari, G. Salitra, D. Aurbach, *Energy Environ. Sci.* **2011,** *4*, 3243.

[4] W. K. Behl, D. T. Chin, *J. Electrochem. Soc.* **1988,** *135*, 16.

[5] G. Boschloo, A. Hagfeldt, *Acc. Chem. Res.* **2009,** *42*, 1819.

[6] X. Dong, L. Chen, J. Liu, S. Haller, Y. Wang, Y. Xia, *Sci. Adv.* **2016,** *2*, e1501038.

[7] Y. Wang, Q. Sun, Q. Zhao, J. Cao, S. Ye, *Energy Environ. Sci.* **2011**, *4*, 3947.

[8] Q. Zhao, Y. Lu, Z. Zhu, Z. Tao, J. Chen, *Nano Lett.* **2015**, *15*, 5982.

[9] K. Li, B. Lin, Q. Li, H. Wang, S. Zhang, C. Deng, *ACS Appl. Mater. Interfaces* **2017**, *9*, 20508.

[10] H. Wang, G. Zhang, L. Ke, B. Liu, S. Zhang, C. Deng, *Nanoscale* **2017**, *9*, 9365.

[11] Q. Zhang, Z. Wu, F. Liu, S. Liu, J. Liu, Y. Wang, T. Yan, *J. Mater. Chem. A* **2017,** *5*, 15235.

[12] G. Zhou, E. Paek, G. S. Hwang, A. Manthiram, *Adv. Energy Mater.* **2016,** *6*, 1501355.

[13] F.-C. Liu, W.-M. Liu, M.-H. Zhan, Z.-W. Fu, H. Li, *Energy Environ. Sci* **2011,** *4*, 1261.

[14] K. H. Park, D. Y. Oh, Y. E. Choi, Y. J. Nam, L. Han, J. Y. Kim, H. Xin, F. Lin, S. M. Oh, Y. S. Jung, *Adv. Mater.* **2016**, *28*, 1874.

[15] S. H. Park, H. J. Kim, J. Jeon, Y. Choi, J. J. Cho, H. Lee, *ChemElectroChem* **2016,** *3*, 1915.

[16] F. Wu, J. T. Lee, N. Nitta, H. Kim, O. Borodin, G. Yushin, *Adv. Mater.* **2015,** *27*, 101.

[17] L. Ji, M. Rao, H. Zheng, L. Zhang, Y. Li, W. Duan, J. Guo, E. J. Cairns, Y. Zhang, *J Am. Chem. Soc.* **2011,** *133*, 18522.

[18] C. Wang, X. Wang, Y. Yang, A. Kushima, J. Chen, Y. Huang, J. Li, *Nano Lett.* **2015,** *15*, 1796.

[19] X. Wang, Z. Wang, L. Chen, *J. Power Sources* **2013**, *242*, 65.

[20] X. Hu, Z. Li, Y. Zhao, J. Sun, Q. Zhao, J. Wang, Z. Tao, J. Chen, *Sci. Adv.* **2017,** *3*, e1602396.

[21] D. Lin, Y. Liu, Z. Liang, H.-W. Lee, J. Sun, H. Wang, K. Yan, J. Xie, Y. Cui, *Nature Nanotechnol.* **2016,** *11*, 626.

[22] L. Stobinski, B. Lesiak, A. Malolepszy, M. Mazurkiewicz, B. Mierzwa, J. Zemek, P. Jiricek, I. Bieloshapka, *J. Electron Spectrosc. Relat. Phenom.* **2014,** *195*, 145.

[23] S. Tanaka, M. Taniguchi, H. Tanigawa, *J. Nucl. Mater.* **2000,** *283*, 1405.

[24] C. Strydom, J. Van Staden, H. Strydom, *Electroanalysis* **1991**, *3*, 197.

[25] C.-P. Yang, Y.-X. Yin, H. Ye, K.-C. Jiang, J. Zhang, Y.-G. Guo, *ACS Appl. Mater. Interfaces* **2014,** *6*, 8789.

[26] K. P. Yao, D. G. Kwabi, R. A. Quinlan, A. N. Mansour, A. Grimaud, Y.-L. Lee, Y.-C. Lu, Y. Shao-Horn, *J. Electrochem. Soc.* **2013,** *160*, A824.

[27] A. J. Bard, L. R. Faulkner, J. Leddy, C. G. Zoski, *Electrochemical Methods: Fundamentals and Applications*, 2nd ed.; Wiley, **2001**.

[28] V. Augustyn, J. Come, M. A. Lowe, J. W. Kim, P.-L. Taberna, S. H. Tolbert, H. D. Abruña, P. Simon, B. Dunn, *Nat. Mater.* **2013**, *12*, 518.

[29] T. Brezesinski, J. Wang, S. H. Tolbert, B. Dunn, *Nat. Mater.* **2010**, *9*, 146.

[30] D. Gong, B. Wang, J. Zhu, R. Podila, A. M. Rao, X. Yu, Z. Xu, B. Lu, *Adv. Energy Mater.* **2017**, *7*, 1601885.

[31] H. Tian, T. Gao, X. Li, X. Wang, C. Luo, X. Fan, C. Yang, L. Suo, Z. Ma, W. Han, *Nat. Commun.* **2017,** *8*, 14083.

[32] H. J. Peng, T. Z. Hou, Q. Zhang, J. Q. Huang, X. B. Cheng, M. Q. Guo, Z. Yuan, L. Y. He, F. Wei, *Adv. Mater. Interfaces* **2014**, *1*, 1400227.

[33] M. Winter, R. J. Brodd, *Chem. Rev.* **2004,** *104*, 4245.

[34] F.-C. Liu, Z. Shadike, X.-F. Wang, S.-Q. Shi, Y.-N. Zhou, G.-Y. Chen, X.-Q. Yang, L.-H. Weng, J.-T. Zhao, Z.-W. Fu, *Inorg. Chem.* **2016,** *55*, 6504.

[35] Z. Cao, Z. Liu, J. Sun, F. Huang, J. Yang, Y. Wang, *Solid State Ionics* **2008,** *179*, 1776.

[36] Y. Yang, G. Zheng, S. Misra, J. Nelson, M. F. Toney, Y. Cui, *J Am. Chem. Soc.* **2012,** *134*, 15387.

[37] D. Aurbach, E. Pollak, R. Elazari, G. Salitra, C. S. Kelley, J. Affinito, *J. Electrochem. Soc.* **2009,** *156*, A694.

[38] X. Liang, Z. Wen, Y. Liu, M. Wu, J. Jin, H. Zhang, X. Wu, *J. Power Sources* **2011,** *196*, 9839.

[39] S. Evers, L. F. Nazar, *Acc. Chem. Res.* **2012,** *46*, 1135.

[40] X. Ji, L. F. Nazar, *J. Mater. Chem.* **2010,** *20*, 9821.

[41] A. Manthiram, Y. Fu, Y.-S. Su, *Acc. Chem. Res.* **2012,** *46*, 1125.

[42] V. H. Pham, T. V. Cuong, T.-D. Nguyen-Phan, H. D. Pham, E. J. Kim, S. H. Hur, E. W. Shin, S. Kim, J. S. Chung, *Chem. Commun.* **2010,** *46*, 4375.

[43] H. D. Pham, V. H. Pham, T. V. Cuong, T.-D. Nguyen-Phan, J. S. Chung, E. W. Shin, S. Kim, *Chem. Commun.* **2011,** *47*, 9672.

CHAPTER 4
CARBON NANOTUBE/SODIUM IODIDE COMPOSITE CATHODES FOR SODIUM ION BATTERIES

The content of this chapter was previously published in: "High Energy Density CNT/NaI Composite Cathodes for Sodium-Ion Batteries", Sanghyeon Kim, Xiangming Li, Lingzi Sang, Ralph G. Nuzzo, Andrew A. Gewirth, and Paul V. Braun, Advanced Materials Interfaces, 5, 1801342, 2018.

4.1 Introduction

Extensive research has been carried out on rechargeable batteries for applications ranging from portable electronics to grid-scale storage.[1-3] While LIBs are the dominant energy storage system for portable devices, large-scale application of LIBs may be limited by the cost and scarcity of lithium,[4,5] which has led to an increase in interest in SIBs.[4-6] However, commercialization of SIBs has been hampered due to issues including the low energy density and poor cyclability of current cathode materials.[7-9] Discovery of stable and high energy density sodium ion cathode materials would be one step towards improving the commercialization prospects for SIBs.

The Li-iodine system (I_2 + 2Li ↔ 2LiI) has been studied for LIBs because of fast conversion of the iodine/triiodide redox pair and high reaction voltage with lithium.[10-17] Initial evidence suggests the Na-iodine system can also be used for SIBs analogously. Although there are two recent reports on the use of I_2 for SIBs, the electrode working potentials (around 2.5 V based on second plateau) are significantly lower than the expected thermodynamic value of 2.96 V (calculations in supporting information) and the electrodes shows large voltage hystereses.[13,18] These reports have focused on the Na-iodine system (I_2 + 2Na ↔ 2NaI) using iodine as starting cathode, however, I suggest starting with NaI would be more desirable than I_2 if NaI can be induced to reversibly react with sodium. Use of NaI will allow the use of sodium-free anodes such as antimony, tin, hard carbon, and phosphorous.[19-22] Also, NaI (melting point: 661 ℃, boiling point: 1,304 ℃) is much more thermostable than iodine which is volatile in room temperature (melting point: 113.7 ℃, boiling point: 184 ℃), thus allowing heating during electrode fabrication.

In this chapter, the fabrication of a freestanding NaI-loaded CNT mat (CNT/NaI) electrode is presented and its potential as a SIBs cathode is demonstrated. To the best of my knowledge, this is the first report of NaI being used as a secondary SIBs cathode. While initial designs did not cycle well, once a CNT mat interlayer was inserted between the cathode and the separator and FEC was added to the electrolyte, the resulting electrode showed stable cycling performance with a gravimetric specific capacity of 156 mA h g^{-1} after 100 cycles at 100 mA g^{-1}. Importantly, the CNT/NaI electrodes exhibited a reaction potential close to the thermodynamic value and a small hysteresis.

4.2 Results and discussion

CNT/NaI electrodes were prepared by a simple solution infiltration, evaporation and precipitation method (Figure 4.1a). A CNT mat was chosen as the host for NaI because of its high electrical conductivity and its porous structure which enabled both solution infiltration and facilitated ion transport in the resulting composite.[23,24] NaI was loaded into a CNT film using a 0.44 M ethanolic NaI solution; NaI precipitates in the CNT film as ethanol evaporates. The CNT/NaI composite was directly used as a free standing electrode without additional binder and with the CNT mat serving as the current collector. Before cell assembly, the same thickness CNT mat (40~50 μm) was inserted between the CNT/NaI cathode and separator. This interlayer serves to capture soluble redox species produced during the cycling and suppress shuttling, improving the utilization of active materials and enhancing cyclability.[23,25-27]

Figure 4.1b shows XRD spectra of the as synthesized CNT mat and CNT/NaI cathode. The cathode was covered with Kapton tape to protect NaI from oxidation. XRD of the CNTs shows three characteristic graphitic diffraction peaks at 26.1°, 44.5° and 53.4° which can be indexed as (002), (100), and (004) reflections, respectively.[28,29] No NaI diffraction peak was found after NaI loading, indicating the NaI is either nanocrystalline or amorphous. A SEM image of the CNT/NaI cathode is shown in Figure 4.1c. The morphology is quite similar to that of the bare CNT film (Figure 4.2) indicating NaI is not present as large particles. XPS confirmed the presence of NaI (Figure 4.1d and 4.1e). A Na 1s peak at 1071.5 eV corresponding to the characteristic peak of Na^+, and two peaks at 618.7 and 630.2 eV in the I 3d spectra matching the characteristic peaks of I^- are observed.[30-32] To further confirm the presence of NaI on the

CNT, EDS mapping was performed (Figure 4.1f), which shows Na and I are uniformly distributed across the CNT/NaI cathode.

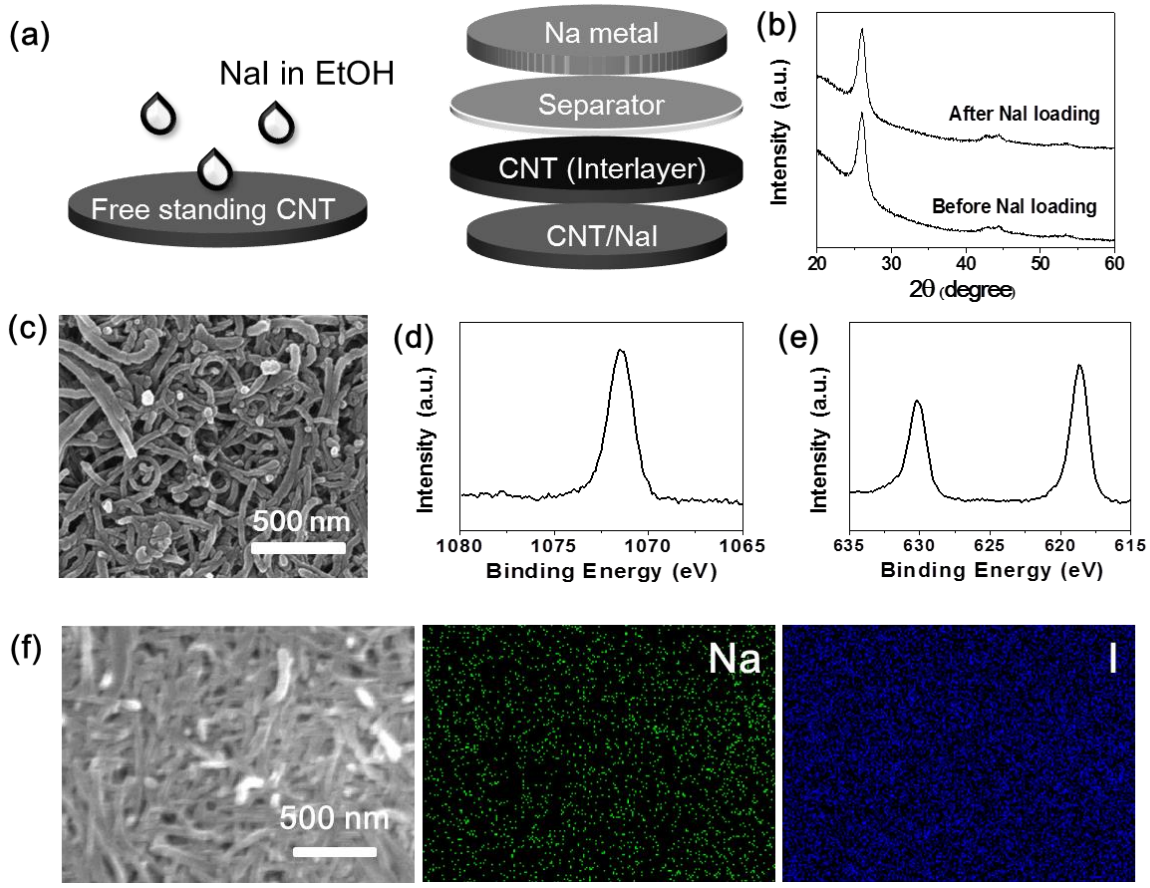

Figure 4.1 (a) Schematic description of a freestanding CNT/NaI electrode fabrication and the cell configuration. (b) XRD of CNT before and after NaI loading with kapton tape. (c) SEM image of a CNT/NaI electrode. XPS spectra of (d) and (e) I 3d from CNT/NaI. (f) SEM image of a CNT/NaI electrode and corresponding Na and I EDS mapping.

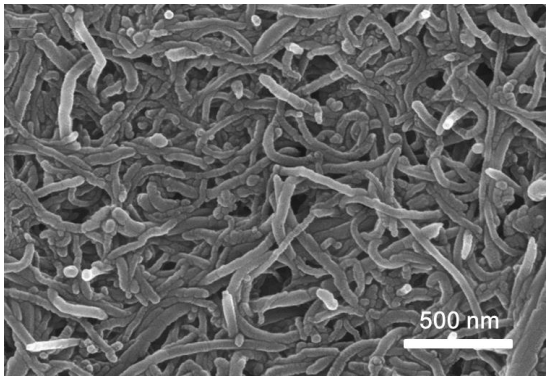

Figure 4.2 SEM image of a bare CNT mat.

We optimized the electrolyte to improve the electrochemical performance of the CNT/NaI cathodes. First, the salt concentration was increased from 1 M to 1.5 M. According to previous studies, higher electrolyte molarity improves capacity utilization significantly and reduces active material dissolution.[33,34] Salt concentrations higher than 1.5 M were not tried as 1.5 M is approximately the solubility limit of $NaClO_4$ in the electrolyte. Second, FEC was added to the electrolyte to minimize shuttling. A CNT/NaI electrode including a CNT interlayer cycled in the FEC-free electrolyte exhibited infinite charging (Figure 4.3), presumably because the dissolved active materials traveled to the sodium, reacted with it and returned to the cathode side. Once FEC was added, shuttling was suppressed. FEC is known to form a protective barrier on both the anode and cathode during cycling which might help reduce the dissolution of active materials.[35-38]

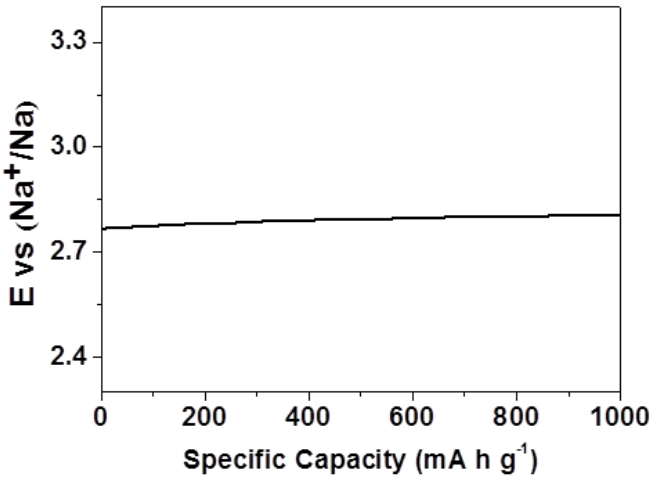

Figure 4.3 Charge curve of a CNT/NaI electrode with interlayer cycled at 100 mA g-1 using electrolyte without added FEC. Charging continues at a constant voltage because of shuttling.

Figure 4.4a shows the long term cycling performance of the CNT/NaI cathode at 100 mA g^{-1} (c-rate of 0.56 C) over 100 cycles. To evaluate the effect of the interlayer, a CNT/NaI electrode was tested under the same conditions with and without the interlayer. The CNT/NaI electrode with the interlayer exhibited a first discharge capacity of 170 mA h g^{-1} which is 95.1 % of the NaI theoretical capacity, indicating high active material utilization. After 100 cycles the specific capacity was 156 mA h g^{-1} and the electrode was stable to cycling. When the interlayer was not present, the electrode capacity decayed rapidly and dropped to below 60 mA h g^{-1} after 20 cycles.

Shuttling was also significantly greater when no interlayer was used as reflected by the coulombic efficiency of two electrodes. The coulombic efficiency of the electrode with an interlayer gradually increases to about 99 % while the coulombic efficiency of the interlayer free electrode starts to decrease after 35 cycles and drops to 80 %. Shuttling of the interlayer free electrode is also shown in discharge/charge curves (Figure 4.5) by longer plateaus during the charge process.

I observe that the interlayer captures dissolved species, preventing them from crossing over to the anode. Figure 4.6 shows iodine is distributed throughout the interlayer after cycling. For all experiments here, specific capacities are on a NaI weight basis and the weight fraction of NaI in the freestanding electrode is 25~30 %. The variation in the weight fraction of NaI

(25~30 %) is due to the weight variation of the CNT mat as the same amount of NaI always was loaded on the CNT. The capacity contribution of the CNT mat is not included, as the bare CNT showed a specific capacity of less than 1.2 mA h g^{-1} over the voltage range of 2.3-3.4 V (Figure 4.7).

The discharge-charge curves of a CNT/NaI electrode shows two pairs of plateaus (Figure 4.4b), indicating the electrochemical reaction consists of two steps. During charging, NaI is oxidized to NaI_3 at 2.83 V and NaI_3 is further oxidized to I_2 at 3.29 V.[13,18] During discharging, I_2 is reduced to NaI_3 at 3.22 V and NaI_3 is further reduced to NaI at 2.8 V.[13,18] These reactions can be most clearly seen in dQdV curves (Figure 4.4e). Figure 4.4e shows corresponding redox peak pairs. Both discharge plateaus appeared above 2.8 V after the first cycle, making the second discharge specific energy density as high as 473 W h kg^{-1} (vs. sodium metal). Hysteresis was taken as the voltage difference between the redox peaks. The very small hysteresis (0.03 V) between the charging and discharging NaI_3/NaI redox peaks and the average working potential of 2.83 V, which is close to the thermodynamic value of 2.96 V (calculations in supporting information), are particularly promising as they indicate the electrode is operating close to its thermodynamic limits.

Calculations

The theoretical electromotive force of the NaI electrode can be calculated as follows (data from Lange's Handbook of Chemistry, 15th Ed., McGraw-Hill, Inc.).

$$\mathrm{NaI} \leftrightarrow \mathrm{Na} + \frac{1}{2} I_2$$

$$\Delta G_f = \Delta G_{NaI} - \Delta G_{Na} - \frac{1}{2}\Delta G_{I_2} = -\frac{286\ \mathrm{kJ}}{\mathrm{mol}} - 0 - 0 = -286\ \mathrm{kJ}\, mol^{-1}$$

$$\mathrm{E} = -\frac{\Delta G_f}{nF} = \frac{\frac{286\ kJ}{mol}}{\frac{96485\ C}{mol}} = 2.96\ \mathrm{V}$$

The theoretical specific capacity of the NaI electrode can be calculated as follows.

$$\mathrm{C} = \frac{nF}{m} = \frac{96485\ C/mol}{149.89\ g/mol} \cdot \frac{mA \cdot h}{3600} = 178.8\ mA\ h\ g^{-1}$$

This small hysteresis is probably due to its fast kinetics by nature [10-17] and the fact that the reaction kinetics is not limited by externally owing to high electrical conductivity of CNT and very small size of active materials coated on CNT. To study the reaction kinetics of the CNT/NaI electrodes, cyclic voltammetry was conducted at scan rates from 0.3 to 1.5 mV s^{-1} (Figure 4.8a). The second anodic peaks are indistinguishable at high scan rates because at these scan rates, the first and second anodic peaks overlapped. The peak current has the following relationship with scan rate: $I_p = a * v^b$ where a is a constant and ν is the scan rate. b ranges from

0.5 to 1, depending on whether the reaction is diffusion controlled or a capacitive process.[39,40] Figure 4.8b exhibits a logarithmic relationship between NaI_3/NaI redox peak currents and scan rate. b was determined to be 0.6 and 0.5 for the anodic and cathodic reactions, respectively, indicating the NaI_3/NaI redox pair is primarily diffusion controlled.

The rate performance of the CNT/NaI electrodes (including the CNT interlayer mat) was evaluated by cycling at different current densities. Specific capacities of 165, 145, 102, 79, 63 mA h g^{-1} were obtained at 100, 200, 500, 1000, 2000 mA g^{-1} (0.56, 1.12, 2.8, 5.6, 11.2 C) respectively. When the rate was returned from 2000 to 100 mA g^{-1}, nearly 100% of the 100 mA g^{-1} capacity was recovered. The rate performance was slightly improved by using a thicker interlayer (around 80 μm) (Figure 4.9) for reasons that are not yet clear. Specific capacities of 175, 147, 116, 100 and 86 mA h g^{-1} were obtained at 100, 200, 500, 1000 and 2000 mA g^{-1}, respectively.

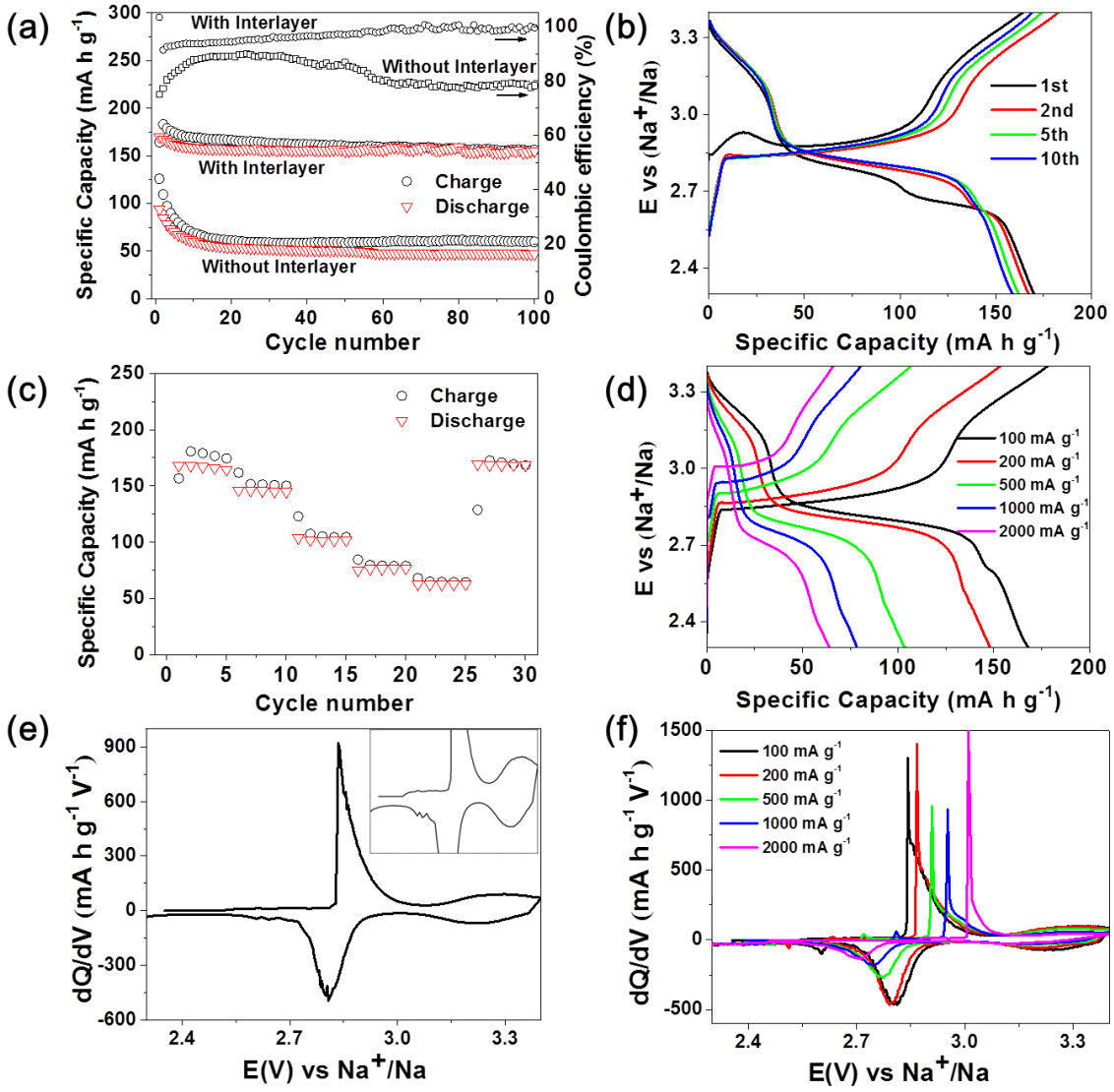

Figure 4.4 (a) Cycling performance of CNT/NaI electrodes with and without an interlayer at 100 mA g^{-1}. (b) 1st, 2nd, 5th, 10th cycle discharge-charge curves of a CNT/NaI electrode containing an interlayer at 100 mA g^{-1}. (c) Rate performance of CNT/NaI containing an interlayer at current densities of 100, 200, 500, 1000, and 2000 mA g^{-1}. (d) Discharge/charge curves of CNT/NaI containing an interlayer cycled at different current densities. (e) Differential capacity plot of the 10th cycle from Fig 4.4b. The inset shows the magnified Fig 4.4e. (f) Differential capacity plot of CNT/NaI electrode cycled at 100, 200, 500, 1000 and 2000 mA h g^{-1}.

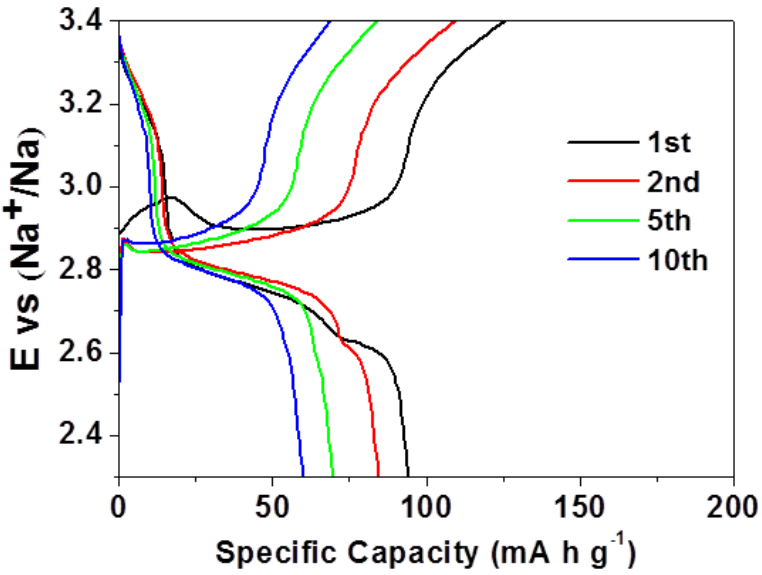

Figure 4.5 1st, 2nd, 5th, and 10th cycle discharge-charge curves of a CNT/NaI electrode without interlayer at 100 mA g^{-1}.

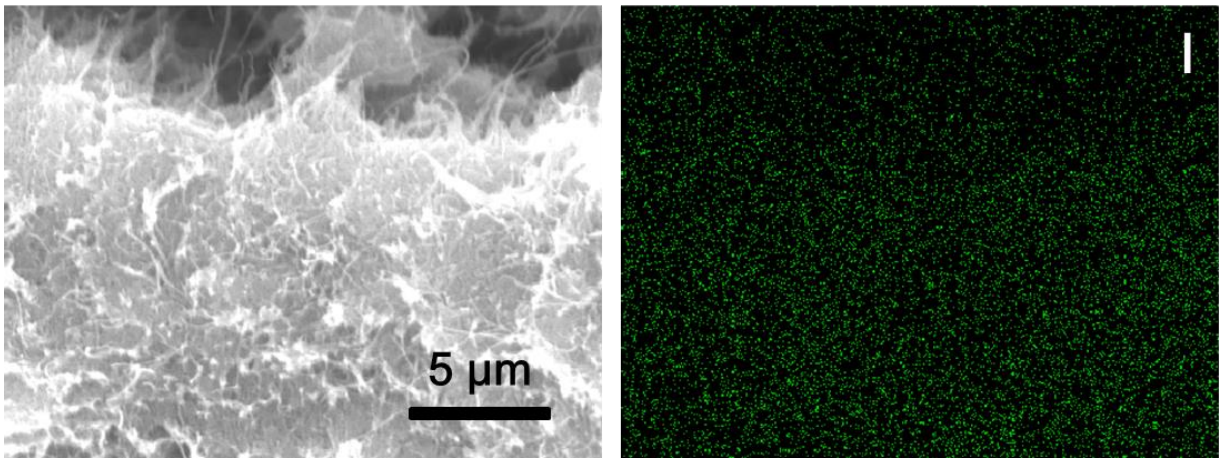

Figure 4.6 Cross-sectional SEM image of a CNT interlayer after cycling and corresponding EDS mapping for I.

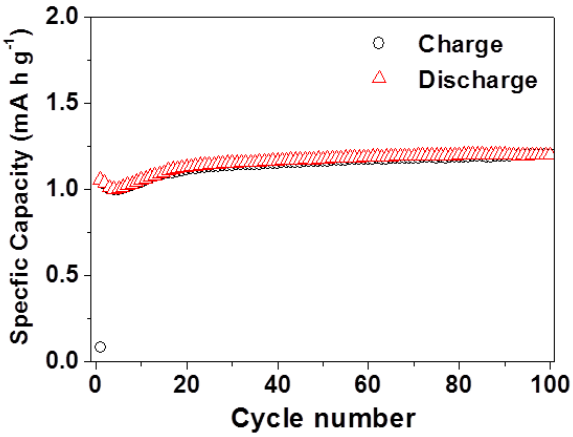

Figure 4.7 Cycling performance of CNT cycled at 100 mA g^{-1} in the voltage range of 2.3-3.4 V.

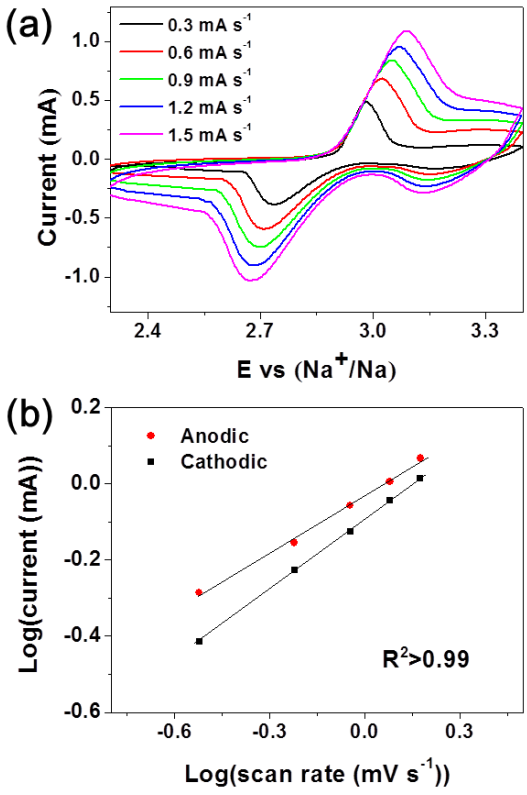

Figure 4.8 (a) Cyclic voltammetry curves of a CNT/NaI electrode at various scan rates of 0.3, 0.6, 0.9, 1.2 and 1.5 mV s^{-1}. (b) The plot of log(peak current) vs. log(scan rate) obtained from fig 3a.

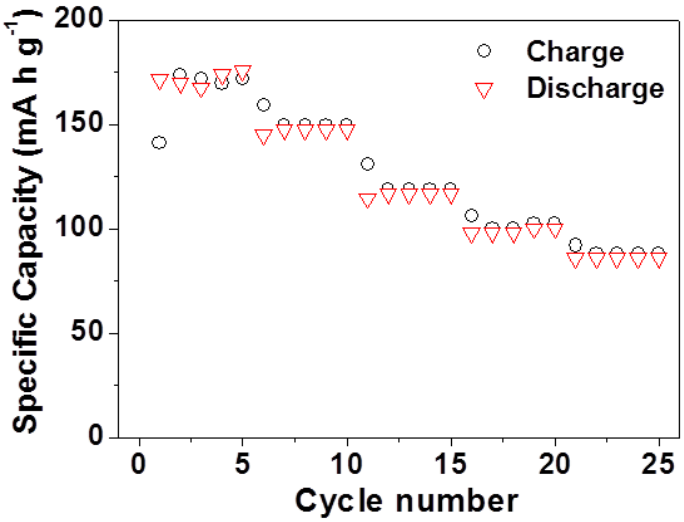

Figure 4.9 Rate performance of CNT/NaI with thick interlayer at current density of 100, 200, 500, 1000, and 2000 mA g^{-1}.

To compare NaI with I_2 as the starting active material, a control experiment was performed using a CNT/I_2 electrode made by the same fabrication process. Figure 4.10 exhibits the normalized capacities (based on theoretical capacities: NaI, 178.8 mA h g^{-1}; I_2, 211 mA h g^{-1}) of NaI and I_2 loaded electrodes cycled at 100 mA g^{-1} over the voltage range of 2.3-3.4 V. Although the cycling stabilities of both electrodes were similar, large initial capacity differences were observed. This is perhaps because I_2 evaporated during the electrode fabrication due to its volatility. While we are not sure if this was the case, it is clearly easier (and safer) to fabricate a NaI-loaded electrode than an I_2-loaded electrode.

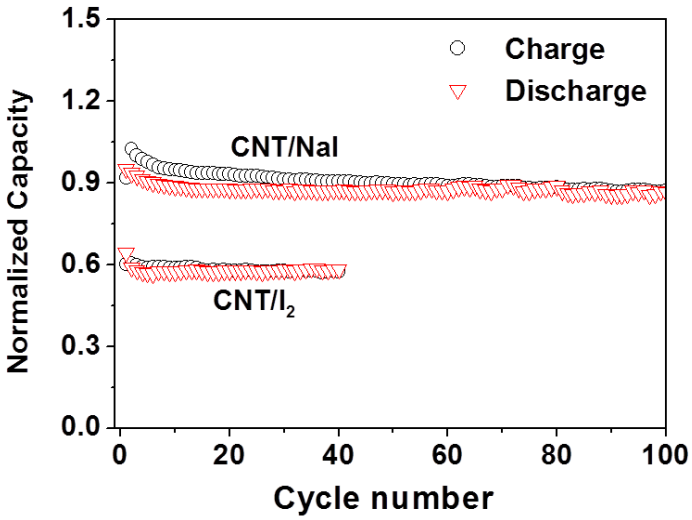

Figure 4.10 Normalized capacity of NaI and I_2 electrodes cycled at 100 mA g^{-1} in the voltage range of 2.3-3.4 V.

Ex situ XPS and Raman were employed to examine the reactions occurring on the CNT/NaI electrodes during cycling. The oxidation states of iodine in pristine CNT/NaI, fully charged CNT/NaI and fully discharged CNT/NaI electrodes were investigated by XPS (Figure 4.11a). XPS spectra were normalized for comparison and peak fitting was performed by using CasaXPS software. Additional peaks located at 1.7 eV higher than the original I $3d_{5/2}$ peaks were observed after charging. These peaks are due to formation of I_2 indicating that I^- was oxidized to a higher oxidation state,[41,42] even though there is a small chance that I_2 can be a decomposition product of remaining I_3^-. The I 3d peak intensity was much smaller in fully charged CNT/NaI resulting in a noisier spectrum, probably because I_2 evaporated under vacuum during XPS measurement due to its volatility. These results support the hypothesis that NaI was converted to I_2 upon charging. After a full discharge to 2.3 V, I $3d_{5/2}$ peak returned to 618.7 eV, suggesting the reduction of I_2 to I^-. In addition to XPS data, the dQdV curves of CNT/NaI and CNT/I_2 electrodes nearly overlapped, supporting our hypothesis that NaI and I_2 go through the same electrochemical reactions (Figure 4.12).

Ex situ Raman was performed on electrodes cycled with and without the CNT interlayer to different states of charge to determine what intermediate species are formed during cycling. The cells were disassembled after discharging/charging and the CNT/NaI electrode and

electrolyte-soaked separators were evaluated. Raman scattering from iodine was not observed from the CNT mat due to the strong visible light adsorption of the (black) CNT mat, thus all Raman measurements were performed on the electrolyte soaked separator (the separator contained residual active materials). Figure 4.11b shows the Raman spectra of electrolyte soaked separator with (right panel) and without (left panel) applying the CNT interlayer during cycling. Raman spectra were acquired when the battery was held at open circuit potential (OCP, grey), charged to 3.05 V (red) and 3.4 V (blue), and discharged to 2.3 V (yellow). All the spectra shows similar vibrational signatures (i.e. peak C-I) in the frequency range between 300 cm^{-1} and 1000 cm^{-1}. Peak C through I are associated with the $NaClO_4$, PC and FEC electrolyte solution.[45-49] Complete vibrational assignments are provided in Table 4.1. Considering the relatively unchanged electrolyte environment during cycling, the relative intensities of all the vibrational modes are normalized to the electrolyte peaks. In particular, Peak G near 850 cm^{-1}, assigned to the symmetric ring vibration of propylene carbonate,[45] was chosen as an intensity reference. As observed in Figure 4b, without applying the CNT interlayer the relative intensity of peak A near 118 cm^{-1} emerges when the cell is charged to 3.05 V. Peak A is associated with the symmetric stretch of $I_3^-(\nu_s(I_3^-))$, the presence of which suggests the conversion of NaI to NaI_3.[43,44] Peak B near 230 cm^{-1} is the asymmetric stretch of $I_3^-(\nu_{as}(I_3^-)$). This peak is influenced by the choice of solvent.[44] The strong I_3^- peak persists even after charging to 3.4 V, while the vibrational signature of I_2, expected near 212 cm^{-1} was not observed.[47] This is probably because I_2 on the separator was converted back to NaI_3 by traveling to and reacting with Na metal after charging was stopped. The I_3^- peak decreased significantly after discharging to 2.3 V, suggesting the formation of the original active material, NaI. In the Raman spectra collected at OCP and discharged to 2.3 V, a broad feature was observed near 131 cm^{-1} which is also observed in the spectra of a separator soaked with the electrolyte (spectrum not shown here). The presence of this artifact is likely a result of the notch filter cut-off at such low frequencies. To examine the influence of CNT interlayer on the dissolution of active materials, Raman spectra from the electrolyte soaked separator from cells with and without the CNT interlayer were compared. The most notable difference is that the intensity of the $\nu_s(I_3^-)$ peak was much smaller when a CNT interlayer was present (Figure 4.11b), indicating the interlayer captures dissolved redox species

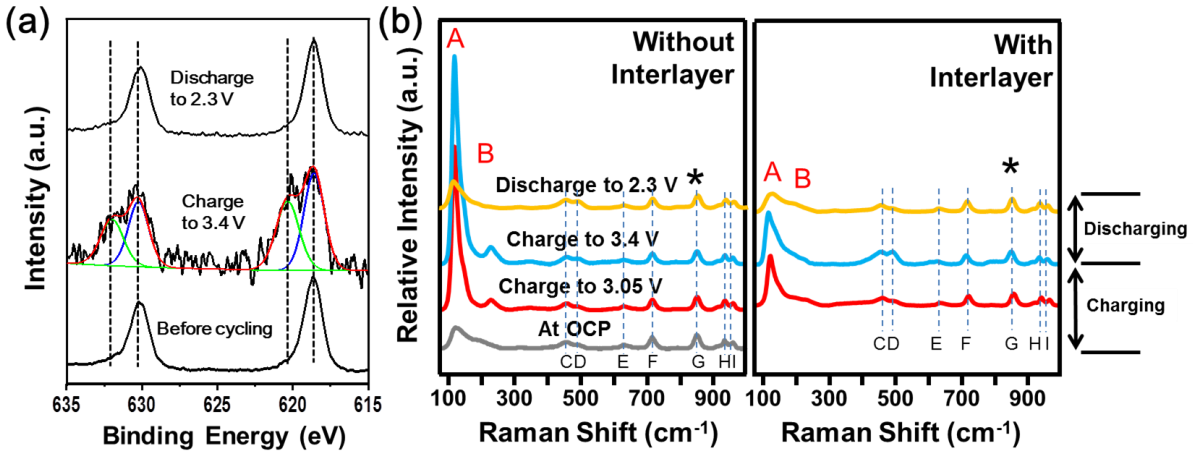

Figure 4.11 (a) XPS spectra of I 3d from CNT/NaI electrodes with interlayer before cycling, after charge, and after discharge. (b) Ex situ Raman spectra obtained from separators during charging and discharging with and without CNT interlayer. All the relative intensities are normalized to peak G (*) at 852 cm^{-1}.

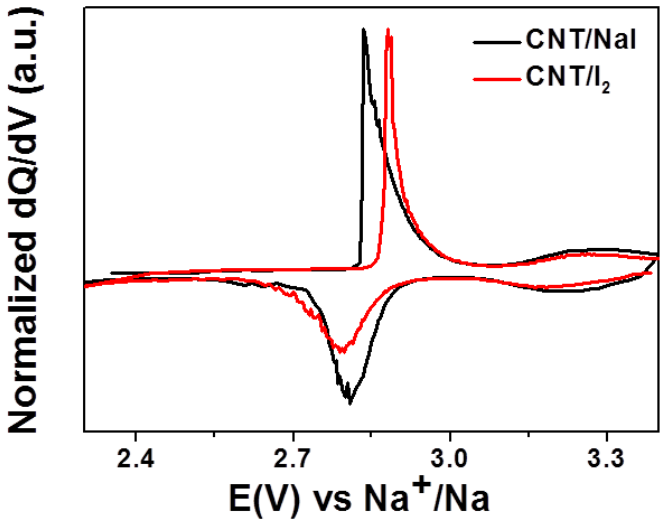

Figure 4.12 Normalized differential capacity plots of the 10th cycle from CNT/NaI and CNT/I_2 electrodes.

Based on the XPS and Raman data, the electrochemical reactions during cycling are proposed as follows.

$$1)\ 2\mathrm{NaI} \leftrightarrow \frac{2}{3}NaI_3 + \frac{4}{3}Na^+ + \frac{4}{3}e^-$$

$$2)\ \frac{2}{3}\mathrm{NaI}_3 \leftrightarrow I_2 + \frac{2}{3}Na^+ + \frac{2}{3}e^-$$

$$\text{Overal reaction}:\ 2\mathrm{NaI} \leftrightarrow I_2 + 2Na^+ + 2e^-$$

The ratio of actual capacities delivered in the voltage range of 3.4-2.87 V and 2.87-2.3 V are 28.5 and 71.5 %, respectively (10th discharge basis) which deviated slightly from theoretical values (33.3 and 66.6 %). This is perhaps because the conversion of NaI_3 to I_2 is not perfect in the charge process due to shuttling, leading to a reduced capacity in the following discharge.

4.3 Conclusions

In conclusion, CNT/NaI electrodes fabricated by a solution infiltration, evaporation and precipitation method were demonstrated as a SIBs cathode for the first time. The CNT/NaI cathode exhibited an initial specific capacity of 170 mA h g^{-1} at 100 mA h g^{-1} with two discharge plateaus shown above 2.8 V, giving an energy density of 473 W h kg^{-1} vs. Na metal, making it highly competitive among previously reported high voltage Na-ion battery cathode materials (Figure 4.13). The CNT/NaI electrodes showed high capacity retention of 92 % after 100 cycles and small hysteresis (0.03 V). Shuttling was significantly suppressed with the addition of a CNT interlayer and FEC to the electrolyte, the combination of which limit the loss of active materials during cycling. Based on ex situ XPS and Raman results, it was confirmed that NaI is converted to NaI_3 and I_2 sequentially during charging and I_2 is converted back to NaI reversibly in an opposite sequence during discharging. I demonstrate the potential of NaI as a battery cathode for SIBs and CNT as an interlayer and electrode platform. This work may spur further research and development on NaI-based cathodes.

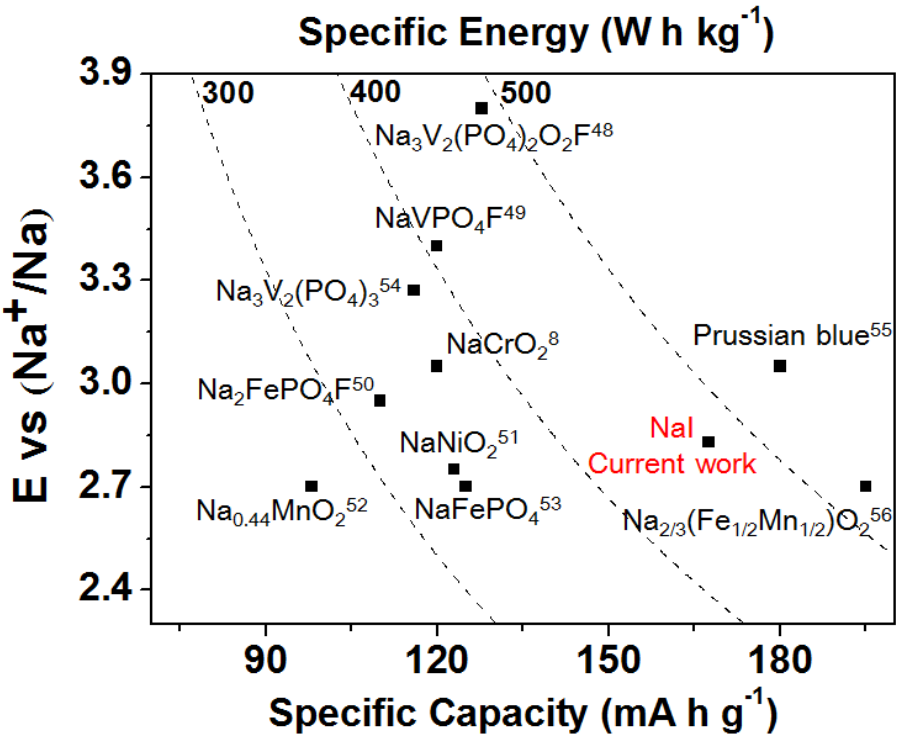

Figure 4.13 Electrochemical characteristics of representative high voltage Na-ion battery cathode materials and NaI.[8, 48-56]

peak label	frequency (cm^{-1})	Assignments	References
A	118	I_3^- symmetric stretch	43, 44
B	225	I_3^- asymmetric stretch	44
C	455	carbonate binding (PC)	45
D	487	carbonate binding (FEC)	
E	630	Associated with PC, Observed, not assigned	
F	715	ring skeletal bending	
G	850	symmetric ring vibration	
H	930	ClO_4^- symmetric stretch	46
I	958	carbonate symmetric strech	45

Table 4.1 Vibrational assignments of 1.5 M $NaClO_4$ in PC with 5 wt % FEC electrolyte and NaI active material

4.4 Experimental section

Synthesis of CNT mat: A 8~9 wt % MWCNT (Multiwalled Carbon Nanotubes) solution (Aladdin) was cast onto a PVDF filter film (Taobao) which is horizontally placed on a glass substrate and dried at room temperature for 12 hours to form a MWCNT film. The thickness of MWCNT was controlled by the amount of MWCNT solution casted (mats used for experiments were 40~50 μm thick). The MWCNT film was baked at 150 ℃ for 2 hours to reduce the electrical resistance.

Synthesis of CNT/NaI electrode: A 0.44 M NaI solution was prepared by dissolving sodium iodide (NaI, Acros) in anhydrous ethanol with stirring overnight in a glove box. The CNT film was punched into round shape pieces with a diameter of 8 mm and 40~50 μm thickness. The cut CNT electrodes were transferred into the glove box and directly used as a free standing electrode without a current collector or additional binder. Because NaI is air and moisture sensitive, the rest of steps were all done in the glove box. A NaI solution was dropped onto the CNT electrode using a micropipette and the ethanol completely dried. The areal NaI loading is 1.2 mg cm^{-2}. At larger areal loadings shuttling becomes significant at 100 mA g^{-1}, so larger loading were not investigated.

Sample Characterization: SEM and EDS were conducted using a Hitachi S-4700 SEM equipped with an Oxford INCA energy dispersive X-ray analyzer. XPS analysis were performed using a Kratos Axis Ultra XPS system with a monochromatic Al Kα (1486.6 eV) source. Binding energies were calibrated based on the C 1s peak (284.4 eV). To minimize air exposure time, sample preparation for SEM and XPS measurement was done in the glove box. A sample holder with sample attached was put in a bottle filled with Ar gas and tightly sealed. The sample holder was taken from the bottle just before transferring to the vacuum chamber. The vacuum chamber was immediately evacuated. The air exposure time was less than 1 second. XRD was done by a Philips X'pert MRD XRD (Materials Research Diffractometer) using Cu Kα radiation (λ = 0.15418 nm, Scan step size: 0.05°, Time per step: 5 sec). The CNT/NaI sample was prepared in the glove box and covered with Kapton tape to prevent the oxidation of NaI. Raman spectra were recorded by a Shamrock SR-303i monochromator (Andor Tech) equipped with a iDus 420 spectroscopy Charge-Coupled Device (CCD) detector (Andor Tech). A 532 nm laser (B&W Tek Inc.) was used as an excitation source. The CNT/NaI sample was taken out of swagelock cell and

transferred to the cell for Raman measurement. The cell was assembled and made airtight in the glovebox prior to measurement. Quartz was used as an optical window.

Electrochemical Measurements: 1.5 M $NaClO_4$ in PC containing 5 wt % FEC was used as electrolyte and sodium foil (Na, Sigma Aldrich) was used as the counter electrode for two-electrode cells. When indicated, a CNT mat of 40~50 μm thickness was inserted between the CNT/NaI cathode and separator as an interlayer. All cells were assembled in the glove box. Galvanostatic discharge/charge tests and cyclic voltammetry were performed using a VMP3, Bio-Logic potentiostat and swagelok-type cells over a voltage range of 2.3 to 3.4 V vs. Na/Na^+ at room temperature. Current densities and specific capacities were calculated based on NaI. The weight of active materials was determined as follows: weight of active materials = concentration of NaI solution (0.44M) × total amount of solution dropped on CNT mat.

4.5 References

[1] M. Armand, J.-M. Tarascon, *Nature* **2008**, *451*, 652.

[2] J. B. Goodenough, *Acc. Chem. Res.* **2012**, *46*, 1053.

[3] M. Armand, J.-M. Tarascon, *Nature* **2001**, *414*, 359.

[4] H. Kim, H. Kim, Z. Ding, M. H. Lee, K. Lim, G. Yoon, K. Kang, *Adv. Energy Mater.* **2016**, *6*, 1600943.

[5] M. D. Slater, D. Kim, E. Lee, C. S. Johnson, *Adv. Funct. Mater.* **2013**, *23*, 947.

[6] S. Y. Hong, Y. Kim, Y. Park, A. Choi, N.-S. Choi, K. T. Lee, *Energy Environ. Sci.* **2013**, *6*, 2067.

[7] V. Raju, J. Rains, C. Gates, W. Luo, X. Wang, W. F. Stickle, G. D. Stucky, X. Ji, *Nano Lett.* **2014**, *14*, 4119.

[8] C.-Y. Yu, J.-S. Park, H.-G. Jung, K.-Y. Chung, D. Aurbach, Y.-K. Sun, S.-T. Myung, *Energy Environ. Sci.* **2015**, *8*, 2019.

[9] D. Yuan, X. Liang, L. Wu, Y. Cao, X. Ai, J. Feng, H. Yang, *Adv. Mater.* **2014**, *26*, 6301.

[10] S. Kim, S.-K. Kim, P. Sun, N. Oh, P. V. Braun, *Nano Lett.* **2017**, *17*, 6893.

[11] K. Li, B. Lin, Q. Li, H. Wang, S. Zhang, C. Deng, *ACS Appl. Mater. Interfaces* **2017**, *9*, 20508.

[12] K. Lu, Z. Hu, J. Ma, H. Ma, L. Dai, J. Zhang, *Nat. Commun.* **2017**, *8*, 527.

[13] H. Wang, G. Zhang, L. Ke, B. Liu, S. Zhang, C. Deng, *Nanoscale* **2017**, *9*, 9365.

[14] Y. Wang, Q. Sun, Q. Zhao, J. Cao, S. Ye, *Energy Environ. Sci.* **2011**, *4*, 3947.

[15] Q. Zhao, Y. Lu, Z. Zhu, Z. Tao, J. Chen, *Nano Lett.* **2015**, *15*, 5982.

[16] V. Anju, M. P. Austeria, S. Sampath, *Adv. Mater. Interfaces* **2017**, *4*, 1700151.

[17] Z. Wu, J. Xu, Q. Zhang, H. Wang, S. Ye, Y. Wang, C. Lai, *Energy Storage Mater.* **2018**, *10*, 62.

[18] D. Gong, B. Wang, J. Zhu, R. Podila, A. M. Rao, X. Yu, Z. Xu, B. Lu, *Adv. Energy Mater.* **2017**, *7*, 1601885.

[19] S. Komaba, W. Murata, T. Ishikawa, N. Yabuuchi, T. Ozeki, T. Nakayama, A. Ogata, K. Gotoh, K. Fujiwara, *Adv. Funct. Mater.* **2011**, *21*, 3859.

[20] J. Qian, X. Wu, Y. Cao, X. Ai, H. Yang, *Angew. Chem., Int. Ed.* **2013**, *125*, 4731.

[21] Y. Xu, Y. Zhu, Y. Liu, C. Wang, *Adv. Energy Mater.* **2013**, *3*, 128.

[22] Y. Zhu, X. Han, Y. Xu, Y. Liu, S. Zheng, K. Xu, L. Hu, C. Wang, *ACS nano* **2013**, *7*, 6378.

[23] Y. Fu, Y. S. Su, A. Manthiram, *Adv. Energy Mater.* **2014**, *4*, 1300655.

[24] H. X. Zhang, C. Feng, Y. C. Zhai, K. L. Jiang, Q. Q. Li, S. S. Fan, *Adv. Mater.* **2009**, *21*, 2299.

[25] Y.-S. Su, A. Manthiram, *Nat. Commun.* **2012**, *3*, 1166.

[26] Y.-S. Su, A. Manthiram, *Chem. Commun.* **2012**, *48*, 8817.

[27] X. Wang, Z. Wang, L. Chen, *J. Power Sources* **2013**, *242*, 65.

[28] H. Xia, Y. Wang, J. Lin, L. Lu, *Nanoscale Res. Lett.* **2012**, *7*, 1.

[29] H. Yi, H. Wang, Y. Jing, T. Peng, Y. Wang, J. Guo, Q. He, Z. Guo, X. Wang, *J. Mater. Chem. A* **2015**, *3*, 19545.

[30] A. V. Naumkin, A. Kraut-Vass, S. W. Gaarenstroom, C. J. Powell, NIST X-ray Photoelectron Spectroscopy Database, Version 4.1 (National Institute of Standards and Technology, Gaithersburg) **2012**, http://srdata.nist.gov/xps/.

[31] J. F. Moulder, W. F. Stickel, P. E. Sobol, K. D. Bomben, *Handbook of X-Ray Photoelectron Spectra*, Perkin Elmer, Eden Prairie, MN, USA **1992**.

[32] C. Strydom, J. Van Staden, H. Strydom, *Electroanalysis* **1991**, *3*, 197.

[33] J. T. Lee, Y. Zhao, S. Thieme, H. Kim, M. Oschatz, L. Borchardt, A. Magasinski, W. I. Cho, S. Kaskel, G. Yushin, *Adv. Mater.* **2013**, *25*, 4573.

[34] L. Suo, Y.-S. Hu, H. Li, M. Armand, L. Chen, *Nat. Commun.* **2013**, *4*, 1481.

[35] E. Markevich, G. Salitra, D. Aurbach, *ACS Energy Lett.* **2017**, *2*, 1337.

[36] J.-H. Song, J.-T. Yeon, J.-Y. Jang, J.-G. Han, S.-M. Lee, N.-S. Choi, *J. Electrochem. Soc.* **2013**, *160*, A873.

[37] S. Komaba, T. Ishikawa, N. Yabuuchi, W. Murata, A. Ito, Y. Ohsawa, *ACS Appl. Mater. Inter.* **2011**, 3, 4165.

[38] L. W. Ji, M. Gu, Y. Y. Shao, X. L. Li, M. H. Engelhard, B. W. Arey, W. Wang, Z. M. Nie, J. Xiao, C. M. Wang, J. G. Zhang, J. Liu, *Adv. Mater.* **2014**, 26, 2901.

[39] V. Augustyn, J. Come, M. A. Lowe, J. W. Kim, P.-L. Taberna, S. H. Tolbert, H. D. Abruña, P. Simon, B. Dunn, *Nat. Mater.* **2013**, *12*, 518.

[40] T. Brezesinski, J. Wang, S. H. Tolbert, B. Dunn, *Nat. Mater.* **2010**, *9*, 146.

[41] T. G. Levitskaia, S. Chatterjee, B. W. Arey, E. L. Campbell, Y. Hong, L. Kovarik, J. M. Peterson, N. K. Pence, J. Romero, V. Shutthanandan, *RSC Adv.* **2016**, *6*, 76042.

[42] C. Vogt, T. R. Gengenbach, S. L. Chang, G. P. Knowles, A. L. Chaffee, *J. Mater. Chem. A* **2015**, *3*, 5162.

[43] A. E. Johnson, A. B. Myers, *J. Phys. Chem.* **1996**, *100*, 7778.

[44] U. L. Štangar, B. Orel, A. Š. Vuk, G. Sagon, P. Colomban, E. Stathatos, P. Lianos, *J. Electrochem. Soc.* **2002**, *149*, E413.

[45] G. Janz, J. Ambrose, J. Coutts, J. Downey Jr, *Spectrochim. Acta, Part A* **1979**, *35*, 175.

[46] H.-Y. Song, T. Fukutsuka, K. Miyazaki, T. Abe, *Phys. Chem. Chem. Phys.* **2016**, *18*, 27486.

[47] H. L. Strauss, *J. Indian Inst. Sci.* **1988**, *68*, 493.

[48] K. Saravanan, C. W. Mason, A. Rudola, K. H. Wong, P. Balaya, *Adv. Energy Mater.* **2013**, *3*, 444.

[49] T. Jin, Y. Liu, Y. Li, K. Cao, X. Wang, L. Jiao, *Adv. Energy Mater.* **2017**, *7*, 1700087.

[50] Y. Kawabe, N. Yabuuchi, M. Kajiyama, N. Fukuhara, T. Inamasu, R. Okuyama, I. Nakai, S. Komaba, *Electrochem. Commun.* **2011**, *13*, 1225.

[51] P. Vassilaras, X. Ma, X. Li, G. J. Ceder, *Electrochem. Soc.* **2013**, *160*, A207.

[52] P. Zhan, S. Wang, Y. Yuan, K. Jiao, S. J. Jiao, *Electrochem. Soc.* **2015**, *162*, A1028.

[53] S.-M. Oh, S.-T. Myung, J. Hassoun, B. Scrosati, Y.-K. Sun, *Electrochem. Commun.* **2012**, *22*, 149.

[54] J. Z. Guo, P. F. Wang, X. L. Wu, X. H. Zhang, Q. Yan, H. Chen, J. P. Zhang, Y. G. Guo, *Adv. Mater.* **2017**, *29*, 1701968.

[55] Y. You, X.-L. Wu, Y.-X. Yin, Y.-G. Guo, *Energy Environ. Sci.* **2014**, *7*, 1643.

[56] S. Kalluri, K. H. Seng, W. K. Pang, Z. Guo, Z. Chen, H.-K. Liu, S. X. Dou, *ACS Appl. Mater. Interfaces* **2014**, *6*, 8953.

CHAPTER 5
HIGH VOLUMETRIC AND GRAVIMETRIC CAPACITY ELECTRODEPOSITED MESOSTRUCTURED Sb_2O_3 SODIUM ION BATTERY ANODES

5.1 Introduction

Although LIBs are the dominant energy storage system for portable devices and electric vehicles, increasing demands for low cost and large-scale energy storage has led to intensive investigation of SIBs, driven in particular by the relatively high cost and limited availability of lithium, relative to sodium.[1-3] Along with being abundant and low cost[1-3], the fact that Na behaves differently than Li, which may open opportunities for new chemistries, should also not be discounted.[4] A particular challenge of SIBs, however, is the limited number of anode materials. Hard carbon has been considered as an option, however carboneous Na anodes have rather low practical capacities (~300 mAh g-1) which results in a low energy density.[5-9]

Metallic antimony (Sb) is considered as a promising SIB anode material, in particular relative to hard carbon, because of its significantly higher theoretical gravimetric (660 mA h g-1) and volumetric (1130 mA h cm^{-3}) capacities assuming formation of Na_3Sb, relatively low reaction voltage (0.4 V vs. Na), and small hysteresis (0.3 V).[10-13] However, Sb undergoes a large volume expansion of 293% upon sodiation,[14] considerably greater than for the lithiation of Sb to Li_3Sb (135 %) because of the large ionic size of Na compared to that of Li.[15] Thus, there must be sufficient free volume available within the electrode to accommodate the volume expansion. Providing free volume to enhance the performance of conversion and alloying electrodes is not a new idea, and many groups have designed electrodes from nanowire, nanotube, hollow and core-shell structures to provide the required free volume,[11,16-19] or buffered the volume expansion by embedding the active materials into graphene and carbon nanofiber-based structures.[13,20-22] A significant challenge of these approaches is that while the electrodes could sometimes exhibit good gravimetric capacities and cycling performance, their active material loading is generally small, leading to low volumetric capacities.[23]

Another problem not limited to Sb, originating from repeated volume expansion and contraction in alloying electrodes, is active material pulverization concurrent with loss of electrical contact within electrode and continual growth of SEI.[23-25] In the case of Sb, to address pulverization, the use of Sb_2O_3 rather than Sb has been considered. During sodiation,

Sb_2O_3 first converts into Sb nanoprecipitates in an amorphous Na_2O matrix.[26-30] The ductile and soft Na_2O matrix then alleviates the stress generated as the Sb precipitates sodiate.[26-30]

In this chapter, I present the fabrication and cycling performance of 3D Ni inverse opal supported NiSb/Sb_2O_3 (3D Ni@NiSb/Sb_2O_3) anodes. I show that an engineered 3D conductive scaffold, with the appropriate active materials loading provides a high gravimetric and volumetric capacity and a stable cycling behavior. The key advantage of the 3D porous electrode is that it effectively accommodates large volume changes with cycling and enables a high active material loading.[23,31] To the best of my knowledge, this is the first application of a 3D metallic support network for a SIB electrode.

5.2 Results and discussion

The 3D Ni scaffold was formed by Ni electrodeposition through a PS colloidal template following our published approach[32] (Figure 5.1). In contrast to my prior work (Chapter 2), the PS colloidal template was annealed at 97 ℃ instead of 95~96 ℃. While this might not seem significant, it is in fact important, as the higher annealing temperature resulted in increased sintering of the PS particles, which in turn resulted in larger pore interconnects in the final Ni scaffold (contrast Figure 5.1a and 5.1b) which I found were necessary to prevent closure of the pore network during the sodiation-induced volume expansion of the active material. As shown in Figure 5.1a and 5.1b, the pore size of interconnects was increased from 180 nm to 210 nm simply by the increased sintering temperature. This approach was much simpler than using chemical etching or electrochemical polishing.[33,34] Active materials were deposited onto the Ni scaffold by pulsed electrodeposition. Pulsed, rather than constant current electrodeposition was used to provide a conformal active material coating throughout Ni scaffold. In brief, a pulsed electrodeposition enabled ions consumed by electrodeposition within the 3D scaffold to be replenished by diffusion during rest time before the subsequent deposition pulse. The mass of active materials deposited was controlled by the number of pulses. The as-deposited sample was annealed at 300 ℃ for 1 h in air to improve the crystallinity of the active material and adhesion between the active material and Ni current collector. As shown by Figure 5.1c, following annealing (as well as before annealing, not shown) the active materials uniformly coat on the Ni

inverse opal. Importantly, the 3D electrode retains its open pore structure, as required to ensure electrolyte accessibility.

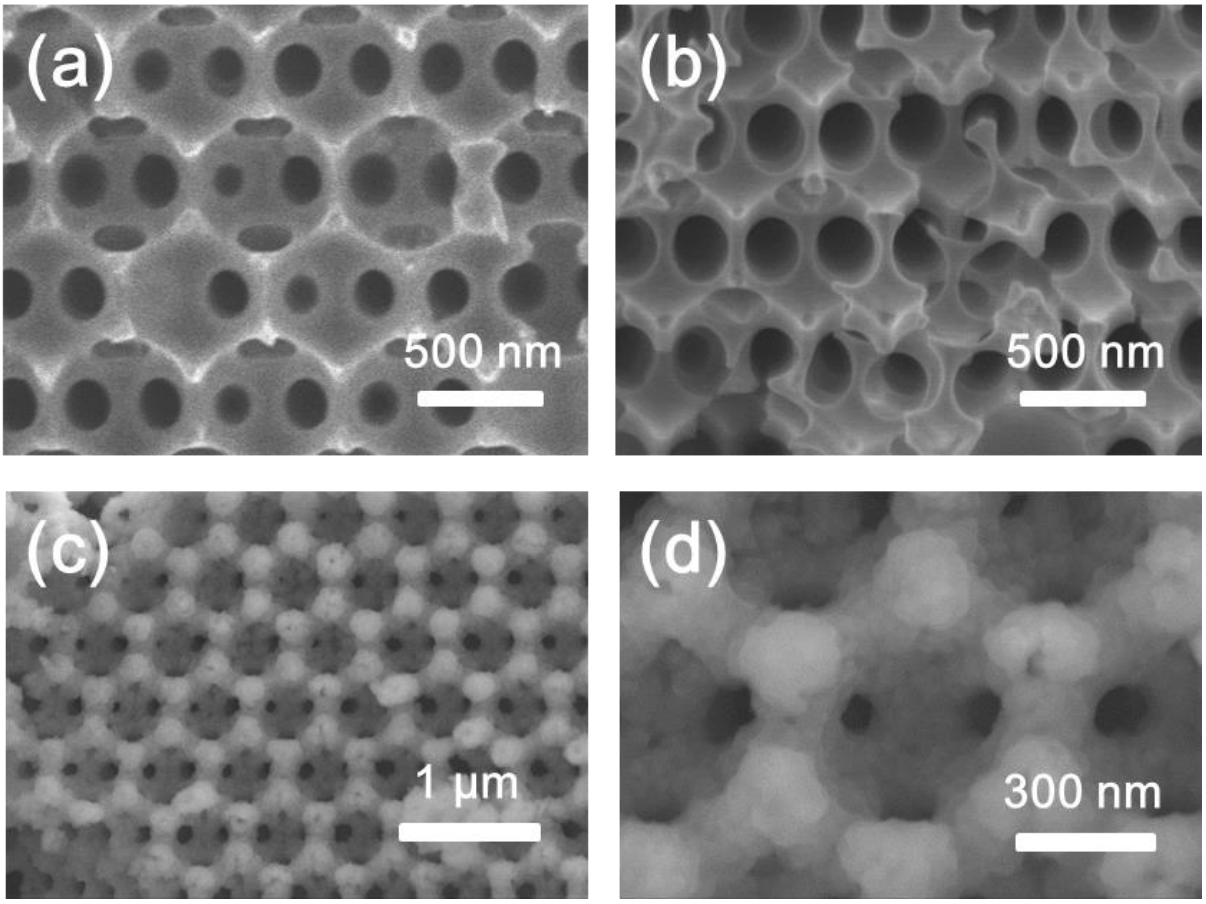

Figure 5.1 Cross-sectional SEM images of 3D Ni sintered at (a) 95 ℃ (b) 97 ℃ and (c) 3D Ni@NiSb/Sb_2O_3 (1.1 g cm^{-3} loading) after heat treatment 300 ℃ for 1 h in air. (d) higher-magnification image of the same 3D Ni@NiSb/Sb_2O_3 electrode.

XRD was performed on the samples before and after the annealing step. In the as-grown sample, only Ni (scaffold) and W (substrate) peaks were observed (Figure 5.2a). Following the heat treatment, Sb_2O_3 and NiSb diffraction peaks emerged. To determine the origin of the Sb_2O_3 phase, a series of experiments were performed as detailed here. The mass change (deposited material basis) with annealing was found to be only about 1% indicating Sb_2O_3 is not formed due to oxidation by air. To explore if significant chemical reactions occurred during the heat treatment which netted out to a minimal overall mass change, TGA was performed in air on an

as-deposited sample (Figure 5.3). As the sample was ramped to 300 ℃ at 5 ℃/min. and then held at 300 ℃ for 1 h it slowly lost 2.7% mass (deposited materials basis). If the sample started to oxidize at some temperature, I would have expected to see a mass gain (or at least a significant change in slope) over some temperature range. I suspect the small mass loss is simply due to desorption of organic and water molecules during annealing. Based on the combination of the XRD and TGA data, I speculate that an amorphous Sb/Sb_2O_3 phase was formed during electrodeposition which converts to crystalline Sb_2O_3 and NiSb (Ni is provided from Ni scaffold) during heat treatment. This speculation is consistent with previous reports which indicate a mixture of Sb and Sb_2O_3 is formed by electrodeposition from a potassium antimony tartrate electrolyte in the absence of HCl, while only Sb is deposited when the pH is reduced to 1.3 with HCl.[35,36] In my system, acid was not added to the electrolyte. I can only speculate why my as-deposited materials appear amorphous, while they were crystalline in the previous reports, but perhaps it is because we use pulsed deposition with a short pulse time (0.25 s), which was not the case in the literature. Finally, EDS was performed to check the electrode composition. Only Sb, O and Ni were observed (Figure 5.2b). Elemental mappings show Sb and O were distributed uniformly on the 3D $Ni@NiSb/Sb_2O_3$ electrode (Figure 5.2c).

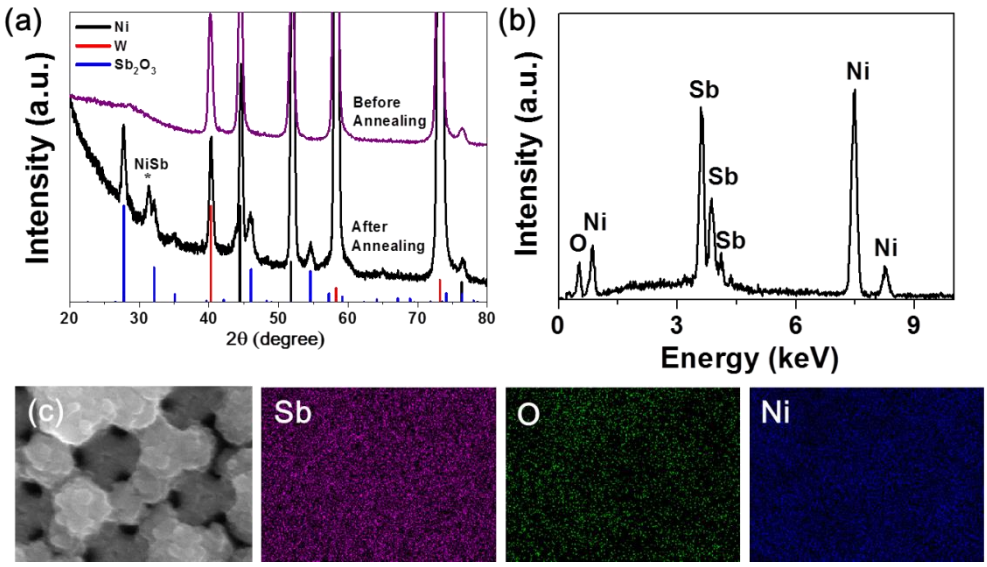

Figure 5.2 (a) XRD of as-deposited 3D electrodes before and after heat treatment. (b) EDS spectrum of a 3D $Ni@NiSb/Sb_2O_3$ electrode. (c) Top SEM image of the electrode and corresponding Sb, O and Ni EDS mapping.

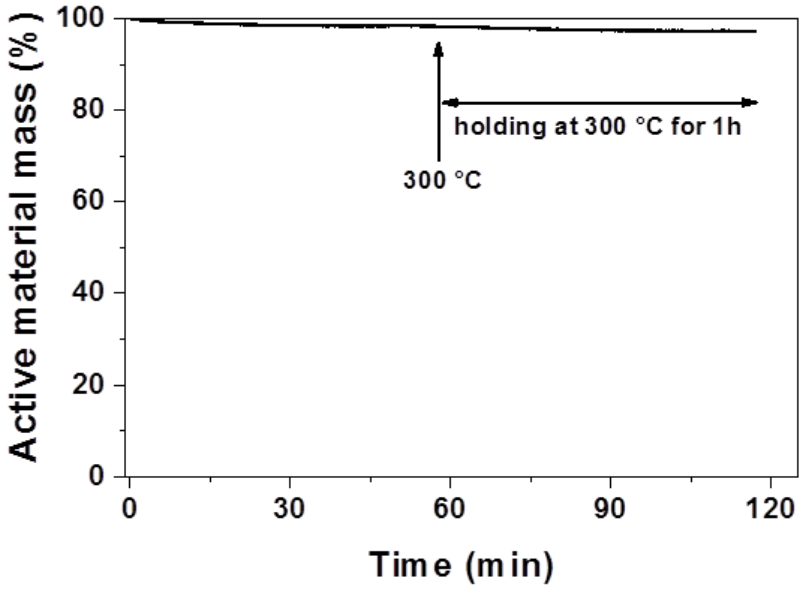

Figure 5.3 TGA curve of a 3D Ni@NiSb/Sb_2O_3 electrode. The mass of as-deposited active material is 1.2 mg.

The specific and volumetric capacities of three electrodes with different loadings were measured to determine the effect of loading. All electrodes had the same area and thickness to enable comparison. All electrodes were cycled 5 times and their 5^{th} discharge capacities are presented in Figure 5.4. The specific and volumetric capacities show an inverse relationship with loading. As the loading increases, the specific capacity decreases which I speculate is due to several factors, including the longer solid-state diffusion lengths, and the fact that free volume expansion may be becoming suppressed by sodiation-induced stress in the confined pore space. Because active material utilization falls-off only slowly as the loading increases, the volumetric capacity continues to increases with loading. The sum of the volumetric and specific capacities was highest at a loading of 1.1 g cm^{-3}, thus a loading of 1.1 g cm^{-3} was chosen for most studies presented here.

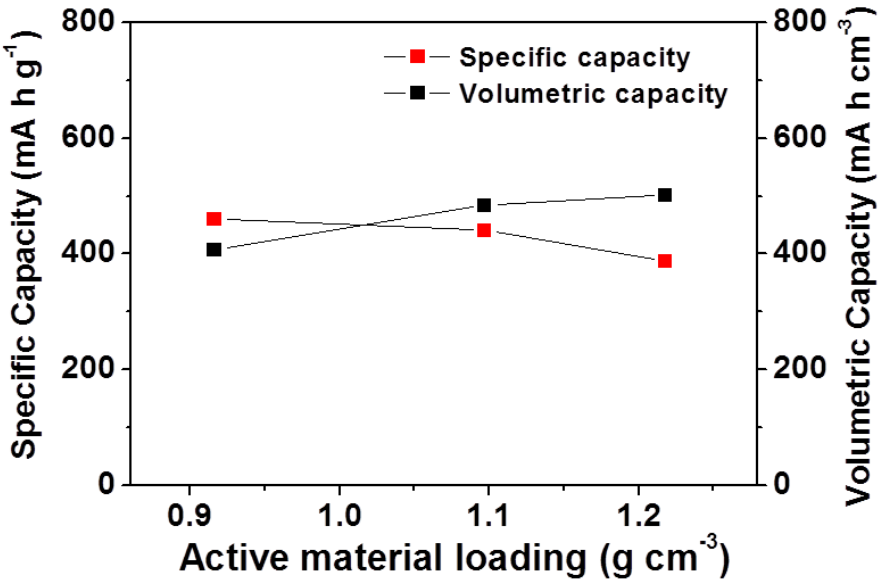

Figure 5.4 Specific and volumetric capacity of 3D Ni@NiSb/Sb_2O_3 electrodes with different active material loadings at 5th cycle. All electrodes were tested at specific current of 200 mA g^{-1}

The electrochemical properties of 3D Ni/NiSb/Sb_2O_3 electrodes were evaluated by galvanostatic discharge/charge testing at room temperature. Figure 5.5a shows the cycling performance of 3D Ni/NiSb/Sb_2O_3 at 200 mA g^{-1} over 200 cycles. The 3D NiSb/Sb_2O_3 electrode exhibits first and second discharge capacities of 714 and 441 mA h g^{-1}, respectively. This irreversible capacity loss is commonly observed in the conversion anodes and is due to incomplete desodiation and the formation of SEI.[37,38] The 3D Ni/NiSb/Sb_2O_3 specific capacity gradually increased to 445 mA h g^{-1} over about 30 cycles, indicating some sort of an activation process (an effect frequently observed in alloying-type anodes).[3,27] The discharge capacity faded slightly to 397 mA h g^{-1} after 200 cycles, which corresponds to 89 % capacity retention relative to the maximum discharge capacity of 445 mA h g^{-1} at the 30th cycle. In spite of the stable cycling performance, the 3D Ni@NiSb/Sb_2O_3 electrode shows a relatively low coulombic efficiency (Figure 5.6) similar to that previously reported for other Sb_2O_3-based SIB anodes.[26,27,36] The two most likely reasons for the low coulombic efficiency are SEI formation, and irreversibility of the Sb_2O_3 conversion reaction (Sb_2O_3 + 6Na ↔ 2Sb + 3Na_2O). Here, FEC was added to the electrolyte to improve the cycling performance, as it has previously been demonstrated to enhance the formation of a stable and thin SEI layer on the surface of an

anode.[39,40] However, FEC decomposition during discharging can lead to low coulombic efficiency. About 0.12 mmol of FEC was contained in the electrolyte within the cell. Assuming FEC decomposition is the only reason for the observed ~95% coulombic efficiency, this is considerable greater than the amount of FEC required for FEC decomposition to be the only irreversible mechanism over 200 cycles. Along with FEC decomposition, the electrochemically active phase gradually irreversibly changes from Sb_2O_3 to Sb (will be discussed later), with cycling, indicating Na_2O is not fully decomposable during charging. Although the coulombic efficiencies of initial cycles were low (below 95%), the efficiency gradually increased to 95.8 % by the 200th cycle as the system stabilized. I am not the first to report this issue, and a relatively low coulombic efficiency is commonly observed in the Sb_2O_3 system when electrolytes containing FEC are used.[26, 27, 41]

As one demonstration of the effect of the Ni scaffold, a 3D-structured scaffold-free Sb electrode synthesized by potentiostatic electrodeposition through a PS opal template was evaluated. Note, synthesis of a 3D-structured scaffold-free Sb_2O_3 electrode, which would have been a true control experiment, was attempted using a potassium antimony tartrate electrolyte. However, this was not successful as the PS template was damaged by the electrolyte. Sb was chosen instead, as it undergoes similar reactions as Sb_2O_3, as well as a similar large volume change. The cycling performance of this electrode was evaluated at a current density of 200 mA g^{-1} (Figure 5.7). A rapid capacity decay was observed during cycling, which in conjunction with the good cycling performance of the 3D Ni/NiSb/Sb_2O_3 at least suggests it is the mechanically robust and conductive Ni scaffold that enables good capacity retention in the 3D Ni/NiSb/Sb_2O_3 system.

In the 1.1 g cm^{-3} loaded electrodes, an electrode-basis volumetric capacity as high as 488 mA h cm^{-3} was obtained, corresponding to 34.3 % of the theoretical volumetric capacity of Sb_2O_3. The theoretical volumetric capacity of Sb_2O_3 is 1420 mA h cm^{-3}, assuming Sb_2O_3 reacts with 12 mole of Na ($Sb_2O_3 + 12Na \rightarrow 3Na_2O + 2Na_3Sb$, $\Delta V = 304$ %). As I show, a higher loading, and thus volumetric capacity was possible, but not desirable as it leads to a lower specific capacity and faster capacity decay (Figure 5.8). The practical volumetric capacity is expected to be lower than the theoretical capacity because of pinch-off and electrolyte accessibility issues. It is important to point out that while most reports mention only specific capacities, in conversion and alloying systems such as these, where large volume expansions

occur, the volumetric capacity of the sodiated form is critical, as this is an important engineering parameter for determination of the actual volumetric battery capacity.

Figure 5.5b shows discharge-charge curves of the 3D Ni/NiSb/Sb_2O_3 electrode. The 1st discharge curve is rather different than subsequent cycles due to a first discharge activation process. dQ/dV curves (Figure 5.5c and 5.5d) were obtained by differentiating the charge/discharge voltage curves (Figure 5.5b) to investigate the reaction chemistry in more detail. In the first discharge, the peak at 0.95 V can be attributed to the reduction of Sb_2O_3 to Sb and Na_2O.[26,42] The peaks at 0.64 and then 0.7 V can be ascribed to the formation first of Na_xSb and then Na_3Sb, indicating the stepwise reduction of Sb.[26,43] In the following charge, the oxidation peaks at 0.71 and 0.81 V are due to the dealloying reactions of Na_3Sb to Sb.[26,39] The peak at 1.6 V corresponds to the oxidation reaction of Sb and Na_2O to Sb_2O_3.[26,44] Both conversion and alloying reaction were confirmed by dQ/dV. The intensity of conversion redox peaks decreased with cycling, indicating the conversion reaction became partially irreversible. Retention of Na_2O produced upon conversion may actually be beneficial for stable cycling performance as it buffers the strain/stress caused by the volume change during cycling.[45] In contrast, the intensity of alloying redox peaks increased with cycling, indicating more Sb becomes electrochemically active. The peak potentials also shift with cycling, indicating the environment of the active materials changed. This is not surprising, as it is known the crystallite size and chemical composition of active materials change during conversion reactions[46,47,48] and these parameters influence the reaction potentials.

The rate performance of the 3D Ni/NiSb/Sb_2O_3 electrode was evaluated by cycling it at different current densities (Figure 5.5e). It should be noted that Na's larger mass (3 times) and ionic radius (45% larger) relative to Li leads to slower ionic diffusion, resulting in the rate performance of SIB electrodes being generally reduced relative to LIB electrodes.[49] I observed specific capacities of 487, 450, 413, 368, and 326 mA h g^{-1} (electrode basis volumetric capacities of 459, 424, 390, 347, and 307 mA h cm^{-3}) at 200, 400, 800, 1600 and 3200 mA g^{-1}, respectively. Even at 6400 mA g^{-1}, the electrode still delivered 288 mA h g^{-1} (electrode basis volumetric capacity of 271 mA h cm^{-3}). When the rate returned from 6400 to 200 mA g^{-1}, the specific capacity recovered to 477 mA h g^{-1} (electrode basis volumetric capacity of 449 mA h cm^{-3}). Figure 5.9 compares the specific capacity of this work with previous Sb_2O_3 systems as a function of the current density. As Figure 5.9 shows, the 3D Ni/NiSb/Sb_2O_3 electrode exhibited a similar

rate performance as other reports. Although some of the other reports indicated a better rate performance in terms of specific capacity, the results are particularly notable considering the high loading and high volumetric capacity of our design (volumetric capacities are not generally provided in the other reports, although from reviewing the images and experimental procedures in the other reports, it appears the volumetric capacities are generally low). The good rate performance at high loading presented here can be attributed to the 3D bicontinuous structure of the electrode, which improves the reaction kinetics by providing short solid-state ion diffusion lengths, the large electrode surface area and the high electrical conductivity of the scaffold.[31,32,34]

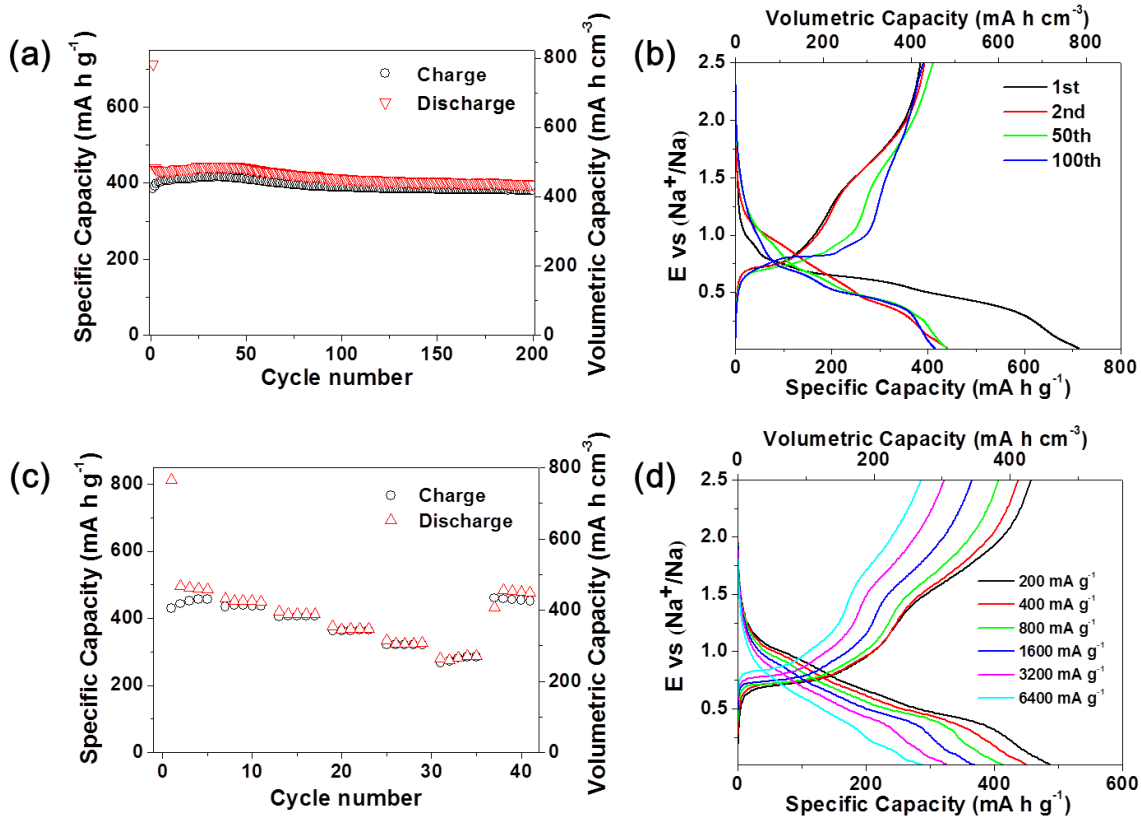

Figure 5.5 (a) Cycling performance of 3D Ni@NiSb/Sb_2O_3 (1.1 g cm^{-3} loading) at 200 mA g^{-1}. (b) 1st, 2nd, 10th, 50th and 100th cycle discharge-charge curves of a 3D Ni@NiSb/Sb_2O_3 at 200 mA g^{-1}. (c) Rate performance of a 3D Ni@NiSb/Sb_2O_3 (1.1 g cm^{-3} loading) at 200 to 6400 mA g^{-1}. (d) Discharge−charge voltage curves at indicated current densities.

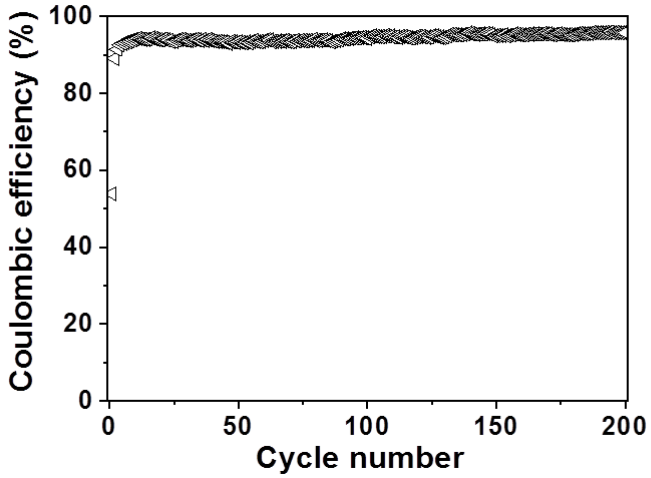

Figure 5.6 Coulombic efficiency of a 3D Ni@NiSb/Sb_2O_3 electrode presented in Fig 5.5a.

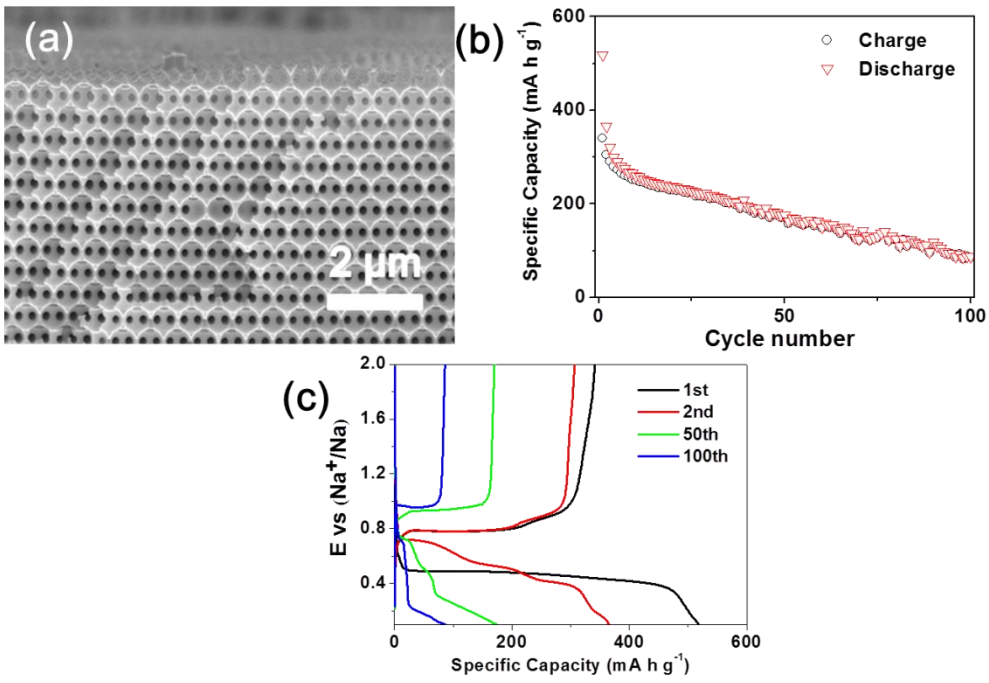

Figure 5.7 (a) Cross-sectional SEM image of a 3D Sb inverse opal, (b) Cycling performance of a 3D Sb electrode at 200 mA g^{-1} and (c) 1st, 2nd, 50th and 100th cycle discharge-charge curves of a 3D Sb at 200 mA g^{-1}.

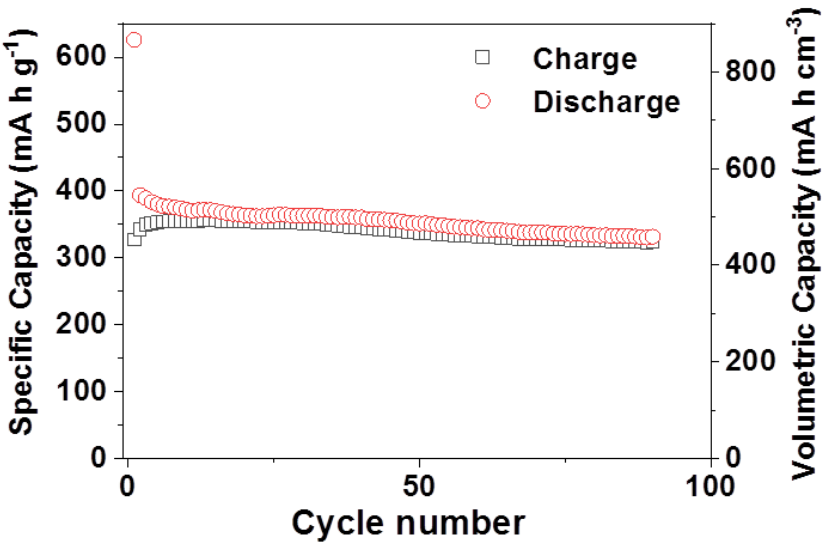

Figure 5.8 Cycling performance of 3D Ni@NiSb/Sb_2O_3 with higher loading (1.26 g cm^{-3}) at 200 mA g^{-1}

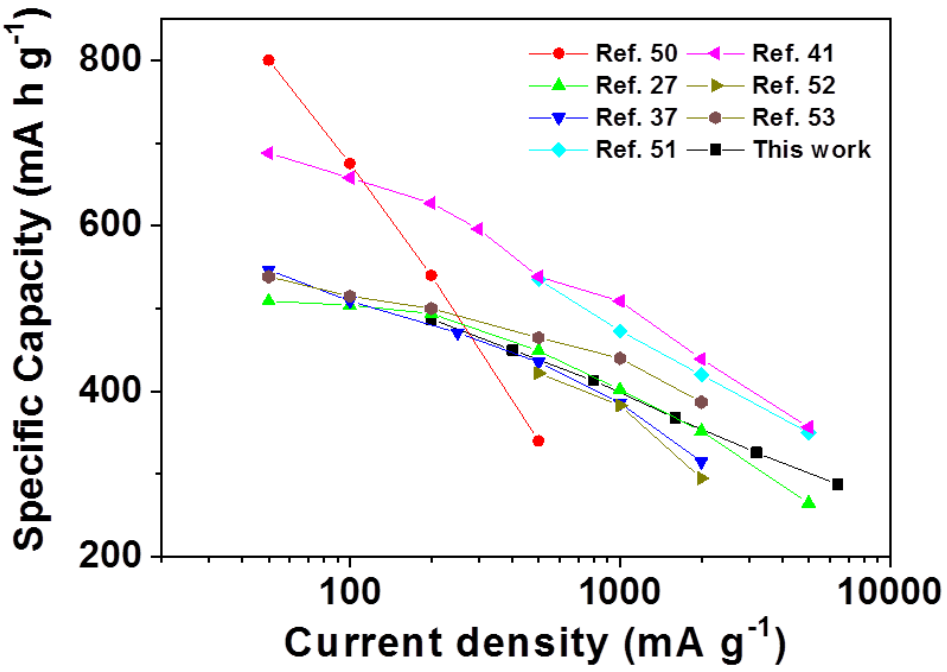

Figure 5.9 A comparison of the rate performance of current work with other previous Sb_2O_3 works.[27,37,41,50-53]

The electrode microstructure during cycling was examined by SEM (Figure 5.10). A single sample was prepared and cut into two pieces, one of which was imaged in the discharged state, and the other in the charged state. The sodiated (discharged) electrode appears denser and the interconnected pore size smaller due to volume expansion of the active material. The overall electrode structure remained constant during cycling and no damage to the 3D Ni scaffold was observed, indicating the 3D metal scaffold effectively accommodated the volume expansion. The volume expansion during discharge appears significantly less than 300 %, perhaps because the Sb_2O_3 is not fully sodiated, as reflected in the capacity and as discussed in the following paragraph, the NiSb formed during annealing was electrochemically inactive during cycling.

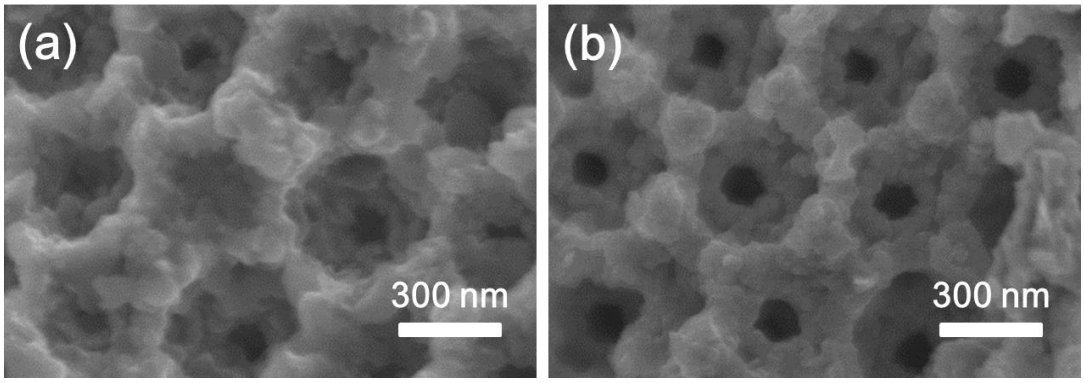

Figure 5.10 Cross-sectional SEM images of 3D Ni@NiSb/Sb_2O_3 (1.1 g cm^{-3} loading) after (a) sodiation and (b) desodiation.

Ex situ XRD was performed on electrodes cycled to different states of charge (discharged to 0.01 V, and charged to 1.2 and 2.5 V) to better understand the reaction chemistry of the 3D Ni/NiSb/Sb_2O_3 electrode (Figure 5.11). Sb_2O_3 peaks disappeared after the electrode was discharged to 0.01 V. No new peaks appeared even after charging to 2.5 V, indicating the discharge product is amorphous and the active material crystallinity is not recovered during charging. The NiSb peak was unchanged during cycling, indicating NiSb is electrochemically inactive in this system. As an admittedly not fully conclusive experiment, to potentially investigate the effect of NiSb, the as-deposited 3D electrode before heat treatment was cycled at 200 mA g^{-1}. The specific capacity decayed rapidly, indicating the inactive NiSb may be an important contribution to the improved cyclability of the annealed 3D electrodes (Figure 5.12). While I cannot rule out other possibilities for the improved cyclability, such as annealing driving

off trace water, I think I can rule out that the annealing induced crystallinity is important to the cyclability, since even the electrodes after heat treatment become amorphous after the 1st discharge. One possibility is that NiSb enhances the adhesion between active materials and Ni current collector by forming an alloy at this interface which inhibits electrical disconnection of the active materials from the 3D Ni current collector.

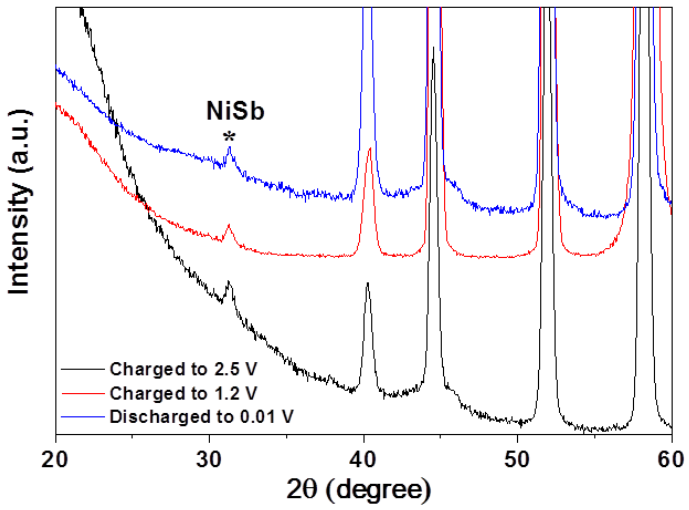

Figure 5.11 XRD pattern of 3D Ni@NiSb/Sb_2O_3 electrode discharged to 0.01 V, and charged to 1.2 and 2.5 V

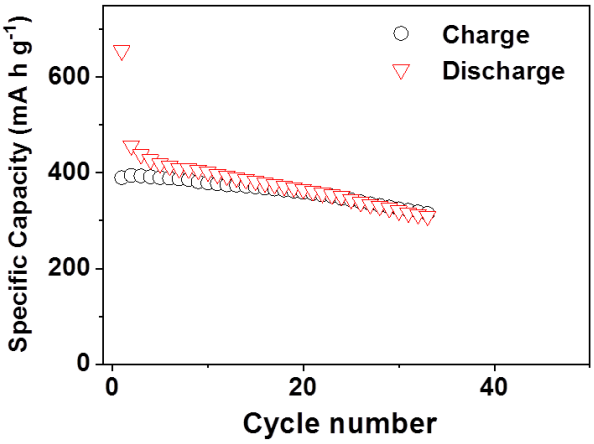

Figure 5.12 Cycling performance of as-deposited 3D electrodes at 200 mA g^{-1} (1.1 g cm^{-3} loading)

5.3 Conclusions

In conclusion, high gravimetric and volumetric capacity 3D Ni/NiSb/Sb_2O_3 electrodes were fabricated by electrodeposition of what is probably an amorphous mixture of Sb and Sb_2O_3 on a Ni scaffold followed by a heat treatment in air. The 3D Ni/NiSb/Sb_2O_3 electrodes exhibited attractive specific and electrode basis volumetric capacities of ~445 mA h g^{-1} and ~488 mA h cm^{-3} in conjunction with an excellent cycling performance of 89 % capacity retention over 200 cycles at a current density of 200 mA g^{-1}. The effect of active materials loading in the porous 3D scaffold was investigated to determine a loading which provided a high gravimetric and volumetric capacity. I suggest the enhanced cyclability can be attributed to the 3D Ni scaffold which accommodates volume changes curing cycling and provides a conductive pathway, and a NiSb alloy formed between the current collector and active materials which improves the adhesion of the active material to the scaffold. In addition to reporting advancements in a specific promising Na-ion anode chemistry, I believe this work proposes a useful guideline on how to design electrode structures for conversion and alloying SIB electrode materials.

5.4 Experimental section

Sample preparation: A tungsten substrate (Sigma-Aldrich) was rinsed with acetone, ethanol and millipore water, and dried. A PS suspension (0.2 wt %) was prepared by dispersing 600 nm diameter PS spheres (Molecular Probes) in millipore water. The tungsten substrate was vertically placed into vials filled with the PS suspension solution at 55 ℃ overnight. The substrate was taken out from the vials before the solution completely dried and subsequently annealed at 97 ℃ for 3 h to strengthen the adhesion between PS spheres and to increase the interconnected pore size between the PS spheres. A 3D Ni scaffold was made by Ni electrodeposition through a PS colloidal template by applying -1.5 mA cm^{-2} in a commercial Ni plating solution (Techni Nickel S, Technic Corp.) with the PS opal on tungsten substrate as the working electrode and a nickel substrate as the counter electrode. After Ni deposition, the sample was soaked in toluene to dissolve the PS template, resulting in the Ni inverse opal. The final electrode thickness was typically about 6 μm. Amorphous Sb/Sb_2O_3 was electrodeposited on the Ni inverse opal by pulsed-voltage electrodeposition in a 0.1 M $K_2Sb_2(C_4H_2O_6)_2$ (Sigma-Aldrich, 99 %) solution. A platinum foil and a Ag/AgCl reference electrode (BASi Inc.) were used as the

counter and reference electrodes, respectively. The voltage profile applied consists of -2 V vs Ag/AgCl for 0.25 s and a rest for 60 s. The amount of material deposited was controlled by the number of pulses applied (to generate a loading of 1.1 g cm^{-3} on a typical scaffold, 90 pulses were required). Following electrodeposition, the electrode was washed with Millipore water and ethanol and annealed in air at 300 ℃ for 1h. A 3D scaffold-free pure Sb electrode was prepared by electrodeposition through constant voltage method. Electrodeposition of Sb was conducted by applying constant voltage of -0.4 V vs Ag/AgCl in 0.2 M $SbCl_3$ in isopropyl alcohol solution with a PS opal grown tungsten substrate as a working electrode and a platinum substrate as a counter electrode. The PS template was removed in the same way as above.

Characterization: Sample morphologies were investigated using a Hitachi S-4800 SEM. EDS was performed using a Hitachi S-4700 SEM equipped with an Oxford INCA energy-dispersive X-ray analyzer. The crystal structures were confirmed by a Philips X'pert MRD XRD using Cu Kα radiation (λ = 0.15418 nm). For the ex situ XRD analysis after cycling, electrodes were washed with DMC multiple times and dried in the glove box prior to analysis. The electrodes were sealed with Kapton tape (SPEX, 8μm thickness) in the glove box to prevent air exposure. The mass of deposited materials was determined by a microbalance with an accuracy of 1 μg (XP26, METTLER TOLEDO) before and after heat treatment. TGA analysis was performed using a Q50-TGA (TA Instruments) in air. The heating rate to 300 ℃ was 5 ℃ min-1 and the hold time at 300 ℃ was 1h. For postmortem SEM analysis after cycling, electrodes were washed with DMC multiple times and dried in the glove box prior to analysis.

Electrochemical Measurements: 1 M $NaClO_4$ in PC containing 5 wt % FEC was used as electrolyte. Sodium metal (Na, Sigma Aldrich) was used as the counter electrode for Swagelok-type two-electrode cells and glass microfiber filter (Whatman, GF/F) was used as a separator. All cells were assembled in the glove box under an argon atmosphere. Galvanostatic discharge/charge tests were conducted using a VMP3, Bio-Logic potentiostat over a voltage range of 0.01 to 2.5 V vs. Na/Na^+ at room temperature. Current densities are calculated based on the total mass of deposited materials.

5.5 References

[1] H. Kim, H. Kim, Z. Ding, M. H. Lee, K. Lim, G. Yoon, K. Kang, *Adv. Energy Mater.* **2016**, *6*, 1600943.

[2] S. W. Kim, D. H. Seo, X. Ma, G. Ceder, K. Kang, *Adv. Energy Mater.* **2012**, *2*, 710.

[3] M. D. Slater, D. Kim, E. Lee, C. S. Johnson, *Adv. Funct. Mater.* **2013**, *23*, 947.

[4] X. Ma , H. Chen , G. Ceder, *J. Electrochem. Soc.* **2011**, *158*, A1307.

[5] D. A. Stevens, J. R. Dahn, *J. Electrochem. Soc.* **2000**, *147*, 1271.

[6] H. Hou, C. E. Banks, M. Jing, Y. Zhang, X. Ji, *Adv. Mater.* **2015**, *27*, 7861.

[7] W. Li, M. Zhou, H. Li, K. Wang, S. Cheng, K. Jiang, *Energy Environ. Sci.* **2015**, *8*, 2916.

[8] J. Ding, H. Wang, Z. Li, A. Kohandehghan, K. Cui, Z. Wu, B. Zahiri, X. Tan, E. M. Lotfabad. B. C. Olsen, D. Mitlin, *ACS Nano* **2013**, *7*, 11004.

[9] K. Kubota, S. Komaba, *J. Electrochem. Soc.* **2015**, *162*, A2538.

[10] M. He, K. Kravchyk, M. Walter, M. V. Kovalenko, *Nano Lett.* **2014**, *14*, 1255.

[11] S. Liu, J. Feng, X. Bian, J. Liu, H. Xu, *Energy Environ. Sci.* **2016**, *9*, 1229.

[12] J. Liu, L. Yu, C. Wu, Y. Wen, K. Yin, F.-K. Chiang, R. Hu, J. Liu, L. Sun, L. Gu, *Nano Lett.* **2017**, *17*, 2034.

[13] Y. Zhu, X. Han, Y. Xu, Y. Liu, S. Zheng, K. Xu, L. Hu, C. Wang, *ACS Nano* **2013**, *7*, 6378.

[14] N. Yabuuchi, K. Kubota, M. Dahbi, S. Komaba, *Chem. Rev.* **2014**, *114*, 11636.

[15] L. Baggetto, P. Ganesh, C.-N. Sun, R. A. Meisner, T. A. Zawodzinski, G. M. Veith, *J. Mater. Chem. A* **2013**, *1*, 7985.

[16] J. Liu, N. Li, M. D. Goodman, H. G. Zhang, E. S. Epstein, B. Huang, Z. Pan, J. Kim, J. H. Choi, X. Huang, *ACS Nano* **2015**, *9*, 1985.

[17] M. S. Park, G. X. Wang, Y. M. Kang, D. Wexler, S. X. Dou, H. K. Liu, *Angew. Chem., Int. Ed.* **2007**, *46*, 750.

[18] T. Song, J. Xia, J.-H. Lee, D. H. Lee, M.-S. Kwon, J.-M. Choi, J. Wu, S. K. Doo, H. Chang, W. I. Park, *Nano Lett.* **2010**, *10*, 1710.

[19] L.-F. Cui, Y. Yang, C.-M. Hsu, Y. Cui, *Nano Lett.* **2009**, *9*, 3370.

[20] G. Derrien, J. Hassoun, S. Panero, B. Scrosati, *Adv. Mater*. **2007**, *19*, 2336.

[21] Y. Liu, N. Zhang, L. Jiao, J. Chen, *Adv. Mater.* **2015**, *27*, 6702.

[22] M. D. Goodman, S. Kim, N. Tatsuda, K. Yano, P. V. Braun, *Part. Part. Syst. Charact.* **2015**, *32*, 928.

[23] J. Liu, X. Chen, J. Kim, Q. Zheng, H. Ning, P. Sun, X. Huang, J. Liu, J. Niu, P. V. Braun, *Nano Lett.* **2016**, *16*, 4501.

[24] A. L. Michan, G. Divitini, A. J. Pell, M. Leskes, C. Ducati, C. P. Grey, *J. Am. Chem. Soc.* **2016**, *138*, 7918.

[25] X. H. Liu, L. Zhong, S. Huang, S. X. Mao, T. Zhu, J. Y. Huang, *ACS Nano* **2012**, *6*, 1522.

[26] K.-S. Hong, D.-H. Nam, S.-J. Lim, D. Sohn, T.-H. Kim, H. Kwon, *ACS Appl. Mater. Interfaces* **2015**, *7*, 17264.

[27] M. Hu, Y. Jiang, W. Sun, H. Wang, C. Jin, M. Yan, *ACS Appl. Mater. Interfaces* **2014**, *6*, 19449.

[28] N. Li, S. Liao, Y. Sun, H. Song, C. Wang, *J. Mater. Chem. A* **2015**, *3*, 5820.

[29] M. Valvo, F. Lindgren, U. Lafont, F. Björefors, K. Edström, *J. Power Sources* **2014**, *245*, 967.

[30] L. Wu, X. Hu, J. Qian, F. Pei, F. Wu, R. Mao, X. Ai, H. Yang, Y. Cao, *J. Mater. Chem. A* **2013**, *1*, 7181.

[31] H. Zhang, T. Shi, D. J. Wetzel, R. G. Nuzzo, P. V. Braun, *Adv. Mater.* **2016**, *28*, 742.

[32] S. Kim, J. Liu, K. Sun, J. Wang, S. J. Dillon, P. V. Braun, *Adv. Funct. Mater.* **2017**, *27*, 1702783.

[33] J. Liu, Q. Zheng, M. D. Goodman, H. Zhu, J. Kim, N. A. Krueger, H. Ning, X. Huang, J. Liu, M. Terrones, P. V. Braun, *Adv.Mater.* **2016**, *28*, 7696.

[34] H. Zhang, X. Yu, P. V. Braun, *Nat. Nanotechnol.* **2011**, *6*, 277.

[35] H. Bryngelsson, J. Eskhult, L. Nyholm, M. Herranen, O. Alm, K. Edström, *Chem. Mater.* **2007**, *19*, 1170.

[36] D. H. Nam, K. S. Hong, S. J. Lim, M. J. Kim, H. S. Kwon, *Small* **2015**, *11*, 2885.

[37] D. Li, D. Yan, J. Ma, W. Qin, X. Zhang, T. Lu, L. Pan, *Ceram. Int.* **2016**, *42*, 15634.

[38] Y. Wang, Y. Jin, C. Zhao, Y. Duan, X. He, M. Jia, *Mater. Lett.* **2017**, *191*, 169.

[39] A. Darwiche, C. Marino, M. T. Sougrati, B. Fraisse, L. Stievano, L. Monconduit, *J. Am. Chem. Soc.* **2012**, *134*, 20805.

[40] J. Qian, Y. Chen, L. Wu, Y. Cao, X. Ai, H. Yang, *Chem. Commun.* **2012**, *48*, 7070.

[41] J. Zhou, B. Yan, J. Yang, Y. Yang, W. Zhou, H. Lan, H. Wang, L. Guo, *Nanoscale* **2018**, *10*, 9108.

[42] M.-Z. Xue, Z.-W. Fu, *Electrochem. Commun.* **2006**, *8*, 1250.

[43] X. Zhou, Z. Dai, J. Bao, Y.-G. Guo, *J. Mater. Chem. A* **2013**, *1*, 13727.

[44] X. Zhou, X. Liu, Y. Xu, Y. Liu, Z. Dai, J. Bao, *J. Phys. Chem. C* **2014**, *118*, 23527.

[45] J. Pan, N. Wang, Y. Zhou, X. Yang, W. Zhou, Y. Qian, J. Yang, *Nano Res.* **2017**, *10*, 1794.

[46] F. Wang, H.-C. Yu, M.-H. Chen, L. Wu, N. Pereira, K. Thornton, A. Van der Ven, Y. Zhu, G. G. Amatucci, J. Graetz, *Nat. Commun.* **2012**, *3*, 1201.

[47] L. S. Li, F. Meng, S. Jin, *Nano Lett.* **2012**, *12*, 6030.

[48] U. Boesenberg, M. A. Marcus, A. K. Shukla, T. Yi, E. McDermott, P. F. Teh, M. Srinivasan, A. Moewes, J. Cabana, *Sci. Rep.* **2015**, *4*, 7133.

[49] J. Qian, M. Zhou, Y. Cao, X. Ai, H. Yang, *Adv. Energy Mater.* **2012**, *2*, 410.

[50] J. Fei, Y. Cui, J. Li, Z. Xu, J. Yang, R. Wang, Y. Cheng, J. Hang, *Chem. Commun.* **2017**, *53*, 13165.

[51] S. Liu, Z. Cai, J. Zhou, M. Zhu, A. Pan, S. Liang, *J. Mater. Chem. A* **2017**, *5*, 9169.

[52] X. Guo, X. Xie, S. Choi, Y. Zhao, H. Liu, C. Wang, S. Chang, G. Wang, *J. Mater. Chem. A* **2017**, *5*, 12445.

[53] L. Yang, Y. Huang, X. Li, J. Sheng, F. Li, Z. Xie, Z. Zhou, *ChemElectroChem* **2018**, *5*, 2522.

CHAPTER 6
REVERSIBLE CONVERSION REACTIONS AND SMALL FIRST CYCLE IRREVERSIBLE CAPACITY LOSS IN METAL SULFIDE-BASED ELECTRODES ENABLED BY SOLID ELECTROLYTES

6.1 Introduction

Solid electrolytes have received considerable attention for LIBs due to their potential safety, cycle life, and energy density advantages over liquid electrolytes.[1-5] For example, solid electrolytes may prevent cycling-induced problems associated with liquid electrolytes including electrode dissolution, lithium dendrite formation and loss of electrical contact to active materials (however, a number of these potential benefits have yet to be observed in practice).[1-5] One area I find particularly intriguing is the possibly for solid electrolytes to enable electrode materials with good theoretical energy densities, which to date have only exhibited poor electrochemical performance in liquid cells. As an example, $LiNi_{0.5}Mn_{1.5}O_4$ performs better when used with a solid electrolyte than with a liquid electrolyte since the solid electrolyte prevents Mn ions dissolution into the electrolyte during cycling.[6] The Li-S system is another chemistry where solid-state designs have been investigated due to the potential of a solid electrolyte to eliminate polysulfide shuttling.[7-9] A bit surprisingly, solid-state designs have even been demonstrated for electrode materials which undergo large volume changes during cycling. When a Si anode was tested in a solid-state cell with a boron-doped lithium phosphorus oxynitride (LiPONB) solid electrolyte, very little capacity decay was observed even to 1500 cycles.[10] Apparently, the solid electrolyte suppressed the formation of cracks in the Si anode.

I was interested in exploring anodes based on binary metal sulfides (M_xS_y with M = Sn, Sb, Pb, Bi) because these systems have high theoretical capacities through conversion followed by alloying reaction,[11-18] yet much lower practical capacities in common liquid electrolytes. The much lower than theoretical capacities is because the conversion reaction has been found to be irreversible, resulting in a large irreversible capacity after the first cycle.[13,16] Here I focus on SnS because it has the highest theoretical capacity among these metal sulfides, and Sn is both relatively abundant and nontoxic.[13-18] Charge storage during electrochemical reactions with lithium are due to the following reactions:

(1) $SnS + 2Li \leftrightarrow Sn + Li_2S$ (Conversion), 0.9 to 2.2 V vs. Li, specific capacity = 356 mA h g^{-1}

(2) $Sn + 4.4Li \leftrightarrow Li_{4.4}Sn$ (Alloying) 0.01 to 0.9 V vs. Li, specific capacity = 782 mA h g^{-1}

A large irreversible capacity is unfavorable because it consumes Li, and thus requires a pre-lithiation step prior to cell assembly, and substantially lowers the usable energy density of the electrode. Our hypothesis is that the large irreversible capacity exhibited by SnS is due to undesirable interactions between the SnS and liquid electrolytes, which I test by building a solid-state cell consisting of SnS nanocrystals embedded in a sulfide based glass electrolyte. Using this cell we demonstrate a solid-state design enables a reversible conversion reaction of SnS and provides a stable cycling performance. In particular, the first cycle irreversible capacity loss is significantly lower in the solid-state design (8.2%), relative to an otherwise quite similar liquid electrolyte-based design (44.6%).

6.2 Results and discussion

Nearly monodisperse, ~500 nm on a side, tetrahedral ZB SnS nanocrystals were synthesized by a wet chemical method (see experimental section) (Figure 6.1b and 6.1c). The well-defined morphology and crystal structure was achieved by controlling the Sn and S precursor ratio, reaction time and temperature. The SnS ZB crystal structure was confirmed by XRD (Figure 6.1d), with the expected (111), (200) and (220) peaks at 26.5°, 30.7°, and 44.0°, respectively and 0.8 nm lattice fringes corresponding to the (110) d-spacing observed in HRTEM (Figure 6.1e). EDS indicated the Sn:S atomic ratio is close to 1:1, and no other elements were observed in significant concentration (Figure 6.2).

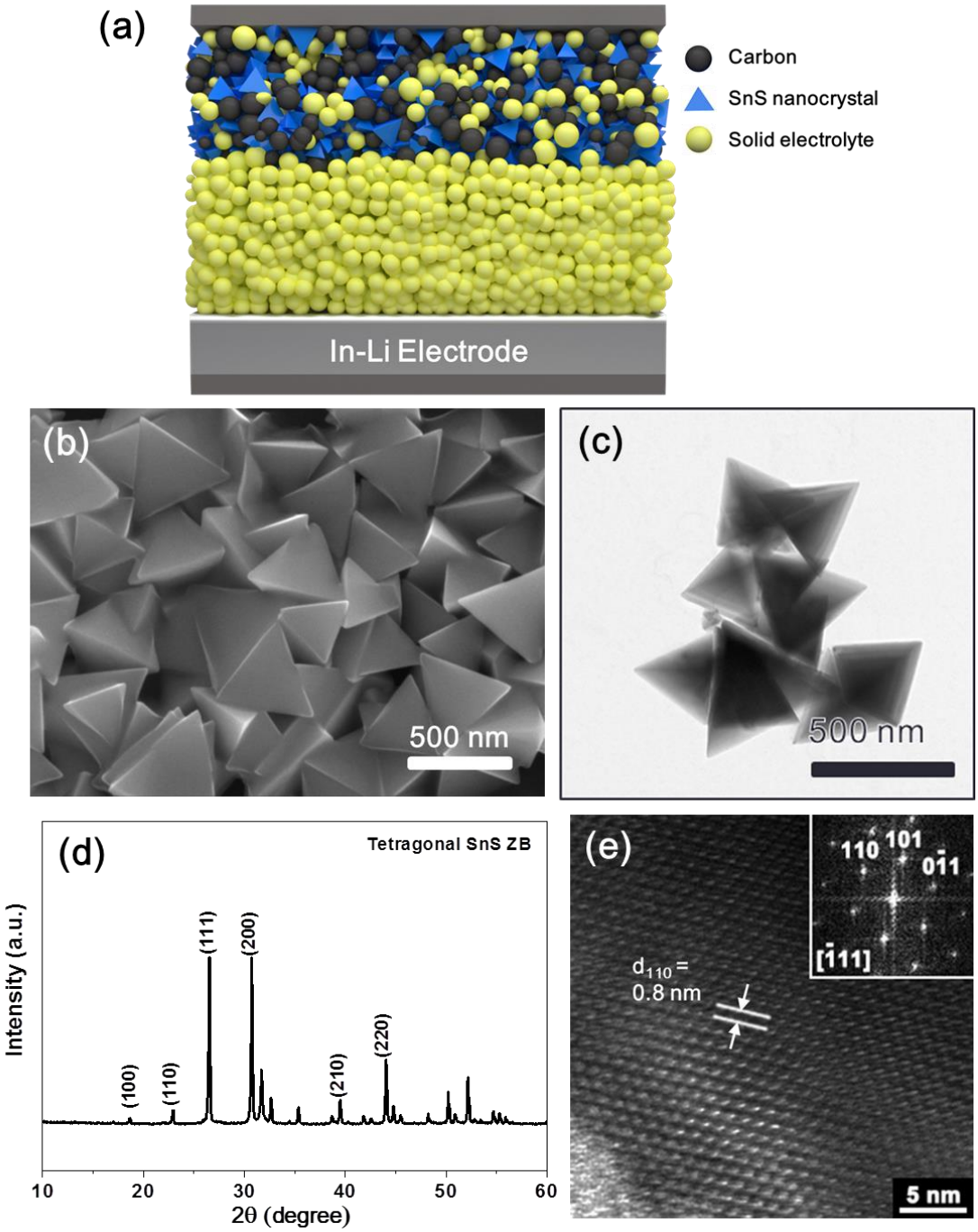

Figure 6.1 (a) Schematic of the all-solid-state battery design. (b) SEM and (c) TEM images of ZB SnS nanocrystals. (d) XRD of ZB SnS nanoparticles. (e) High resolution TEM image of ZB SnS nanocrystals and corresponding SAED pattern (inset).

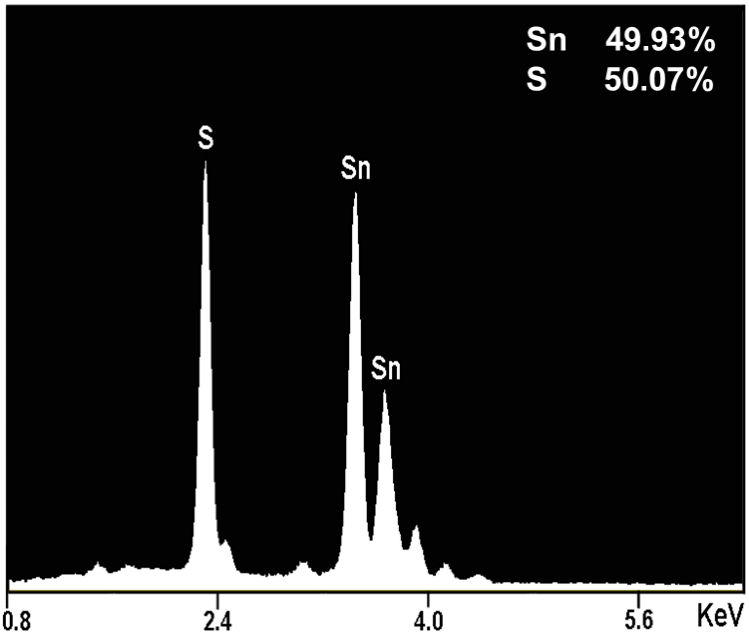

Figure 6.2 EDS spectrum of ZB SnS nanocyrstals.

The electrochemical properties of the SnS nanocrystals were tested by galvanostatic discharge/charge tests in both solid-state and liquid cells at 22 °C (note, I also tested commercial SnS powders, consisting of much larger sized primary particles, however their specific capacity was quite low (Figure 6.3). I tested commercial SnS powders consisting of much larger primary particle sizes in a solid-state cell by galvanostatic discharge/charge at room temperature as a preliminary experiment in advance. While I observed a stable cycling performance, the specific capacity using this system was low, ~400 mA g h^{-1}, indicating a nanosized active material and close contact between the active material and the solid electrolyte is necessary for obtaining a good cycling performance, perhaps because a large interfacial area is required between the solid electrolyte and the active material to obtain a good capacity and rate performance. Figure 6.4a shows the cycling performance of the SnS nanocrystals at 50 mA g^{-1} in both these cell designs. First discharge capacities of 802 (solid-state) and 1123 mA h g^{-1} (liquid cell) were observed. Although the liquid cell shows a higher first discharge capacity, its second cycle discharge capacity is only 635 mA h g^{-1} (irreversible capacity of 43.4%, 488 mA h g^{-1}) while the second discharge capacity of solid-state cell is 735 mA h g^{-1} (irreversible capacity of 8.2%, 67 mA h g^{-1}). Also, the solid-state cell shows much more stable cycling than the liquid cell. The specific

capacity of the solid-state cell decreased slightly for the first 10 cycles, and stabilized at ~629 mA h g^{-1} (100 cycle value), corresponding to 85.6 % retention relative to its second cycle discharge capacity. In contrast, the specific capacity of the liquid cell decayed rapidly, dropping to 148 mA h g^{-1} after 50 cycles. The long-term stability of the solid-state cell was checked by cycling a cell to 1300 cycles at higher c-rate (Figure 6.5). The cell was cycled 5 times at 50 mA g^{-1} and subsequently cycled at 500 mA h g^{-1} for 1300 cycles. 1300th cycle capacity at this rate was 180 mA h g-1 which is 74% of the 100 cycle capacity at this rate.

To determine why the solid-state cell cycled considerably better than the liquid cell, the discharge-charge curves of SnS nanocrystal-based solid-state and liquid cells were compared (Figure 6.4c and 6.4e). In the first discharge, both cells showed a hump at around 1.3 V which is the reduction of SnS to Sn and Li_2S.[13,15-17,19,20] The voltage plateaus below 0.6 V observed in both the solid-state and liquid cells are indications of Sn and Li alloying reactions,[21-23] and in the first charge, a series of voltage plateaus were observed up to 0.7 V from both cells due to de-alloying reactions.[21-23] The solid-state cell then showed a voltage plateau at around 1.85 V which is missing in the liquid cell. This voltage plateau is reported as the reconversion reaction of Sn to SnS[13,15-17,19], implying the reconversion is not occurring in the liquid cell. The conversion reaction voltage plateau in the second discharge curve appeared at a higher reaction potential (1.45 V) compared to the plateau in the first discharge (1.25 V), probably because of decreased overpotential as a result of the reduced particle size due to the conversion reaction.[24] Corresponding dQ/dV curves were obtained by differentiating the charge/discharge voltage curves to investigate reaction peaks (Figure 6.4d and 6.4f). The solid-state cell still shows clear conversion and alloying redox peaks after 5 cycles. The liquid cell also shows alloying redox peaks over 5 cycles but conversion redox peaks are not observed except one conversion reduction peak in the first discharge. Even some alloying redox peaks from the liquid cells disappear with cycling, suggesting active material degradation. Thus, the better cycling performance of the solid-state cell can be attributed to suppressed active materials degradation which will be discussed later. I also speculate that physical confinement enabled by solid electrolyte can contribute to stable cycling performance. The lack of a reconversion reaction in the liquid cell, and its presence in the solid-state cell appears to be the primary reason for the large difference in the irreversible capacity of the two designs.

The rate performance of the SnS-based solid-state cell was evaluated by cycling the cell at different current densities (Figure 6.4b) at room temperature. Specific capacities of 735, 608, 540, 383 and 188 mA h g^{-1} (second discharge capacity at each current density) were achieved at 50, 100, 200, 500, and 1000 mA g^{-1}, respectively. When the rate returns to 50 mA g^{-1} from 2000 mA g^{-1}, the charge capacity recovered to 477 mA h g^{-1}. It is notable that conversion reaction plateau or redox peaks disappeared at c-rates greater than 500 mA g^{-1} (Figure 6.6a and 6.6b), indicating Sn in the SnS can react with lithium selectively without first going through a conversion reaction. This implies that the reaction kinetics of the conversion reaction is more sluggish than those of the alloying reaction and that the conversion reaction can be bypassed at high c-rate.

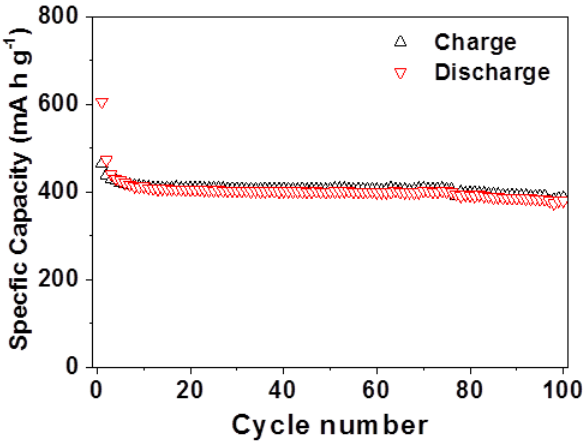

Figure 6.3 Cycling performance of Bulk SnS in a solid-state cell cycled at 50 mA h g^{-1} at room temperature.

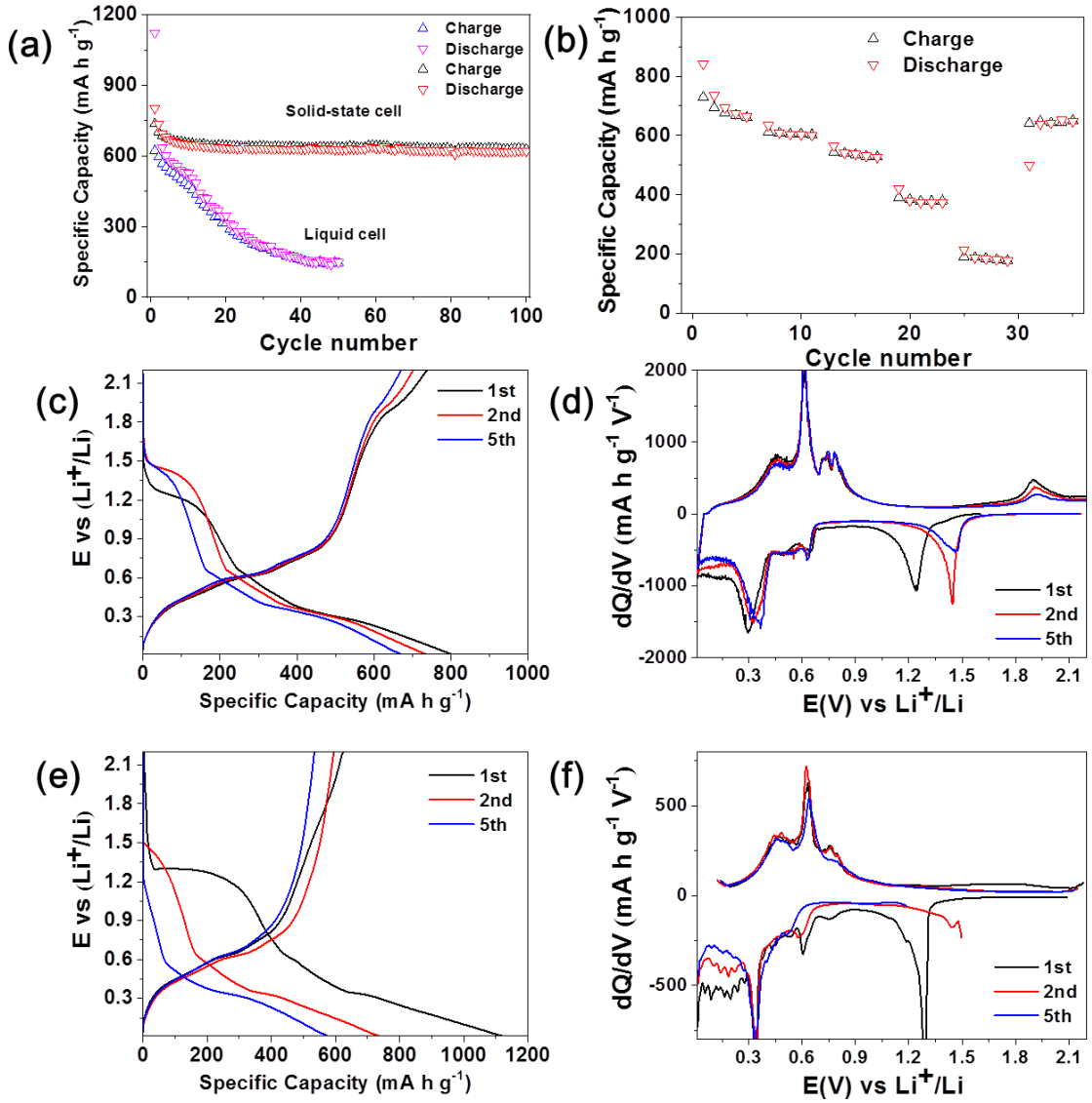

Figure 6.4 (a) Cycling performance of ZB SnS in a solid-state cell and conventional liquid cell cycled at 50 mA h g^{-1} at room temperature. (b) Rate performance of ZB SnS in a solid-state cell at different c-rates ranging from 50 mA g^{-1} to 1000 mA g^{-1} at room temperature. 1^{st}, 2^{nd} and 5^{th} cycle discharge-charge curves of ZB SnS in (c) a solid-state cell and (e) liquid cell from Fig 6.4a. Differential capacity plots for cycles presented in (d) Fig 6.4c and (f) Fig 6.4e.

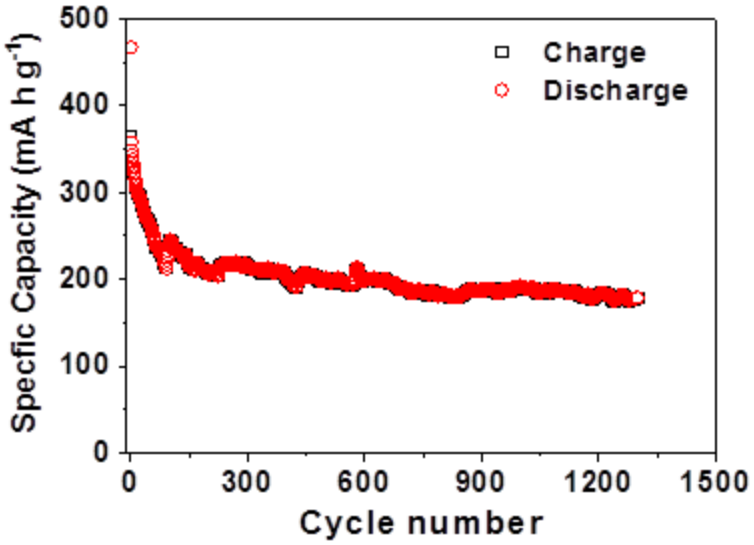

Figure 6.5 Cycling performance of ZB SnS in a solid-state cell cycled at 500 mA h g^{-1} at room temperature.

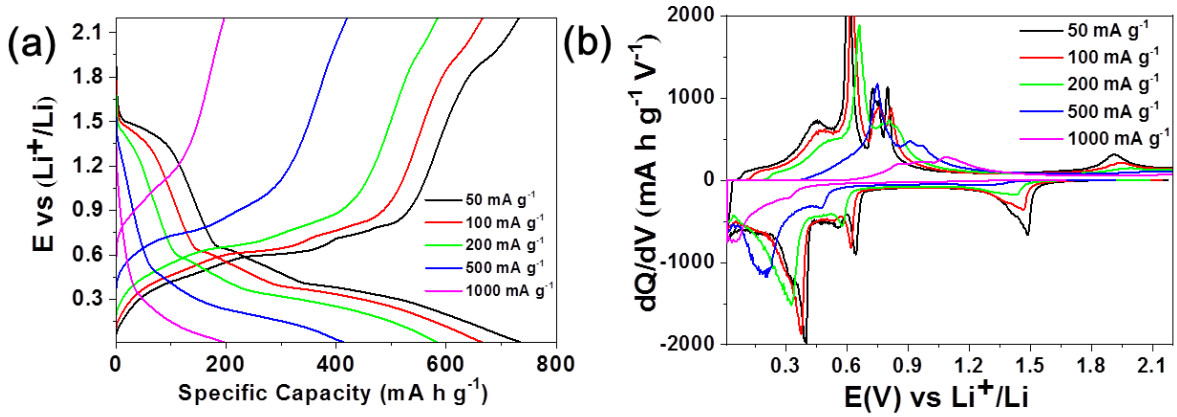

Figure 6.6 (a) Discharge/charge curves of ZB SnS in a solid-state cell cycled at different c-rates from Fig 6.4b. (b) Differential capacity plots for cycles presented in Fig 6.6a.

Cycling of the SnS-based solid-state cell was performed at 60 °C to examine if the reaction chemistry changes when the reaction kinetics and solid electrolyte ionic conductivities are greater (Figure 6.7a). At 60 °C the reaction voltages remained the same as at 22 °C (Figure 6.7b and 6.7c), indicating the reaction chemistry is not changing with operating temperature, while the voltage plateaus and dQdV peaks become more discrete. As others have indicated, this

is because the enhanced kinetics at higher temperatures allows reactions to occur closer to their thermodynamic potentials.[25] The solid-state cell at 60 °C exhibited first and second discharge capacities of 989 and 836 mA h g^{-1}, respectively (the second discharge specific capacity at 60 °C was 14 % greater than the second discharge specific capacity at 22 °C). We suspect the increased capacity at 60 °C is due to the higher ionic conductivity at 60 °C relative to at 22 °C. As determined by electrochemical impedance spectroscopy (EIS) the solid electrolyte ionic conductivity was 7.34×10^{-5} at 22 °C and 2.16×10^{-4} S cm^{-1} at 60 °C (Figure 6.8).

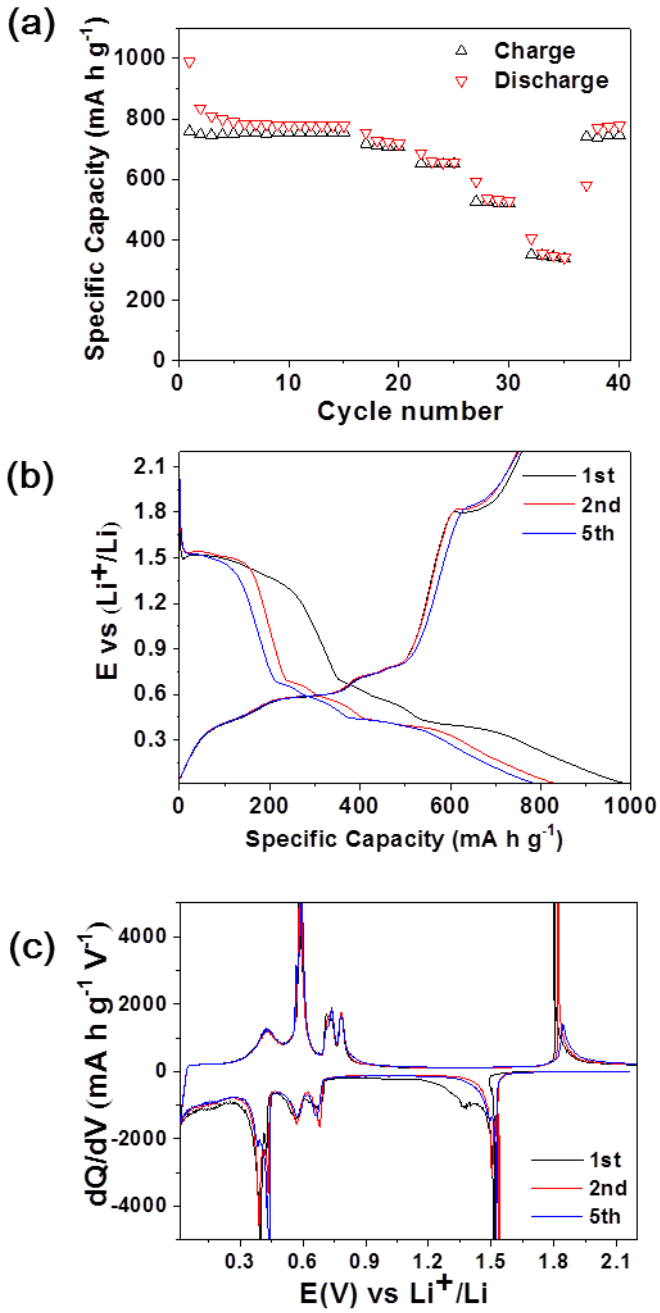

Figure 6.7 (a) Cycling and rate performance of ZB SnS in a solid-state cell cycled at 60 ℃. (b) 1st, 2nd and 5th cycle discharge-charge curves from Fig 6.7a. (c) Differential capacity plots for cycles presented in Fig 6.7b.

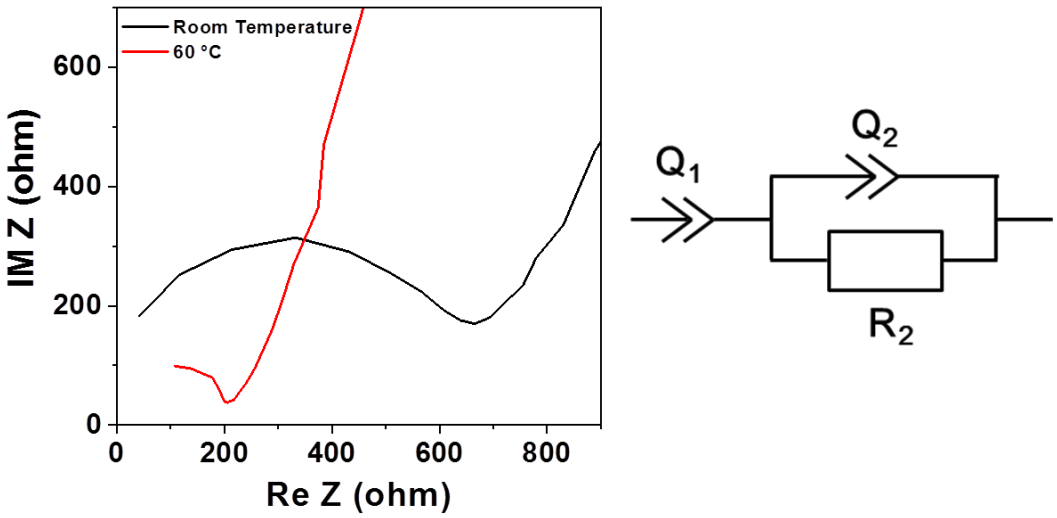

Figure 6.8 Nyquist plot of Li_2S-P_2S_5 solid electrolyte and its equivalent circuit.

To investigate the mechanism for the liquid cell SnS irreversible conversion reaction, XPS was performed on uncycled, 1 time and 10 times cycled electrodes in a liquid cell (Figure 6.9a). For the uncycled electrode, S 2p peaks at 161.1 and 162.3 eV characteristics of S^{2-} in SnS were observed. After 1 cycle, S 2p peaks at 160.6 and 161.6 eV, which correspond to S 2p3/2 and S 2p1/2 of Li_2S,[26,27], were observed, indicating SnS was not recovered after 1 cycle and Li_2S produced by discharging remained in the electrode. After 10 cycles, the S 2p intensity was very weak, indicating possible S loss by dissolution of Li_2S in the electrolyte. As further evidence of Li_2S dissolution, significant S was found on the Li counter-electrode after 5 cycles via EDS, presumably due to cross-over of dissolved Li_2S, while no Sn was observed (Figure 6.9b). Coin cell was assembled as usual and kept uncycled for 5 days. S was not found on the Li counter-electrode from uncycled cell via EDS indicating SnS is intact and insoluble in the liquid electrolyte. Based on the XPS and EDS data, I thus attribute the irreversible conversion reaction to the dissolution of Li_2S into carbonate based electrolyte.

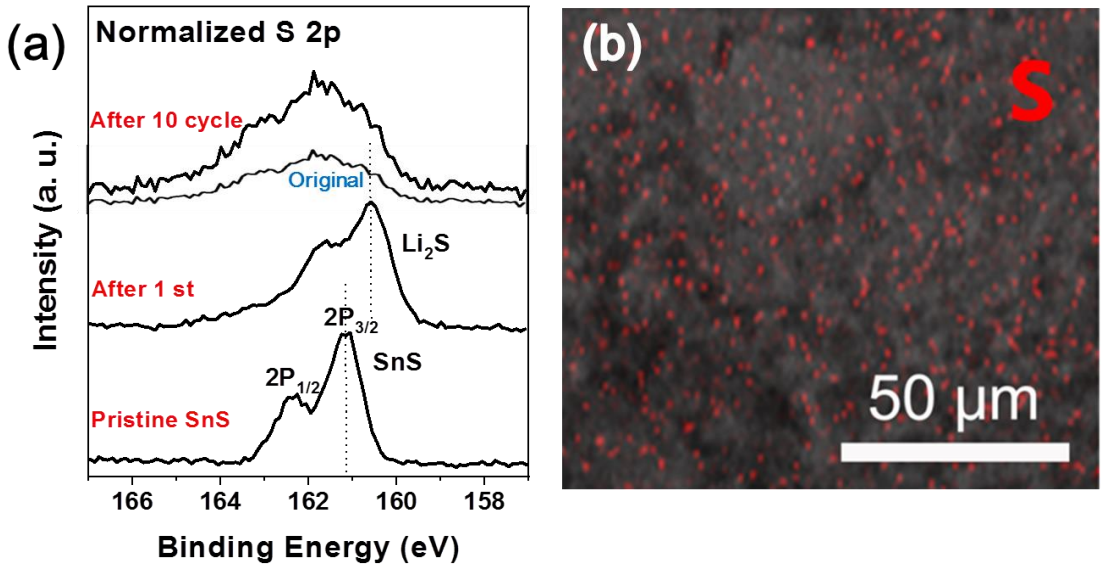

Figure 6.9 Postmortem analysis of a liquid cell. (a) Normalized XPS spectra of S 2p obtained from uncycled, 1 time and 10 times cycled ZB SnS electrodes in a liquid cell. XPS spectra normalized for comparison. (b) SEM image of a Li electrode after 5 cycles with EDS mapping of S overlay.

Another factor known to contribute to a large irreversible capacity is SEI formation. The liquid cell exhibits a first discharge capacity of 1123 mA h g^{-1} but some of this capacity may be due to SEI formation. CV was performed in a liquid cell using a $LiPF_6$ free electrolyte (EC:DMC, 1:1 v/v) to evaluate SEI formation (Figure 6.10a). CV was used rather than galvanostatic charge/discharge because there is no charge carrier in the electrolyte due to lack of salt. Substantial current flow was observed in the first cathodic scan including a broad peak at around 0.85 V. On the other hand, when cyclic voltammetry was performed in an In-Li ‖ Solid electrolyte ‖ Ti solid-state cell (Figure 6.10b), no significant current flow was observed in the cathodic scans indicating solid electrolyte is not electrochemically reduced. Specific cumulative charge during cyclic voltammetry in the liquid cell is shown in Figure 6.10c. In the liquid cell, the first cathodic scan showed a specific cumulative charge of about 240 mA h g^{-1} while subsequent scans showed below 100 mA h g^{-1} which decreased with cycling, indicating that SEI formation happens primarily in the first few discharge processes. From Figure 6.10c, I estimate about 20 % of first discharge capacity in the liquid cell originates from the SEI formation.

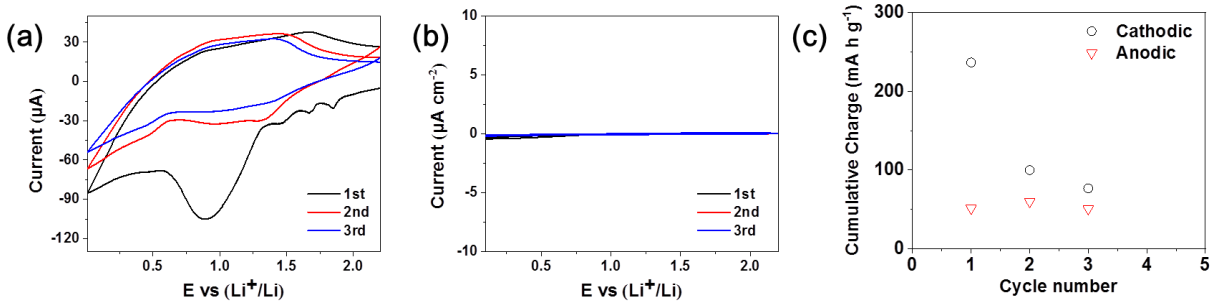

Figure 6.10 Cyclic voltammetry curves of (a) Li ‖ EC:DMC (1:1 v/v) ‖ SnS liquid cell and (b) In-Li ‖ Solid electrolyte ‖ Ti solid state cell at a scan rate of 0.1 mV s^{-1}. (c) Specific cumulative charge during cyclic voltammetry calculated from Fig 6.10a.

To investigate the reaction chemistry of SnS in the solid-state cells, in particular the conversion reactions, phase changes of SnS during cycling were examined by ex-situ XRD at different states of charge (Figure 6.11). The solid-state cells were disassembled after discharging/charging and electrodes were sealed with Kapton tape to protect them from air. SnS assembled in a solid-state cell shows the same diffraction pattern as SnS in powder form, indicating significant reactions with SnS do not occur during mixing with solid electrolyte and cell assembly. When the electrode was discharged to 0.8 V, SnS peaks disappeared and Li_2S and Sn peaks appeared. I suspect that this crystalline Li_2S is produced as the result of solid electrolyte decomposition after losing Li^+, and not from conversion reactions based on previous studies which suggested Li_2S-P_2S_5 solid electrolyte undergoes phase decomposition into Li_2S during cycling.[28,29] To evaluate this, as a control experiment a solid-state cell assembled using $Li_4Ti_5O_{12}$ was tested in the same way. After discharging to 1 V vs Li/Li^+, Li_2S was observed by XRD. Based on previous reports, I suspect the Li_2S formed by conversion reactions is amorphous,[30-32] and thus not observed by XRD. It is reported that Li_2S formed from solid electrolyte does not evolve further with cycling and is stable,[33] which agrees with the XRD data (the Li_2S peaks intensities were constant during the charging and discharging. The Sn diffraction peaks became weak in comparison to the Li_2S peaks upon charging to 0.45 V, indicating the consumption of crystalline Sn by lithiation. The diffraction peaks of Sn disappeared and one broad peak at around 22° and the other peak at 38° appeared after full discharge to 0.01 V. These new peaks are characteristic of a Li-Sn alloy and agree with previous

reports.[34,35] Many Li-Sn alloy phases (e.g., Li_5Sn_2, $Li_{13}Sn_5$, Li_7Sn_2, $Li_{22}Sn_5$, and $Li_{17}Sn_4$) have very similar XRD patterns so the Li-Sn alloy phase was not determined.[35] Rather, the stoichiometry of Li and Sn was estimated as $Li_{2.8}Sn$ based on a calculation from the capacity delivered over the voltage range of 0.7-0.01 V (634 mA h g^{-1}). When the electrode was charged to 0.66 V, Li-Sn alloy peaks disappeared and Sn peaks reappeared, demonstrating the reversibility of the alloying reaction. The Sn peaks intensities decreased and no additional peaks were observed after further charging to 1.32 V. After fully charged to 2.2 V, the intensity of Sn peaks decreased significantly, suggesting reconversion of Sn and Li_2S to SnS. However, SnS peaks were not observed in the fully charged state, indicating reconstructed SnS is either amorphous or nanocrystalline.

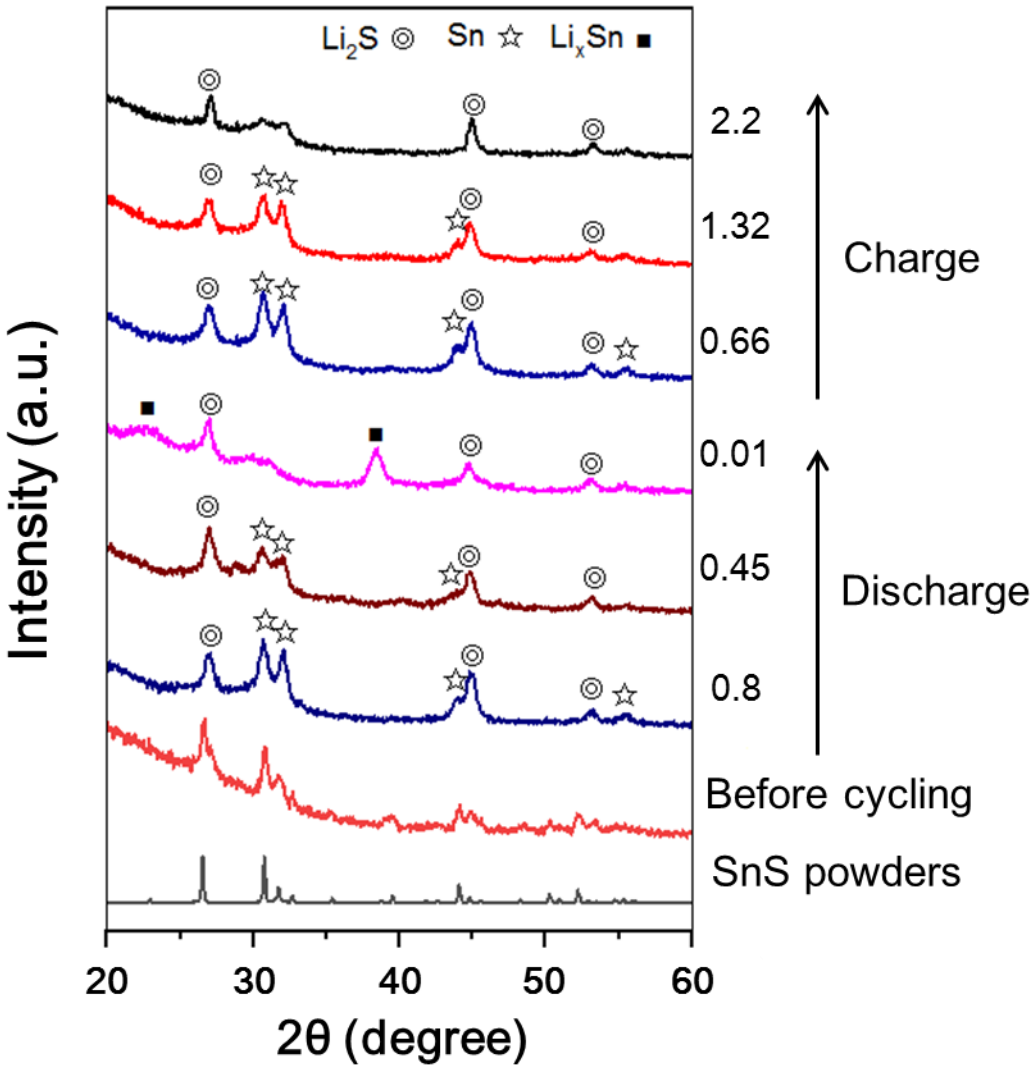

Figure 6.11 Ex situ XRD spectra of SnS in solid-state cells at different states of charges.

To gain further understanding of the reaction chemistry of SnS in a solid-state cell, XAS was utilized. Ex-situ XAS analysis was performed using the same samples used for the XRD measurements. Figure 6.12a and 6.12b show the Sn K-edge XANES spectra at different charge states during the first discharging and charging. For comparison, the XANES spectra of the Sn metal foil is also included. In all spectra, the strong main absorption peak originates from the transition from the Sn 1s state to the unoccupied 5p states.

When the SnS electrode was discharged to 0.8 V (Figure 6.12a), the peak height decreased and reached an intensity comparable to that of the Sn reference foil, which reflects the reduction of Sn and formation of a metallic phase, in agreement with XRD. The peak height

further decreased upon discharge to 0.45V. In the fully discharged state, the Sn peak position shifted 3.8 eV toward higher energy, indicating the oxidation state of Sn is negative and that of Li is positive. This is probably due to the electronegativity difference of Li and Sn. The electronegativity of Sn (1.96) is greater than lithium (0.98), so Sn will likely attract more electrons in the Li-Sn alloy.

During charging (Figure 6.12b), the peak position shifted back to lower energy and the peak height increased upon charging. The spectrum at 0.66V overlapped with that of the Sn metal foil indicating the formation of metallic Sn through the de-alloying process. Metallic Sn was continuously oxidized to higher oxidation state upon charging. The spectrum in the fully charged state (at 2.2 V) is very similar to SnS spectrum, suggesting reconversion of Sn to SnS. However, the reconverted SnS is not exactly the same as pristine SnS. As discussed in the XRD results, the SnS formed after charging is amorphous or nanocrystalline phase and perhaps could be off stoichiometry.

Local structural changes of SnS during the discharge/charge process were determined by the EXAFS. Figure 6.12c shows FT of the Sn K-edge EXAFS spectra for pristine, first fully discharged state (0.01V) and first fully charged state (2.2 V). The EXAFS spectra of commercial SnS and standard Sn metal foil are presented together as references. Both pristine SnS nanocrystals and commercial SnS showed a Sn-S peak at 2.2 Å. The FT magnitude changes of the Sn-S peak and Sn-Sn peak in EXAFS plot for the pristine and discharge state are clearly associated with dissociation of the Sn-S bond in SnS and the formation of metallic Sn-Sn bonds in the Li-Sn alloy as a result of the conversion and alloying reaction.[36] The fully charged sample showed a peak at 2.2 Å, the same as pristine and commercial SnS, suggesting Sn-S bonds was reformed through the reconversion reaction.

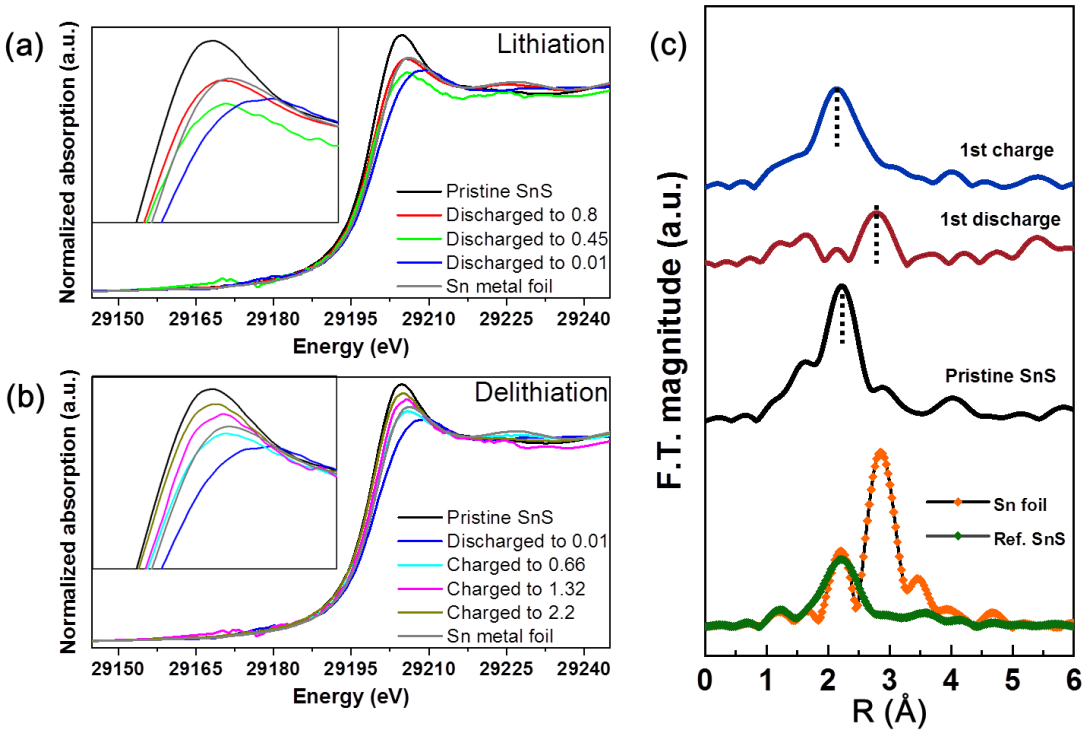

Figure 6.12 Ex situ XANES spectra of SnS in a solid-state cell during (a) discharging and (b) charging. (c) EXAFS spectra of SnS in a solid-state cell before cycling, after discharge and after charge.

GITT was performed to examine the reaction kinetics of SnS in solid-state cells (Figure 6.13). The electrodes were pre-cycled 3 times at 50 mA g^{-1} prior to GITT. During GITT measurements, the cell was allowed to relax for 4 h after every 1 h discharge and charge at 50 mA g^{-1}. The voltage difference (polarization) between the charge/discharge potential and the quasi-equilibrium potential after the 4h relaxation is plotted in Figure 6.13b. The conversion reaction showed a larger polarization than the alloying reaction during both charging and discharging. This agrees with Figure 6.6a and 6.6b that the reaction kinetics of conversion reaction is more sluggish than alloying reaction.

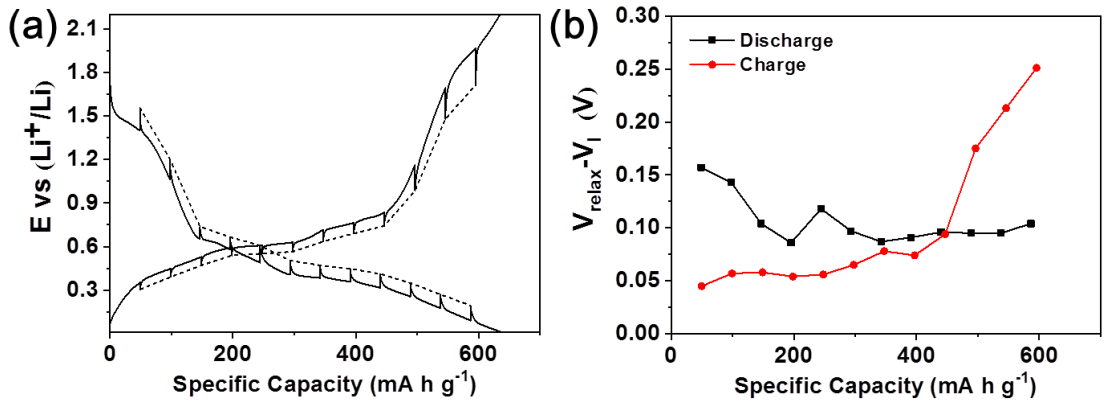

Figure 6.13 (a) GITT curves of ZB SnS in a solid state cell at room temperature. (b) Voltage difference after the 2 h relaxation at different states of discharge and charge.

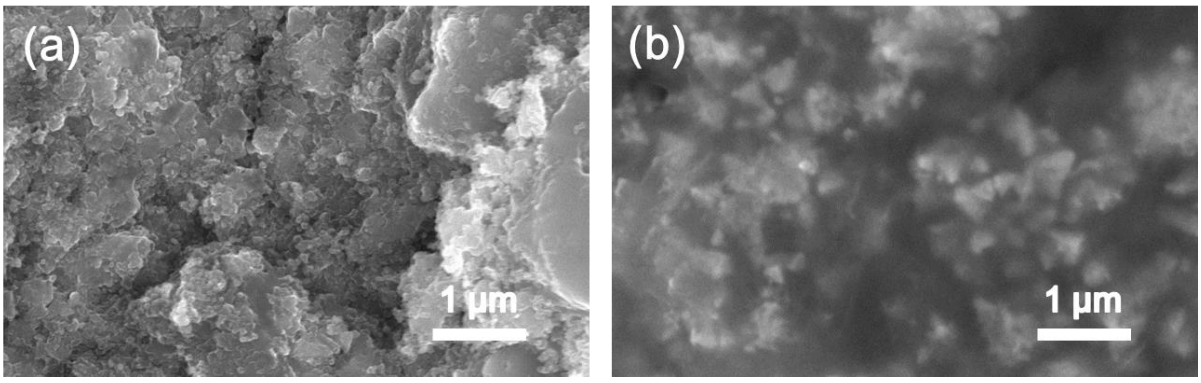

Figure 6.14 SEM image of ZB SnS electrodes in (a) solid-state cells and (b) liquid cells after first cycle.

6.3 Conclusions

In conclusion, SnS was evaluated in both solid-state and liquid cells. In the solid state, SnS showed a stable cycling performance with a discharge capacity of 629 mA h g^{-1} after 100 cycles at 50 mA g^{-1} at room temperature, while in a liquid cell rapid capacity decay was observed. The solid-state cell showed a very small irreversibility capacity (67 mA h g^{-1}, 8.2 %) in contrast to the liquid cell (488 mA h g^{-1}, 44.6 %). Postmortem analysis of the liquid cell by XPS and EDS revealed that a large irreversible capacity and capacity decay in the liquid cell can be attributed to the dissolution of discharge product during cycling. Limited SEI formation (by electrolyte reduction) in the solid state also contributed to the small irreversible capacity in the solid-state

cell. Ex-situ XRD and XAS showed that both the conversion and alloying reactions are reversible in the solid-state cell although crystallinity is not preserved in the conversion reaction. In summary, the solid electrolyte prevented the degradation of the SnS active material and enabled a reversible conversion reaction, leading to stable cycling performance. I hope that this work will spur further research on solid-state conversion or alloying battery systems.

6.4 Experimental section

Synthesis of SnS nanoparticles: SnS nanoparticles were synthesized by a wet chemical method. A 50-mL two-neck Schlenk flask was charged with oleylamine (10 mL) and dried under vacuum at 110 ℃ for 3 h, followed by addition of sulfur (18 mg, 0.56 mmol) under Ar atmosphere. After 10 min of stirring, the flask was naturally cooled to room temperature. $SnCl_2$ (100 mg, 0.53 mmol) was vacuum-dried for 10 min and dissolved in the above solution. The reaction flask was heated at 230 ℃ for 2 h under Ar atmosphere. After the reaction, the resulting products were washed with ethanol and centrifuged. The obtained SnS nanoparticles were dried in a vacuum oven at 30 ℃.

Material characterization: Sample morphologies were confirmed by Hitachi S-4800 and S-4300 SEM and JEOL JEM2100F TEM. EDS was performed using a Hitachi S-4700 SEM equipped with an Oxford INCA energy-dispersive X-ray analyzer. Surface chemical states were investigated by X-ray photoelectron spectroscopy (PHI 5700 ESCA for liquid cell and Kratos Axis Ultra XPS for solid-state battery) using monochromated Al Kα radiation (h = 1486.6 eV). Binding energies were calibrated based on the C 1s peak (284.5 eV). XRD was performed by a Philips X'pert MRD XRD (Materials Research Diffractometer) using Cu Kα radiation (λ = 0.15418 nm). For postmortem XPS analysis of liquid cells after cycling, electrodes were washed with DMC multiple times and dried in the glove box prior to analysis. Postmortem EDS analysis on the Li after cycling was done without washing the electrode.

Fabrication of liquid cells and electrochemical measurements: SnS (80 mg), carbon black (10 mg), NMP (100 mg), and PVDF (10 mg) were ground using a mortar and pestle. This mixture was coated on a Cu foil and dried under vacuum at 110 ℃ for 24 hours. The slurry coated Cu electrodes were cut into a 14 mm diameter circular shape. Half cells were fabricated in a coin cell (CR2032) in a glove box under Ar. Li metal and 1 M $LiPF_6$ in EC/DMC (1:1 v/v)

were used as counter electrode and electrolyte, respectively. Galvanostatic discharge/charge tests were conducted using a WBCS3000 automatic battery cycler and ZIVE SP system (WonATech).

Fabrication of an all solid-state battery and electrochemical measurements: All procedures described here were conducted in under Ar atmosphere. Glass type solid electrolytes were prepared by high-energy ball milling (8000M Mixer/Mill, SPEX SamplePrep) Li_2S (Sigma, 99.98%) and P_2S_5 (Sigma, 99%) in a 77.5 to 22.5 molar ratio for 10 h in a stainless steel vial. A composite cathode was prepared by mixing SnS nanoparticles, $77.5Li_2S$-$22.5P_2S_5$ solid electrolyte, and carbon black in a 10:20:2 weight ratio using a mortar and pestle. The solid-state batteries were constructed and tested using a PEEK cell die with Ti metal rods as current collectors for both the working and counter electrode. All solid-state batteries were composed of a composite cathode, $77.5Li_2S$-$22.5P_2S_5$ solid electrolyte, and Li-In alloy anode. First, 100 mg of $77.5Li_2S$-$22.5P_2S_5$ solid electrolytes was pressed at 73.8 MPa in the PEEK cell die to form a pellet. Then, 4 mg of composite powers were spread on the top of the solid electrolyte pellet and pressed at 369.2 MPa. Finally, Li-In anode was then attached to the other side of the solid electrolyte pellet and pressed at 369.2 MPa. Galvanostatic discharge/charge tests were performed using potentiostats (Bio-Logic VMP3 for solid-state battery) over a voltage range of -0.61 to 1.58 V vs. In/Li (0.01 to 2.2 V vs. Li/Li^+) at room temperature (22 ℃) and elevated temperature (60 ℃). All voltages stated in this work is based on Li/Li^+. Current densities and specific capacities were calculated based on the mass of SnS. For GITT measurement, the cell was allowed to relax for 4 h after every 1 h discharging/charging at 50 mA g^{-1} at room temperature. The ionic conductivity of solid electrolyte was measured by EIS in a symmetry cell at room temperature (22 ℃) and elevated temperature (60 ℃). An AC amplitude of 6 mV was applied over the frequency range of 1000 kHz to 0.1 Hz.

Ex-situ XANES Experiment: Ex-situ XAS measurements were performed at 7-BM (QAS) beamline of National Synchrotron Light Source II (NSLS-II) at Brookhaven National Laboratory (BNL). The samples were covered with Kapton tape to protect them from oxidation. Sn K-edge XAS spectra were collected at room temperature in the fluorescence mode. Reference spectra of a Sn foil were collected for energy calibration. To improve the data quality, the spectra were collected in multiple scans and merged. The XAS data were processed using Athena software package.[37] The extracted EXAFS signal, $\chi(k)$, was weighted by k^2 to emphasize the high

energy oscillations, and then Fourier-transformed in k-ranges of 2.5-10.2 A^{-1}, using a Hanning window function to obtain the magnitude plots of the EXAFS spectra in R-space (Å).

6.5 References

[1] R. Chen, W. Qu, X. Guo, L. Li, F. Wu, *Mater. Horiz.* **2016**, *3*, 487.

[2] J. G. Kim, B. Son, S. Mukherjee, N. Schuppert, A. Bates, O. Kwon, M. J. Choi, H. Y. Chung, S. Park, *J. Power Sources* **2015**, *282*, 299.

[3] E. Quartarone, P. Mustarelli, *Chem. Soc. Rev.* **2011**, *40*, 2525.

[4] C. Sun, J. Liu, Y. Gong, D. P. Wilkinson, J. Zhang, *Nano Energy* **2017**, *33*, 363.

[5] M. Tatsumisago, M. Nagao, A. Hayashi, *J. Asian Cerm. Soc.* **2013**, *1*, 17.

[6] G. Oh, M. Hirayama, O. Kwon, K. Suzuki, R. Kanno, *Chem. Mater.* **2016**, *28*, 2634.

[7] S. Kinoshita, K. Okuda, N. Machida, M. Naito, T. Sigematsu, *Solid State Ionics* **2014**, *256*, 97.

[8] F. Han, J. Yue, X. Fan, T. Gao, C. Luo, Z. Ma, L. Suo, C. Wang, *Nano Lett.* **2016**, *16*, 4521.

[9] M. Nagao, A. Hayashi, M. Tatsumisago, *J. Mater. Chem.* **2012**, *22*, 10015.

[10] V. P. Phan, B. Pecquenard, F. Le Cras, *Adv. Funct. Mater.* **2012**, *22*, 2580.

[11] S. M. Wood, E. J. Powell, A. Heller, C. B. Mullins, *J. Electrochem. Soc.* **2015**, *162*, A1182.

[12] Z. Zhang, C. Zhou, L. Huang, X. Wang, Y. Qu, Y. Lai, J. Li, *Electrochim. Acta* **2013**, *114*, 88.

[13] K. Li, S. Yan, Z. Lin, Y. Shi, *J. Alloys Compd.* **2016**, *681*, 486.

[14] B. Zhao, Z. Wang, F. Chen, Y. Yang, Y. Gao, L. Chen, Z. Jiao, L. Cheng, Y. Jiang, *ACS Appl. Mater. Interfaces* **2017**, *9*, 1407.

[15] L. Lu, L. Zhang, H. Zeng, B. Xu, L. Wang, Y. Li, *J. Alloys Compd.* **2017**, *695*, 1294.

[16] A. M. Tripathi, S. Mitra, *Rsc Adv.* **2015**, *5*, 23671.

[17] H.-C. Tao, X.-L. Yang, L.-L. Zhang, S.-B. Ni, *J. Electroanal. Chem.* **2014**, *728*, 134.

[18] J. Lu, C. Nan, L. Li, Q. Peng, Y. Li, *Nano Res.* **2013**, *6*, 55.

[19] J. Liu, M. Gu, L. Ouyang, H. Wang, L. Yang, M. Zhu, *ACS Appl. Mater. Interfaces* **2016**, *8*, 8502.

[20] D. H. Youn, S. K. Stauffer, P. Xiao, H. Park, Y. Nam, A. Dolocan, G. Henkelman, A. Heller, C. B. Mullins, *ACS Nano* **2016**, *10*, 10778.

[21] Y. Xu, Y. Zhu, Y. Liu, C. Wang, *Adv. Energy Mater.* **2013**, *3*, 128.

[22] W. M. Zhang, J. S. Hu, Y. G. Guo, S. F. Zheng, L. S. Zhong, W. G. Song, L. J. Wan, *Adv. Mater.* **2008**, *20*, 1160.

[23] J. Liu, X. Chen, J. Kim, Q. Zheng, H. Ning, P. Sun, X. Huang, J. Liu, J. Niu, P. V. Braun, *Nano Lett.* **2016**, *16*, 4501.

[24] S. Kim, J. Liu, K. Sun, J. Wang, S. J. Dillon, P. V. Braun, *Adv. Funct. Mater.* **2017**, *27*, 1702783.

[25] T. A. Yersak, H. A. Macpherson, S. C. Kim, V. D. Le, C. S. Kang, S. B. Son, Y. H. Kim, J. E. Trevey, K. H. Oh, C. Stoldt, *Adv. Energy Mater.* **2013**, *3*, 120.

[26] Y. Diao, K. Xie, S. Xiong, X. Hong, *J. Electrochem. Soc.* 2012, 159, A1816.

[27] Z. Li, S. Zhang, C. Zhang, K. Ueno, T. Yasuda, R. Tatara, K. Dokko, M. Watanabe, *Nanoscale* **2015**, *7*, 14385.

[28] M. Tatsumisago, S. Hama, A. Hayashi, H. Morimoto, T. Minami, *Solid State Ionics* **2002**, *154*, 635.

[29] J. M. Whiteley, J. W. Kim, D. M. Piper, S.-H. Lee, *J. Electrochem. Soc.* **2016**, *163*, A251.

[30] Y. Li, J. Tu, X. Huang, H. Wu, Y. Yuan, *Electrochim. Acta* **2006**, *52*, 1383.

[31] J. Yan, H. Huang, J. Zhang, Z. Liu, Y. Yang, *J. Power Sources* **2005**, *146*, 264.

[32] K. Wei, Y. Zhao, J. Liu, S. Liu, Y. Cui, R. Zhu, Y. Yang, Y. Cui, *Int. J. Electrochem. Sci.* **2017**, *12*, 7404.

[33] K. N. Wood, K. X. Steirer, S. E. Hafner, C. Ban, S. Santhanagopalan, S.-H. Lee, G. Teeter, *Nat. Commun.* **2018**, *9*, 2490.

[34] N. Oehl, G. Schmuelling, M. Knipper, R. Kloepsch, T. Placke, J. Kolny-Olesiak, T. Plaggenborg, M. Winter, J. Parisi, *CrystEngComm* **2015**, *17*, 8500.

[35] I. A. Courtney, J. Dahn, *J. Electrochem. Soc.* **1997**, *144*, 2045.

[36] C. J. Pelliccione, E. V. Timofeeva, C. U. Segre, *J. Phys. Chem. C* **2016**, *120*, 5331.

[37] J. Woicik, B. Ravel, D. Fischer, W. Newburgh, *J. Synchrotron Radiat.* **2010**, *17*, 409.

CHAPTER 7
CONCLUSIONS AND FUTURE WORK

7.1 Conclusions

In this dissertation, many issues of conversion and alloying electrodes for secondary batteries were discussed and addressed.

FeF_2 is one of the few conversion electrodes which can be considered as cathode due to its high thermodynamic reduction potential (2.66 V vs. Li/Li^+). However, its poor electrochemical performance originating from its sluggish kinetics, the insulating nature of FeF_2, and various degradation issues limit its practical application. In Chapter 2, the fabrication of Ni supported 3D Al_2O_3 coated FeF_2 electrode is presented to overcome such issues. The electrodes are prepared by colloidal templating, electrodeposition followed by facile fluorination and a thin layer of Al_2O_3 coating by atomic layer deposition. The 3D FeF_2 electrodes deliver an initial discharge capacity of 380 mA h g^{-1} at a current density of 200 mA g^{-1} at room temperature. Also, these electrodes show high volumetric capacity and stable cycling performance and exhibit good rate capability. The 3D scaffold facilitates the reaction kinetics and enables a high specific capacity by providing an efficient electron pathway to the insulating FeF_2 and shortening Li diffusion length. Al_2O_3 coating improves the cycle life as it prevents the side reaction by blocking the direct contact of the electrode with the electrolyte. Even though Chapter 2 reported a significant improvement in the electrochemical performance of FeF_2, the large hysteresis of FeF_2 is not practical yet. In Chapter 3 and 4, this dissertation demonstrates new alloying cathode materials with fast reaction kinetics and small hysteresis for lithium and sodium ion batteries.

The Li-iodine chemistry ($I_2 + 2Li \leftrightarrow 2LiI$) is considered to be one of the most promising candidates for high energy density cathodes, due to its high reaction potential (2.95 V vs Li^+/Li on average), high specific capacity (200 mAh g^{-1}) and the fast electrochemical conversion of the iodine/triiodide redox pair. However, Li-iodine batteries composed of Li metal and elemental iodine possess safety and fabrication challenges due to the use of Li metal and high volatility of iodine. These disadvantages could be avoided if LiI can be used as the starting cathode. Chapter 3 demonstrates the use of LiI as a Li-ion battery cathode by fabricating a freestanding reduced graphene oxide (rGO)/LiI composite. These electrodes exhibit stable long-term cycling and good

rate performance with a high specific capacity (200 mAh g^{-1} at 0.5 C after 100 cycles) and a very small hysteresis (0.056 V at 1 C). Also, shuttling was suppressed significantly. The improved electrochemical performance can be attributed to strong interactions between the active materials and rGO, and the reduced ion and electron transport distances provided by the 3D structured cathode.

Analogously, Na-iodine chemistry ($I_2 + 2Na \leftrightarrow 2NaI$) can also be used for SIBs and expected to have similar electrochemical properties with Li-iodine system. Chapter 4 demonstrates the use of NaI as a Na-ion battery cathode using a freestanding NaI-loaded CNT mat electrode. These electrodes show stable long-term cycling performance (92% capacity retention after 100 cycles at 100 mA h g^{-1}) and a high specific energy density (~473 W h kg^{-1}, first discharge basis vs. Na metal) and small hysteresis (0.03 V), indicating the electrode is working very close to its thermodynamic limits. Shuttling was suppressed significantly by using a CNT interlayer and adding FEC to the electrolyte. Ex situ XPS and Raman analysis revealed the reaction chemistry occurring during the cycling.

Another drawback of non-intercalatation electrodes is its huge volume change. Sb compounds are high capacity anode candidates for SIBs. However, its huge volume change during cycling causes active material pulverization and loss of electrical contact between the active material and the current collector. Chapter 5 reports the fabrication of 3D Ni supported Sb_2O_3 electrodes and shows that both high gravimetric and volumetric capacities are achieved by nanostructure engineering. The electrodes showed a specific capacity of ~445 mA h g and volumetric capacity of ~488 mA h cm^{-3} with capacity retention of 89 % after 200 cycles at 200 mA h g^{-1}. The enhanced cyclability can be mainly attributed to the 3D Ni scaffold which accommodates volume changes curing cycling and supports active materials, and post annealing effect.

Lastly, reversibility of conversion reaction was greatly improved by the use of solid electrolyte in Chapter 6. Solid-state batteries can potentially enable new classes of electrode materials which are unstable against liquid electrolytes. SnS nanocrystals were synthesized by wet chemical method and its electrochemical properties were examined in both solid-state and liquid cells. The solid-state cell delivered a capacity of 629 mA h g^{-1} after 100 cycles and exhibited a small irreversible capacity in the first cycle (8.2 %), while the liquid cell showed a rapid capacity decay and large irreversible capacity (44.6 %). XPS and EDS were used to

investigate the differences between the solid-state and liquid cells. Ex XRD and XAS showed that both conversion and alloying reaction are reversible in a solid-state cell although amorphization was observed in the conversion reaction. The solid electrolyte prevented the degradation of the SnS, enabled a reversible conversion reaction, and suppressed electrolyte reduction, leading to a stable cycling performance and small first cycle irreversible capacity.

Various conversion and alloying electrodes have been fabricated and investigated in this dissertation. Many issues of non-intercalation electrodes have been addressed systematically by understanding materials science and using engineering. This dissertation shows the potential of non-intercalation electrodes and provides a guideline on how to design and use them for next-generation secondary batteries.

7.2 Future work

The fabrication procedure described in Chapter 2 can be applied for the synthesis of other metal fluorides on a 3D conductive scaffold. It would be interesting to explore electrochemical properties of other fluorides incorporated into 3D conductive scaffold. MnF_2, CuF_2 and CoF_2 are fluoride candidates worth trying. Especially, $Cu_{0.5}Fe_{0.5}F_2$ appears to be the most promising. The previous study reported that $Cu_{0.5}Fe_{0.5}F_2$ exhibited high working voltage with reduced hysteresis.[1] The stoichiometry of $Cu_xF_{1-x}F_2$ can be controlled precisely by co-electrodeposition of Cu and Fe.

In Chapter 2 and 3, new cathode materials (LiI and NaI) for lithium and sodium ion batteries are presented. Even though they showed reduced shuttling, high specific capacity and stable long-term cycling performance, there is still room for performance improvement. More various types of electrolyte should be tested for LiI and NaI. Shuttling and cross-over of active materials can be more suppressed by optimizing the electrolyte composition or finding new electrolyte additives. The most ideal case would be to use gel or solid electrolytes. The areal loading also needs to be increased. Previously reported high areal capacity electrode studies would be good references.[2,3] Full cell demonstration would also be meaningful as a practical application.

3D Ni scaffolds used in Chapter 2 and 4 are heavy and should be replaced with lighter conductive scaffolds such as 3D lighter metal or carbon template.[4,5] A freestanding and thick

template which enables high areal loading would be the most promising alternative to 3D Ni inverse opal scaffold.[6]

How the volume expansion of conversion electrodes is accommodated in a solid-state battery is not discussed in Chapter 5. It is not intuitive to understand the volume expansion of conversion electrodes in solid-state cells because there is no free space within the electrode and solid electrolyte is not flowing. The volume expansion in solid-state batteries has not been studied elsewhere and it would be worthwhile to study. Finally, other electrode materials which are not compatible with a conventional liquid cell can also be investigated by using a solid-state battery.[7]

7.3 References

[1] F. Wang, S.-W. Kim, D.-H. Seo, K. Kang, L. Wang, D. Su, J. J. Vajo, J. Wang, J. Graetz, *Nat. Commun.* **2015**, *6*, 6668.

[2] R. Carter, B. Davis, L. Oakes, M. R. Maschmann, C. L. Pint, *Nanoscale* **2017**, *9*, 15018.

[3] Y. Li, K. K. Fu, C. Chen, W. Luo, T. Gao, S. Xu, J. Dai, G. Pastel, Y. Wang, B. Liu, *ACS Nano* **2017**, *11*, 4801.

[4] J. Schuster, G. He, B. Mandlmeier, T. Yim, K. T. Lee, T. Bein, L. F. Nazar, *Angew. Chem., Int. Ed.* **2012**, *51*, 3591.

[5] Q. Pham, M. Barako, J. Tice, Y. Won, *Sci. Rep.* **2017**, *7*, 10465.

[6] H. Zhang, H. Ning, J. Busbee, Z. Shen, C. Kiggins, Y. Hua, J. Eaves, J. Davis, T. Shi, Y.-T. Shao, *Sci. Adv.* **2017**, *3*, e1602427.

[7] X. Hua, R. Robert, L.-S. Du, K. M. Wiaderek, M. Leskes, K. W. Chapman, P. J. Chupas, C. P. Grey, *J. Phys. Chem. C* **2014**, *118*, 15169.